New measurement methods and physico-chemical properties of the MSFR salt

Mastromarino, S.

DOI
10.4233/uuid:499dabd7-14be-4815-9597-5b9415db8f04

Publication date
2022

Document Version
Final published version

Citation (APA)
Mastromarino, S. (2022). *New measurement methods and physico-chemical properties of the MSFR salt*. [Dissertation (TU Delft), Delft University of Technology]. https://doi.org/10.4233/uuid:499dabd7-14be-4815-9597-5b9415db8f04

Propositions

accompanying the dissertation

NEW MEASUREMENT METHODS AND PHYSICO-CHEMICAL PROPERTIES OF THE MSFR SALT

by

Sara MASTROMARINO

1. Among the Gen IV reactors, the Molten Salt Fast Reactor (MSFR) will be most likely used because of their low environmental impact [1].
2. The large number of native Americans who felt ill working in uranium mining without proper safety precautions is a result of the abuse of white privilege [2].
3. Pursuing both chloride and fluoride salt reactors will hamper the development of the molten salt reactor.
4. It is more difficult to measure the thermal conductivity than the viscosity of molten salts. (This thesis)
5. A good measurement starts with a proper design of the experiment.
6. Traces should not be called impurities.
7. If you practice what you teach, you become a better teacher.
8. A team gets better when it embraces inclusion and diversity.
9. The statement of Barrow: "the best bikers, not necessarily the best triathlon athletes, have the greatest chance of winning" is not true [3].
10. The most common fatality in triathlon is drowning [4], but learning to swim better will not solve the problem.

These propositions are regarded as opposable and defendable, and have been approved as such by the promotors prof. dr. ir. J.L. Kloosterman and dr. ir. M. Rohde

---

[1] D. D. Siemer, *"Why the molten salt fast reactor (MSFR) is the "best" Gen IV reactor ?"*, Energy Science & Engineering 3, 83 (2015): 83–97

[2] J. Lewis, J. Hoover and D. Mackenzie, *Mining and Environmental Health Disparities in Native American Communities*, Current Environmental Health Reports 4, 130 (2017).

[3] J. D. Barrow, *100 Essential Things You Didnt Know You Didnt Know about Sport*, edited by B. Head (April 9, 2012)

[4] Wikipedia, *List of triathlon fatalities - Wikipedia, the free encyclopedia, https://en.wikipedia.org/wiki/List of triathlon fatalities (2021)*, [Online; accessed 06-April-2021].

Stellingen

behorende bij het proefschrift

NEW MEASUREMENT METHODS AND PHYSICO-CHEMICAL PROPERTIES OF THE MSFR SALT

door

Sara MASTROMARINO

1. Van de Gen IV-reactoren zal de Molten Salt Fast Reactor (MSFR) het meest waarschijnlijk worden gebruikt vanwege de geringe milieueffecten [5].
2. Het grote aantal inheemse Amerikanen dat zich ziek voelde bij het werken in uraniummijnen zonder de juiste veiligheidsmaatregelen is een gevolg van het misbruik van het blanke voorrecht [6].
3. Het nastreven van zowel chloride- als fluoridezoutreactoren zal de ontwikkeling van de gesmoltenzoutreactor belemmeren.
4. Het is moeilijker om de thermische geleidbaarheid te meten dan de viscositeit van gesmolten zouten. (Deze dissertatie).
5. Een goede meting begint met een goede opzet van het experiment.
6. Sporen mogen geen onzuiverheden genoemd worden.
7. Als je in de praktijk brengt wat je onderwijst, word je een betere leraar.
8. Een team wordt beter als het inclusie en diversiteit omarmt.
9. De uitspraak van Barrow: "de beste bikers, niet noodzakelijk de beste triatleten, hebben de grootste kans om te winnenïs niet waar [7].
10. Het meest voorkomende dodelijke slachtoffer in triatlon is verdrinking [8], maar beter leren zwemmen lost het probleem niet op.

Deze stellingen worden opponeerbaar en verdedigbaar geacht en zijn als zodanig goedgekeurd door de promotoren prof. dr. ir. J.L. Kloosterman en dr. ir. M. Rohde

---

[5] D. D. Siemer, *"Why the molten salt fast reactor (MSFR) is the "best"Gen IV reactor ?"*, Energy Science & Engineering 3, 83 (2015): 83–97

[6] J. Lewis, J. Hoover and D. Mackenzie, *Mining and Environmental Health Disparities in Native American Communities*, Current Environmental Health Reports 4, 130 (2017).

[7] J. D. Barrow, *100 Essential Things You Didnt Know You Didnt Know about Sport*, edited by B. Head (April 9, 2012)

[8] Wikipedia, *List of triathlon fatalities Wikipedia, the free encyclopedia, https://en.wikipedia.org/wiki/List of triathlon fatalities (2021)*, [Online; accessed 06-April-2021].

NEW MEASUREMENT METHODS AND PHYSICO-CHEMICAL PROPERTIES OF THE MSFR SALT

NEW MEASUREMENT METHODS AND PHYSICO-CHEMICAL PROPERTIES OF THE MSFR SALT

Proefschrift

ter verkrijging van de graad van doctor
aan de Technische Universiteit Delft,
op gezag van de Rector Magnificus Prof. dr. ir. T.H.J.J. van der Hagen,
voorzitter van het College voor Promoties,
in het openbaar te verdedigen op

door

Sara MASTROMARINO

Master of Science in Chemistry,
Universitá La Sapienza, Rome, Italië
geboren te Aprilia, Italië.

Dit proefschrift is goedgekeurd door de promotoren:
Prof. dr. ir. J.L. Kloosterman
Dr. ir. M. Rohde

Samenstelling promotiecommissie:

Rector Magnificus,	voorzitter
Prof. dr. ir. J.L. Kloosterman	Technische Universiteit Delft, promotor
Dr. ir. M. Rohde	Technische Universiteit Delft, promotor
Onafhankelijke leden:	
Prof. dr. R. J. M. Konings	Technische Universiteit Delft
Dr. S. Delpech	Université Paris-Saclay
Dr. ir. M. Verweij	Technische Universiteit Delft
Dr. R. O. Scarlat	University of California-Berkeley
Overige leden:	
Dr. O. Beneš	European Commission

Keywords: Molten salt reactor, Nuclear reactor, Chemico-physical properties, Viscosity, Melting point, Dissolution, Thermal diffusivity
Printed by: Ipskamp Printing (http://www.ipskampprinting.nl/)

This research was performed in the Reactor Physics and Nuclear Materials (RPNM) section of the Department of Radiation Science and Technology (RST) of Delft University of Technology (The Netherlands) and in the Joint Research Center (JRC) - Karlsruhe of the European Commission in Karlsruhe (Germany).

Financial support:
This project has received funding from the Euratom research and training programme 2014-2018 under the grant agreement No. 661891

ISBN 000-00-0000-000-0

to my parents for planting the seeds of who I am today

You can stop and your pain will stop,
but you will not experience the finish line
if you do not live it fully.

CONTENTS

4 An Ultrasonic Shear Wave Viscometer for Low Viscosity liquids 51

5 Dissolution of Fuel Salt into Water 89

SUMMARY

The Molten Salt Reactor (MSR) is one of the six types of Generation IV nuclear energy systems with the main goals of sustainability, safety, reliability, economic competitiveness and proliferation resistance. This technology has spawn interest worldwide. Numerous universities, institutes and companies are carrying out research projects related to molten salt reactors. In Europe, the research is focused on the development of a fast-spectrum design, the Molten Salt Fast Reactor (MSFR).

The peculiarity and innovation of the MSR technology is the use of liquid fuel; a molten salt mixture in which both fissile and fertile isotopes are dissolved. A number of technological challenges must be addressed for the design of the reactor and the safety approach must be established. The highest priority issues are in the area of fuel salt development, structural materials, on-site fuel processing and the licensing procedure. Fundamental research needs to be conducted to determine thermodynamic and kinetic data of fuel salts. One of the aims of the project that led to this thesis is the characterization of the fuel salt under normal and accidental conditions, providing the basis for the safety evaluation of the reactor.

Reliable data on the thermal properties of molten salt mixtures are scarce. This research focuses on the experimental evaluation of some thermodynamic properties of molten salts. The thesis presents new methods for measuring thermal diffusivity and viscosity, and established methods for measuring melting point and dissolution of the salt in water.

Within the studied thermodynamic properties, the melting point was measured for PuF_3 and one of the MSFR fuel mixtures LiF-ThF_4-UF_4-PuF_3 (77.5-6.6-12.3-3.6 mol %). The melting point was measured via differential scanning calorimetry. PuF_3 was studied using adapted crucibles in ceramic material (BN), graphite, glassy carbon and BN with liners of Pt and W. These new crucibles were designed at JRC-Karlsruhe for reaching the high melting point of PuF_3, found to be 1680 ± 10 K. For the MSFR mixture, the melting point (776 ± 2 K) was measured via DSC using stainless steel crucibles with liners of nickel. The measured melting point was compared to the optimized pseudo binary phase diagram of LiF-ThF_4 with fixed amount of UF_4 and PuF_3 as in the fuel mixture molar ratio. X-ray Diffraction analysis was used to study the purity of the samples before the DSC measurement, which is particularly important for a reliable determination of the melting point. It was found that in most cases PuOF was formed when PuF_3 was molten in BN crucibles without a liner, making these results unreliable. Other materials for the crucibles and liners were therefore used to improve the melting point measurement.

The thermal diffusivity has been studied for MSR fuel and coolant salt mixtures in their solid state because a solid salt layer can be formed under cooling conditions that may add a significant heat resistance during transient conditions. The alkali halides as LiF, KF, NaF and their ternary mixture FLiNaK were measured. The thermal diffusivity of LiF, being the only fluoride salt measured in literature, was compared to these literature results. Thereafter, the thermal diffusivity of PuF_3 and molten salt fuel mixtures LiF-ThF_4-UF_4 (77.5-20.0-2.5 mol %) and LiF-ThF_4-UF_4-PuF_3 (77.5-6.6-12.3-3.6 mol %) have been measured for the first time. The Laser Flash facility at JRC-Karlsruhe was used to measure the thermal diffusivity as a function of temperature in the range from 500 K to 100 K below the melting point of each sample analyzed. It was found that the thermal conductivity, calculated from the measured thermal diffusivity, is very small for the molten salt fuel mixtures in their solid state, i.e. between 0.4 and 3 W/mK, while it is higher for the alkali fluorides, being between 1 and 10 W/mK.

An accurate measurement of viscosity is necessary to predict the flow and turbulent heat transfer of the fuel salt through the reactor circuit. Current techniques for measuring the viscosity could not be used for molten salts due to the small amount of fuel salt available, the radioactivity of the samples and their corrosiveness. An innovative method based on ultrasonic wave propagation has been developed for measuring the viscosity. In this method, a waveguide has been used to remotely transmit ultrasonic shear waves into the liquid. The attenuation of the amplitude of shear waves has been used to extract the liquid viscosity. Measurements on fluids with similar viscosity of molten salt illustrated that the method can successfully measure changes in attenuation due to the viscosity of the liquid. The range of viscosities measured was between 0.8 and 60 mPa-s, with relative error lower than 12 % and uncertainty lower than 5 %. Measurements were also performed varying the dimension of the waveguide and the container for the liquid with the goal of minimizing the liquid analyzed. Higher temperature measurements, up to 70 °C, were also performed with the goal of transforming the current setup in an elevated temperature setup. This method offers advantages such as the capability to perform in situ measurements, the omission of mechanical parts and the possibility to handle very small volumes of liquid.

In this work we present a comprehensive description of the interaction of solid MSFR fuel salt with water. For the salt, the binary systems LiF-ThF_4 and the ternary system LiF-ThF_4-UF_4 were analysed. Also LiF-NaF-KF, which is considered as a coolant for MSFR and which is commonly used as simulant of the fuel salt, was analysed. The three salts have been mixed with water in the ratio of 10 g/l (also 5 g/l for the LiF-ThF_4-UF_4 salt) to simulate the scenario of the fuel leakage in water during storage of the salt. The experiments were repeated for different conditions of physical state. To maximize the dissolution process, a part of the fuel salt was ground to powder to increase the contact surface exposed to the aqueous phase. Experiments were performed at a constant temperature of 25°C and 75°C to evaluate the effect of temperature. Furthermore, we studied also the effect of gamma radiation on the salt solubility, performing experiments under irradiation in a Co-source. After dissolution, the concentration of the single fluorides in water was determined by inductively coupled plasma-optical emission spectroscopy. The hydrate compounds formed in these systems have been determined using powder X-ray diffraction, while the possible change of oxidation state of uranium was studied by X-ray absorption spectroscopy.

This thesis provides new data on some thermal properties of molten salt mixtures and show the applicability of new methods for the determination of viscosity and thermal diffusivity of molten salts.

SAMENVATTING

De gesmolten-zoutreactor (MSR) is een van de zes types kernenergiesystemen van de vierde generatie, met als voornaamste doelstellingen duurzaamheid, veiligheid, betrouwbaarheid, economisch concurrentievermogen en proliferatiebestendigheid. Deze technologie heeft wereldwijd grote belangstelling gewekt. Talrijke instituten voeren onderzoeksprojecten uit met betrekking tot gesmolten zout reactoren. In Europa is het onderzoek toegespitst op de ontwikkeling van een snel-spectrumontwerp, de Molten Salt Fast Reactor (MSFR).

De bijzonderheid en innovatie van de MSR-technologie is het gebruik van vloeibare brandstof; een mengsel van gesmolten zout waarin zowel splijtbare isotopen als kweekstoffen zijn opgelost. Voor het ontwerp van de reactor moet een aantal technologische uitdagingen worden aangegaan en moet een veiligheidsaanpak worden vastgesteld. De hoogste prioriteit wordt gegeven aan de ontwikkeling van splijtstoffen, constructiematerialen, de verwerking van splijtstoffen ter plaatse en de vergunningsprocedure. Er moet fundamenteel onderzoek worden verricht om thermodynamische en kinetische gegevens over splijtstofzouten te bepalen. Een van de doelstellingen van het project dat tot dit proefschrift heeft geleid, is de karakterisering van het splijtstofzout onder normale omstandigheden en bij ongevallen, waarmee de basis wordt gelegd voor de veiligheidsevaluatie van de reactor.

Betrouwbare gegevens over de thermische eigenschappen van gesmolten zoutmengsels zijn schaars. Dit onderzoek richt zich op de experimentele meting van enkele thermodynamische eigenschappen van gesmolten zouten. Het proefschrift presenteert nieuwe methoden voor het meten van thermische diffusiviteit en viscositeit, en gevestigde methoden voor het meten van het smeltpunt en het oplossend vermogen van zout in water.

Binnen de bestudeerde thermodynamische eigenschappen werd het smeltpunt gemeten voor PuF_3 en één van de MSFR-brandstofmengsels LiF-ThF_4-UF_4-PuF_3 (77,5-6,6-12,3-3,6 mol %). Het smeltpunt werd gemeten met differentiële scanning calorimetrie. PuF_3 werd bestudeerd met aangepaste smeltkroezen in keramisch materiaal (BN), grafiet, glasachtige koolstof en BN met voeringen van Pt en W. Deze nieuwe smeltkroezen werden bij JRC-Karlsruhe ontworpen om het hoge smeltpunt van PuF_3 te bereiken, dat 1680 ± 10 K bleek te zijn. Voor het MSFR-mengsel werd het smeltpunt (776 ± 2 K) gemeten via DSC met gebruikmaking van roestvrijstalen smeltkroezen met voeringen van nikkel. Het gemeten smeltpunt werd vergeleken met het geoptimaliseerde pseudo binaire fasediagram van LiF-ThF_4 met een vaste hoeveelheid UF_4 en PuF_3 als in de molaire verhouding van het brandstofmengsel. Met behulp van röntgendiffractieanalyse werd de zuiverheid van de monsters vóór de DSC-meting bestudeerd, wat bijzonder belangrijk is voor een betrouwbare bepaling van het smeltpunt. Gebleken is dat in de meeste gevallen PuOF werd gevormd wanneer PuF_3 werd gesmolten in BN-kroezen zonder voering, waardoor deze resultaten niet betrouwbaar zijn. Daarom werden andere materialen voor de smeltkroezen en voeringen gebruikt om de smeltpuntmeting te optimaliseren. De thermische diffusie is bestudeerd voor MSR brandstof en koelmiddelzouten in vaste toestand, omdat onder koelomstandigheden een vaste zoutlaag kan worden gevormd die een belangrijke warmteweerstand kan toevoegen tijdens transiënte omstandigheden. De alkali-halogeniden LiF, KF, NaF en hun ternaire mengsel FLiNaK werden gemeten. De thermische diffusiviteit van LiF, het enige fluoridezout dat in de literatuur is gemeten, werd vergeleken met deze literatuurresultaten. Daarna zijn de thermische diffusie van PuF_3, $LiF\text{-}ThF_4\text{-}UF_4$ (77,5-20,0-2,5 mol %) en $LiF\text{-}ThF_4\text{-}UF_4\text{-}PuF_3$ (77,5-6,6-12,3-3,6 mol %) voor het eerst gemeten. De Laser Flash faciliteit werd gebruikt om de thermische diffusie te meten als functie van temperatuur in het gebied van 500 K tot 100 K onder het smeltpunt van elk geanalyseerd monster. Gebleken is dat de thermische geleidbaarheid, berekend uit de gemeten thermische diffusiviteit, zeer gering is voor de brandstofmengsels van gesmolten zout in vaste toestand, namelijk tussen 0,4 en 3 W/mK, terwijl deze voor de alkalifluoriden groter is, namelijk tussen 1 en 10 W/mK.

Een nauwkeurige meting van de viscositeit is noodzakelijk om de stroming en de turbulente warmteoverdracht van het splijtstofzout door het reactorcircuit te voorspellen. De huidige technieken voor het meten van de viscositeit kunnen niet worden gebruikt voor gesmolten zouten vanwege de kleine hoeveelheid beschikbaar splijtstofzout, de radioactiviteit van de monsters en hun corrosiviteit. Voor de meting van de viscositeit is een innovatieve methode ontwikkeld op basis van de voortplanting van ultrasone golven. Bij deze methode is gebruik gemaakt van een golfgeleider om ultrasone afschuifgolven op afstand in de vloeistof uit te zenden. De demping van de amplitude van de afschuifgolven is gebruikt om de viscositeit van de vloeistof te bepalen. Metingen aan vloeistoffen met een vergelijkbare viscositeit als gesmolten zout hebben aangetoond dat de methode met succes veranderingen in de demping ten gevolge van de viscositeit van de vloeistof kan meten. Het bereik van de gemeten viscositeiten lag tussen 0,8 en 60 mPa-s, met een relatieve fout van minder dan 12 % en een onzekerheid van minder dan 5 %. Metingen werden ook uitgevoerd met verschillende waarden van de afmeting van de golfgeleider en van de container voor de vloeistof met het doel de geanalyseerde vloeistof te minimaliseren. Metingen bij hogere temperaturen, tot 70°C, werden ook uitgevoerd met het doel de huidige opstelling om te zetten in een opstelling voor hogere temperaturen. Deze methode biedt voordelen zoals de mogelijkheid om in situ metingen uit te voeren, het weglaten van mechanische onderdelen en de mogelijkheid om zeer kleine vloeistofvolumes te hanteren.

In dit werk presenteren wij een uitgebreide beschrijving van de interactie van vast MSFR splijtstofzout met water. Voor het zout werden de binaire systemen $LiF\text{-}ThF_4$ en het ternaire systeem $LiF\text{-}ThF_4\text{-}UF_4$ geanalyseerd. Om te beginnen werd LiF-NaF-KF geanalyseerd, dat beschouwd wordt als koelvloeistof voor MSFR en dat algemeen gebruikt wordt als simulant van het splijtstofzout. De drie zouten werden gemengd met water in een verhouding van 10 g/l (ook 5 g/l voor het $LiF\text{-}ThF_4\text{-}UF_4$ zout) om het scenario te simuleren van het lekken van de splijtstof in water tijdens de opslag van het zout. De experimenten werden herhaald voor verschillende condities. Om het oplossingsproces te maximaliseren werd een deel van het splijtstofzout vermalen tot poeder om het contactoppervlak met de waterige fase te vergroten. De experimenten werden uitgevoerd bij een constante temperatuur van 25°C en 75°C om het effect van de temperatuur te evalueren. Bovendien hebben we ook het effect van gammastraling op de oplosbaarheid van het zout bestudeerd door experimenten uit te voeren onder bestraling in een Cobron. Na het oplossen werd de concentratie van de afzonderlijke fluoriden in water bepaald met behulp van inductief gekoppelde plasma-optische emissiespectroscopie. De hydraatverbindingen die in deze systemen werden gevormd, zijn bepaald met behulp van röntgendiffractie in poedervorm, terwijl de mogelijke verandering van de oxidatietoestand van uranium is bestudeerd met röntgenabsorptiespectroscopie.

Dit proefschrift verschaft nieuwe gegevens over enkele thermische eigenschappen van gesmolten zoutmengsels en toont de toepasbaarheid aan van nieuwe methoden voor de bepaling van de viscositeit en de thermische diffusiviteit van gesmolten zouten.

1

INTRODUCTION

> *There are known knowns.*
> *These are things we know that we know.*
> *There are known unknowns.*
> *That is to say, there are things that we know we don't know.*
> *But there are also unknown unknowns.*
> *There are things we don't know we don't know.*
>
> Donald Rumsfeld

With the current trend of global warming, the need for sustainable and clean power supply for the world's fast growing population has become more prominent [1]. New sources of sustainable energy (e.g solar, hydro, biomass, and wind) are being discovered and developed at a fast pace. Key players in the current energy problem are nuclear power plants. Although nuclear energy can yield an enormous amount of energy, is reliable, sustainable and economically competitive, controversial arguments exist. The radioactive fuel, used in nuclear reactors for generating energy, is hazardous when not dealt with in a well controlled way. Safety is a concern as shown by the accidents in Chernobyl and Fukushima [2]. The radioactive waste that is produced has to be stored in a safe and controlled place until it is not highly radioactive anymore; a process that can take thousands of years. Moreover, traditional energy sources using fossil fuels are still cheaper to use. To deal with these downsides, a constant improvement of nuclear power plants is needed in order to support the future role of nuclear energy.

The Generation IV International Forum (GIF) was set up in 2000 to support the development of the next generation nuclear energy systems. Six new types of Generation IV nuclear energy systems were proposed. In particular, sustainability, safety and reliability, economic competitiveness and proliferation resistance are the main goals of Generation IV Nuclear Reactors [3]. This thesis focuses on one of the six possible candidates: the Molten Salt Reactor (MSR), and in particular on one type of MSR, the Molten Salt Fast Reactor (MSFR).

1.1. THE MOLTEN SALT REACTOR: TECHNOLOGY, ADVANTAGES AND CHALLENGES

In essence, a molten salt reactor core is a vessel that contains a hot liquid salt in which a nuclear reaction takes place. The peculiarity and innovation of the MSR technology is the use of liquid fuel; a molten salt mixture in which both fissile and fertile isotopes are dissolved. A dual function is played by the salt, which serves both as nuclear fuel and as a heat transfer medium. The heat generated by the fission reaction in the reactor core is transferred in one or more intermediate heat exchangers to a secondary liquid salt coolant. This secondary loop is partly inside the reactor core and may possibly be contaminated by the radioactive fuel. A third loop consists of a power cycle facility where the heat is transformed to electricity. A schematic representation of the reactor is shown in Figure 1.1. As it can be seen in the figure, other peculiarities of the MSR with respect to current light water-based reactors are its freeze plug and drain tanks. Moreover, a small part of the fuel salt is extracted and circulated through a chemical processing plant to maintain the salt in a clean operating condition by removing fission products and adjusting the fissile and fertile concentration. In addition, MSRs may be single fluid (Th and U are contained in the same salt) or double-fluid, with the fertile salt containing Th kept separate from the fissile salt with only U. The latter can also be a breeder reactor, meaning that the reactor produces more fissile isotopes than it consumes. MSRs may or may not have a moderator, leading to a broad range of neutron spectra, ranging thermal or fast reactors. Unlike a thermal reactor, the molten salt fast concept does not have a graphite moderator in the core (graphite-free core), resulting in a breeder reactor with a fast neutron spectrum and operating in the Thorium fuel cycle [4]. The latter means that the MSFR uses thorium as the fertile element. Its initial fissile load may comprise ^{233}U, ^{235}U enriched (between 5% and 19.75%) or the transuranic (TRU) elements currently produced by PWRs [5]. The external core structures and the fuel heat exchangers of the MSFR are protected by a thick shielding made of concrete, designed to reduce the gamma and neutron fluxes to acceptable levels. The radial layout includes a fertile blanket to increase the breeding ratio. This blanket is filled with a fertile salt made of LiF-ThF_4 with initially 22.5 mol% of ^{232}Th.

The most important advantages that result from this design [6, 7] are summarized below:

- The fluid state of the fuel means that the fluid fuel salt can be automatically drained via freeze plugs to multiple storage tanks placed underneath the core. This is a passive safety system triggered by the melting of the plug (which occurs when the temperature in the primary circuit becomes too high).
- The molten fuel and coolant salts are stored under ambient pressure due to the high boiling point and low vapour pressure. The risk of reactor vessel break or salt leak due to high pressure is therefore negligible. Still, regular inspection of the vessel is needed since the corrosion of the vessel can deteriorate its strength.
- The high operating temperature of the salt means high efficiency in the conversion of thermal energy into electrical energy and even supports high temperature heat based applications, such as hydrogen production.

- Most of the fission products are retained in the fuel mixture and form stable fluorides.
- In an integrated chemical processing plant, the fuel is continuously cleaned and controlled by removing the fission products. This allows adjusting the fissile concentrations on a continuous basis and removing the poisoning fission products, such as the Xe isotopes.
- The removal of the fission products has also the advantage of reducing the decay heat after reactor shut down.
- For solid-fuel reactors the standard safety goal is to keep the fuel confined as much as possible. In MSFR, the salt is free to expand upon heating. This leads, in fact, to strong negative temperature and void coefficients.
- The MSFR can operate as a ”breeder” in the thorium fuel cycle. In this mode, the reactor produces more fissile isotopes through absorption in the fertile material than it consumes. The high fuel efficiency of these kind of reactors and the reduction of actinide waste fuel to the breeding process makes these reactors very interesting [8]. In the MSFR a container can be located in the core with a blanket salt inside, whose composition increases the breeding ratio.
- The MSFR can operate as a ”burner”. A burner reactor has the main purpose to fission plutonium and minor actinides without generating new ones, thus optimizing waste treatment. Contrary to breeder reactors, burner reactors do not increase the fissile fuel-stocks.
- More generally, the continuous fuel recirculation leads to very high burnup and low radioactivity inventory inside the reactor. Produced waste reaches natural levels of radiotoxicity after just a couple of centuries (compared to the $\sim 2.5 \cdot 10^5\ y$ in standard nuclear reactors).

This technology is still in the development phase. A number of technological challenges must be addressed and the safety approach must be established. The highest priority issues are in the area of (1) fuel development, (2) structural materials, (3) on-site fuel processing and (4) licensing procedure. Fundamental research needs to be conducted to determine thermodynamic and kinetic data on fuel salts. One of the aims of the project that led to this thesis work is the characterization of the fuel salt under normal and accidental conditions, providing the basis for the safety evaluation of the reactor. The safety assessment of this type of reactors, and in particular of MSFR, is also the main goal of the SAMOFAR project, that stands for Safety Assessment of the Molten Salt Fast Reactor. Most of the work presented in this thesis was possible thanks to the collaboration within the SAMOFAR project.

1.2. MOLTEN SALT REACTOR: THE HISTORY

Molten Salt Reactors were developed primarily at Oak Ridge National Laboratory (ORNL) beginning in the late 1940s. They were first designed for military purposes intended for a nuclear-powered aircraft [10] but recognized to be interesting also for the civilian nuclear development program. The first reactor was the Aircraft Reactor Experiment

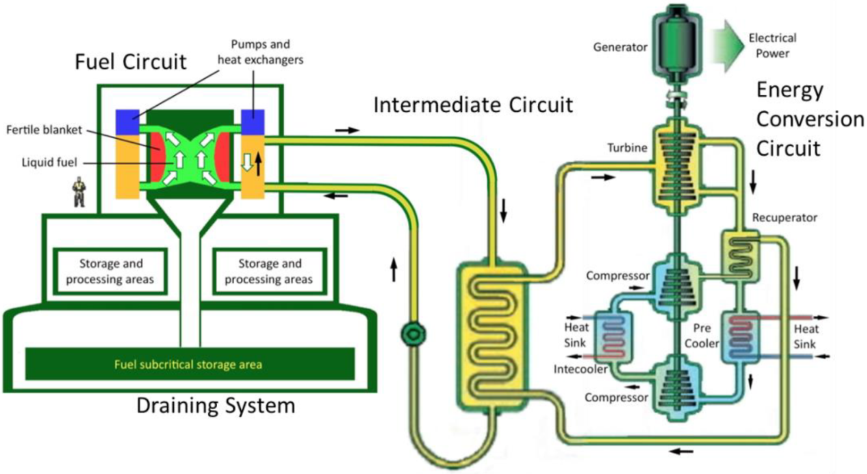

Figure 1.1: Design of the MSFR power plant (from [9]).

(ARE) operated up to 2.5 MWt [11]. The fuel for this reactor experiment was a mixture of the fluorides of sodium, zirconium, and uranium. During 10 years of research, numerous technological challenges have been tackled and a small test reactor, called Molten Salt Reactor Experiment (MSRE) [12, 13], was built and went critical in 1965 generating 8 MWt. This reactor operated with a fuel containing fluorides of beryllium and lithium at 650°C and at atmospheric pressure. The knowledge acquired resulted in the design of a new conceptual breeder reactor, the Molten Salt Breeder Reactor (MSBR)[4]. The fuel for MSBR was $^{233}UF_4$ or $^{235}UF_4$ dissolved in a mixture of LiF and BeF_2 with the fertile material being ThF_4, dissolved in the same or in a separate blanket salt. Despite the success of this technology, the research program was terminated in the early 1970s and little advance was made until 2002. The selection of the MSR as one of the six Generation IV reactors has contributed to an increase of interest and a renaissance of research in this concept.

1.3. MOLTEN SALT FAST REACTOR FUEL

A fundamental step for the design and safety assessment of the MSFR is the selection of the reference molten salt fuel composition. The right choice of the fuel salt is a very complex issue that influences all the other design choices by defining the operation parameters (temperature and pressure) and the reprocessing scheme [14]. Different criteria must be taken into account.

These criteria include neutronic properties (i.e. cross-sections), thermo-chemical and transport properties with major emphasis on the melting temperature, vapour pressure, heat capacity, density, as well as corrosion and fuel reprocessing capability. The class of compounds that best fulfils the above mentioned criteria are fluorides [15], which are considered as primary choice. Concerning the MSFR, the fuel is a multi-component fluoride mixture which has been proposed based on the physico-chemical properties of the fluoride salts and neutronic calculations [16]. Components that are considered for the start-up salt are ThF_4, UF_4 and PuF_3, in which ^{232}Th serves as the fertile material to breed ^{233}U. UF_4 is the fissile material, which is important for the control of the redox potential of the fuel via the UF_4/UF_3 ratio; and PuF_3 is the fissile material for startup, mainly represented by the ^{239}Pu isotope [17]. These three components are dissolved in a molten fluoride matrix and the choice and exact concentration of all the components are selected based on the following criteria:

- Melting temperature. In the selection of fuel and coolant, the melting point is important for determining of the operating temperature of the reactor. A low melting temperature is beneficial since it allows a low operating temperature of the reactor, decreasing the corrosion rate of the structural material by the fluoride salt. A low melting point decreases also the risk of freezing or precipitation of the salt [18].

- Vapour pressure. A low vapour pressure of the fuel means that the reactor can operate at low pressure allowing a smaller and thinner containment. Furthermore, since the primary and secondary circuit are at low pressure (i.e. lower than 5 bar) [19], a salt leakage does not result in an explosion.

- Boiling point. A boiling point much higher that the melting point decreases the possibility that the pressure in the primary system increases [19].

- Neutronic properties. The fuel must allow the reactor to be critical. Parameters to consider should be the thermal feedback coefficients, the effective fraction of delayed neutron, and the actinide solubility (the salt must dissolve enough fissile material at operation temperature to be critical without formation of solid precipitates).

- Heat capacity. This parameter determines the amount of energy the salt can carry in the system. A high heat capacity has the advantage that more energy can be stored in the salt. The volumetric heat capacity, obtained by multiplying heat capacity and density, is used to determine the reactor size, since the specific amount of heat it will store is known [20].

- Thermal conductivity. Since the molten fuel salt serves also as a coolant [21], its efficiency in transferring a large amount of heat defines the efficiency of the MSR. Therefore, a high thermal conductivity of the salt is desirable. Furthermore, the knowledge of the thermal conductivity helps to understand the distribution of the heat and the thermal gradients in the primary circuit.

- Density. The density must be taken into account for heat transfer calculations since it affects the volumetric heat capacity and the thermal conductivity.

- Viscosity. The viscosity of a fluid defines how easily the fluid flows. A small viscous fluid requires a low amount of energy to be pumped through the circuit.

This PhD research focuses on the experimental measurement of thermodynamic properties of molten salts. The scarcity of reliable data on the thermal properties of molten fluoride fluids seriously hampers the research on MSFRs. To remedy this situation, one of the work packages of SAMOFAR is devoted to experimentally obtain safety-related data of the fuel salt. The ultimate goal of this PhD was to develop methods for the determination of thermodynamic properties of the salt and to measure these properties for various salt compositions.

Within the studied thermodynamic properties, the melting point was measured for PuF_3 and one of the MSFR fuel mixtures, selected following the criteria such as neutronic properties, melting temperature, redox potential, physico-chemical properties, as explained in [22].

The thermal conductivity was measured on solid salt because a solid salt layer can be formed under cooling conditions that may add a significant heat resistance during transient conditions. An accurate measurement of viscosity is necessary to predict the flow and turbulent heat transfer of the fuel salt through the reactor circuit. While facilities for the measurement of the melting point, the concentration of the cations in water and thermal conductivity exist, the facility for the measurement of the viscosity had to be developed. Current techniques for measuring the viscosity could not be used for molten salts due to the small amount of fuel salt available, the radioactivity of the samples and their corrosiveness.

New crucibles for the melting point measurement of PuF_3 were designed in-house and new crucibles in glassy carbon were used for melting the salt and creating pellets for the thermal diffusivity measurement, for which also a new method of preparation of the pellets was developed. A number of difficulties were encountered in the measurement of the properties of molten salts:

- The high melting points and wide extent of the liquid state of the fluoride salts establishes a wide temperature range of experimental interest between 500°C and 1200°C.
- Most of the common materials available for the construction of an experimental apparatus corrode in the molten fluoride salts and special materials are needed.
- In the presence of even small amount of oxygen or water vapour, the corrosion rates are greatly accelerated.
- Since these salts in the molten state combine strongly with atmospheric oxygen and water vapour, it is necessary to maintain the molten salts in an inert atmosphere.
- The fluid viscosity in the temperature range of interest is low, varying from approximately 0.002 to 0.015 Pa·s. This requires rather sensitive methods.
- Since we are dealing with high radio-toxic salts, only a small amount of sample can be used. Moreover, since the salts have a high density, a small volume contains a significant amount of fissile elements.

These difficulties impose severe requirements on the measuring equipment by limiting the choice of techniques, construction materials, and instrumentation and by complicating the experimental manipulation of the apparatus.

1.4. DEVELOPMENT AND IMPROVEMENT OF TECHNIQUES TO DETERMINE THE SALT PROPERTIES

The final goal of this thesis is to develop methods for the determination of the most important thermodynamic properties of the salt and to measure these properties for various salt compositions. The knowledge of these properties for various salt compositions as a function of the temperature helps in the understanding of the behaviour of the selected fuel compositions for the reactor applications.

The scope of this thesis is to present techniques that might be applicable for the thermo-chemical characterization of molten salt systems. The techniques selected and developed in this thesis will provide relevant data for understanding the fluid flow and heat transfer; which are important for this kind of reactor. The properties such as thermal conductivity, melting point, viscosity and dissolution of salt in water are necessary for understanding the behaviour of the salt in nominal and accidental conditions. The techniques usually used for the measurements of properties such as thermal conductivity or viscosity are not always usable for molten salts. In those cases, the goal is to develop methods for determining these properties.

At TU Delft a novel technique for measuring the viscosity was developed and the technique was applied on fluids with similar viscosity as the molten fuel salts. At JRC-Karlsruhe the laser flash method was optimized for the determination of the thermal diffusivity of solid fuel salts. Other techniques, such as differential scanning calorimetry, X-ray diffraction, scanning electron microscopy, inductively coupled plasma atomic emission spectroscopy, were also applied in the nuclear laboratory of JRC-Karlsruhe on LiF-ThF_4 salts with additions of PuF_3 and UF_4. Complementing the overview of the salt properties the melting point of liquid fluorides containing uranium, thorium and plutonium was measured using the calorimetric facilities coupled with the well-developed encapsulation technique that prevents the evaporation of salts during the high temperature experiment [23]. The dissolution of the fuel salt in water was studied using the elemental analysis, inductively coupled plasma - optical emission spectrometry, to determine the variation in time of the concentration of the salt in water.

1.5. THESIS SYNOPSIS

The thesis presents both new methods for measuring the properties of molten salts and established methods for measuring the melting point and the dissolution of the salt in water. The second chapter focuses on the melting point measurement of PuF_3 and of LiF-ThF_4-UF_4-PuF_3 (77.5-6.6-12.3-3.6 mol%), a molten salt mixture considered as a key system for the MSFR concept. While for the molten salt mixture no experimental data were available, for PuF_3 only few data could be found - the latest from 1951 [24]. Given the importance of this system for the MSFR and the importance of the melting point of PuF_3, we decided to measure them via Differential Scanning Calorimetry. The innovation in this study is in the use of a newly developed crucible, selected based on its corrosive resistance at high temperature.

Chapter 3 focuses on the determination of the thermal diffusivity of fluoride salts in the solid phase. Most of the data in literature are on the thermal diffusivity of molten salts in their liquid phase. This is of major interest, but the thermal diffusivity of solid salts is equally important in case of overcooling of the reactor core that can result in fuel salt solidification. To understand the influence of a solid crust formation on the surrounding materials and its addition to heat transfer resistance, it is important to know the thermal diffusivity of this solid salt. No data were published in literature except for LiF [25, 26]. For this measurement we had to develop a new method for the preparation of the pellets used for the thermal diffusivity measurements.

In chapter 4, the development of a ultrasonic viscometer is presented. Previously, experimental groups have developed instruments based on different techniques for measuring the viscosity of molten salts, but requiring a large amount of fluid or operating at a low accuracy. The innovation of the ultrasonic viscometer is in its sensitivity at low viscosities, in the small volume of liquid necessary for an experiment, and in the suitability of this instrument for harsh materials. In this chapter, the characteristics of this viscometer, together with the measured viscosity of fluids with viscosities similar to that predicted for the molten fuel salt are presented.

In chapter 5 of this thesis, an established technique for measuring the concentration of elements (Inductively Coupled Plasma Optical Emission Spectroscopy) is used to determine the dissolution of solid MSFR fuel salts in water. The accidental scenario in which molten fuel salt and water come into contact is considered. A series of experiments were performed to simulate the situation of fuel leakage in water. We investigated the dissolution of spent fuel salt (LiF-ThF_4 and LiF-ThF_4-UF_4) in water, as well as the dissolution of FLiNaK, the ternary eutectic alkaline metal fluoride salt mixture LiF-NaF-KF (46.5-11.5-42 mol %) considered as a coolant for MSFR.

A summary of the results and the main outcomes are discussed in Chapter 6. A selection of promising methods is finally presented.

REFERENCES

[1] R. Pachauri, M. Allen, V. Barros, J. Broome, W. Cramer, R. Christ, J. Church, L. Clarke, Q. Dahe, P. Dasqupta, N. Dubash, O. Edenhofer, I. Elgizouli, C. Field, P. Forster, P. Friedlingstein, J. Fuglestvedt, L. Gomez-Echeverri, S. Hallegatte, G. Hegerl, M. Howden, K. Jiang, B. Jimenez Cisneros, V. Kattsov, H. Lee, K. Mach, J. Marotzke, M. Mastrandrea, L. Meyer, J. Minx, Y. Mulugetta, K. OBrien, M. Oppenheimer, J. Pereira, R. Pichs-Madruga, G.-K. Plattner, H.-O. Pörtner, S. Power, B. Preston, N. Ravindranath, A. Reisinger, K. Riahi, M. Rusticucci, R. Scholes, K. Seyboth, Y. Sokona, R. Stavins, T. Stocker, P. Tschakert, D. van Vuuren, and J.-P. van Ypersele, *Climate change 2014 synthesis report. contribution of working groups I, II, and III to the fifth assessment report of the Intergovernmental Panel on Climate Change* (IPCC, 2014).

[2] G. Steinhauser, A. Brandl, and T. E. Johnson, *Comparison of the chernobyl and fukushima nuclear accidents: A review of the environmental impacts,* Science of The Total Environment **470-471**, 800 (2014).

[3] *GEN-IV International Forum - Annual Report 2015,* Tech. Rep. (GIF, 2015).

[4] E. S. Bettis and R. C. Robertson, *The design and performance features of a single-fluid molten-salt breeder reactor,* Nuclear Applied Technology (1970).

[5] J. C. Gehin and J. J. Powers, *Liquid fuel molten salt reactors for thorium utilization,* Nuclear Technology **194**, 152 (2016), https://doi.org/10.13182/NT15-124 .

[6] L. Luzzi, V. Di Marcello, and A. Cammi, *MOLTEN SALT REACTOR TECHNOLOGY,* (2011).

[7] T. J. Dolan, *1 - introduction,* in *Molten Salt Reactors and Thorium Energy*, edited by T. J. Dolan (Woodhead Publishing, 2017) pp. 1 – 12.

[8] A. E. Waltar and A. B. Reynolds, *Fast breeder reactors* (New York : Pergamon Press, 1981).

[9] M. Allibert, D. Gèrardin, D. Heuer, E. Huffer, A. Laureau, E. Merle, S. Beils, A. Cammi, B. Carluec, S. Delpech, A. Gerber, E. Girardi, J. Krepel, D. Lathouwers, D. Lecarpentier, S. Lorenzi, L. Luzzi, S. Poumerouly, M. Ricotti, and V. Tiberi, *Description of initial reference design and identification of safety aspects,* (2016), work Package 1, Deliverable D1.1, SAMOFAR (Safety Assessment of the MOlten Salt FAst Reactor) European project, Contract number: 661891.

[10] W. B. Cottrell, H. E. Hungerford, J. K. Leslie, and J. L. Meem, *Operation of the aircraft reactor experiment,* (1955).

[11] E. S. Bettis, R. W. Schroeder, G. A. Cristy, H. W. Savage, R. G. Affel, and L. F. Hemphill, *The aircraft reactor experimentdesign and construction,* Nuclear Science and Engineering **2**, 804 (1957), https://doi.org/10.13182/NSE57-A35495 .

[12] *Molten-salt reactor program: Semiannual progress report. ORNL-4449*, Tech. Rep. (ORNL, 1970).

[13] P. N. Haubenreich and J. R. Engel, *Experience with the molten-salt reactor experiment,* Nuclear Applications and Technology **8**, 118 (1970), https://doi.org/10.13182/NT8-2-118 .

[14] M. Brovchenko, E. Merle, H. Rouch, F. Alcaro, M. Allibert, M. Aufiero, A. Cammi, S. Dulla, O. Feynberg, L. Frima, O. Geoffroy, V. Ghetta, D. Heuer, V. Ignatiev, J. Kloosterman, D. Lathouwers, A. Laureau, L. Luzzi, B. Merk, P. Ravetto, A. Rineiski, P. Rubiolo, L. Rui, M. Szieberth, S. Wang, and B. Yamaji Optimiza, *Optimization of the pre-conceptual design of the MSFR. Deliverable D2.2, EVOL (Evaluation and Viability Of Liquid fuel fast reactor system) European project, Contract number: 249696,* .

[15] W. R. Grimes, *Molten salt chemistry,* Nuclear Applications and Technology **8**, 137 (1970).

[16] L. David, *Molten salt reactors: A new beginning for an old idea,* Nuclear Engineering and Design **10**, 1644 (2010).

[17] S. Delpech, E. Merle-Lucotte, D. Heuer, M. Allibert, V. Ghetta, C. Le-Brun, X. Doligez, and P. G., *Reactor physic and reprocessing scheme for innovative molten salt reactor system,* Journal of Fluorine Chemistry (2009).

[18] D. E. Holcomb, G. F. Flanagan, B. W. Patton, J. C. Gehin, R. L. Howard, and T. J. Harrison, *Fast Spectrum Molten Salt Reactor Options, ORNL/TM-2011-105*, Tech. Rep. (2011).

[19] B. M. Elsheikh, *Safety assessment of molten salt reactors in comparison with light water reactors,* Journal of Radiation Research and Applied Sciences **6**, 63 (2013).

[20] J. Barnes, R. Coutts, T. Horne, and J. Thai, *Characterisation of Molten Salts for Application in Molten Salt Reactors,* Energy Science & Technology **6** (2019), 10.5130, https://doi.org/10.5130/pamr.v6i0.1546 .

[21] C. N. C. Z. Bahri, W. M. Al-Areqi, M. I. F. M. Ruf, and A. A. Majid, *Characteristic of molten fluoride salt system LiF-BeF$_2$ (FLiBe) and LiF-NaF-KF (FLiNaK) as coolant and fuel carrier in molten salt reactor (MSR),* AIP Conference Proceedings **1799**, 040008 (2017), https://aip.scitation.org/doi/pdf/10.1063/1.4972932 .

[22] O. Beneš, E. Capelli, M. Allibert, M. Brovchenko, D. Heuer, R. J. M Konings, and S. Delpech, *Selection of the MSFR fuel salt composition Evaluation and Viability of Liquid Fuel Fast Reactor System EVOL Contract (grant agreement) number: 249696,* (2015).

[23] O. Bene, R. J. M. Konings, S. Wurzer, M. Sierig, and A. Dockendorf, *A DSC study of the NaNO$_3$KNO$_3$ system using an innovative encapsulation technique,* Thermochimica Acta **509** (2010).

[24] E. F. Westrum and J. C. Wallmann, *Melting point and heat of sublimation of PuF$_3$ 1,* Journal of the American Chemical Society **73**, 3530 (1951).

[25] H. Chang, M. Altman, and R. Sharma, *The Determination of Thermal Diffusivities of Thermal Energy Storage Materials,* Transaction of ASME, Journal of Engineering for Power , 407 (1967).

[26] X. Yu and A. M. Hofmeister, *Thermal diffusivity of alkali and silver halide crystals as a function of temperature,* Journal of Applied Physics **109**, 033516 (2011).

2

MELTING POINT OF FLUORIDE FUEL SALTS

Every problem is an opportunity in disguise.

John Adams

The Molten Salt Fast Reactor (MSFR) concept operating with PuF_3 as fissile material considers as fuel salt a mixture of LiF-ThF_4-UF_4-PuF_3 (77.5-6.6-12.3-3.6mol%). The melting point of this salt mixture has been measured by differential scanning calorimetry (DSC). The measured solidus and liquidus temperature were compared to the optimized pseudo binary phase diagram of LiF-ThF_4 with fixed amount of UF_4 and PuF_3 as in the fuel mixture molar ratio.

The melting point of PuF_3 was studied for the first time in this work by DSC. Adapted DSC crucibles, in ceramic material (BN), graphite, glassy carbon and BN plus liner in Pt and W, were made for this measurement to reach the high melting temperature of PuF_3. X-ray Diffraction analysis was used to demonstrate the purity of the sample before the DSC measurement, which is particularly important for a reliable determination of the melting point.

Parts of this chapter have been published in Journal of Nuclear Materials **527**, 151780 (2019) [1].

2.1. INTRODUCTION

Molten Salt Fast Reactors (MSFR) aim to use as fuel a mixture of fluoride salts, LiF-ThF_4-UF_4-PuF_3. This option is the fuel considered in the SAMOFAR project for the Molten Salt Fast Reactor (MSFR). In this reactor design, it is possible to use a closed thorium fuel cycle (^{232}Th/^{233}U) which offers great benefits in terms of sustainability of the Generation IV reactors [2, 3]. The initial fuel composition considered for Molten Salt Fast Reactors (MSFR) depends on the purpose of the reactor itself that can be breeder or burner [4]. The primary composition is a binary mixture composed of 77.5 mol% of lithium fluoride and 22.5 mol% of actinide fluorides. The last ones are ThF_4, UF_4 and other actinide fluorides. Fissile isotopes of elements have to be added to the initial fuel load for the reactor start-up because ^{232}Th is not a fissile isotope. The initial fuel load may comprise ^{233}U, ^{235}U enriched (between 3% and 5%) natural uranium, or the transuranic (TRU) elements currently produced in PWRs.

Plutonium produced in current LWRs (Light Water Reactor) can also be used as PuF_3 for the MSR start-up as demonstrated in the early studies at Oak Ridge National Laboratories [5]. Due to the possibility to burn plutonium, this is promising for reducing the waste from a LWR [6, 7].

The limitation of this starting mode lies in the Pu solubility limit in the lithium fluoride used as solvent for the fertile (ThF_4) and fissile (UF_4 and PuF_3) components in the salts. The initial molar proportion of Pu in this configuration is chosen based on the neutronic and physico-chemical requirements. The salt composition chosen is therefore LiF-ThF_4-UF_4-PuF_3 (77.5-6.6-12.3-3.6 mol%).

In this chapter, we present the melting point measurement of the LiF-ThF_4-UF_4-PuF_3 system and of pure PuF_3.

While the melting point of the MSFR fuel mixture was never measured before, few data could be found for the melting point of PuF_3. Its melting point was measured for the first time in 1949 [8, 9]. Through an effusion technique, the equilibrium vapor pressure was measured and the deviation from the linearity of the log p vs 1/T (the Clausius-Clapeyron equation) was represented as two lines intersecting at 1442 ± 9 K that was interpreted as the melting point of PuF_3. This value must be corrected to the International Temperature Scale of 1990 (ITS-90), giving 1443 ± 9 K. This temperature is much lower than the one that would have been expected for this fluoride, by comparison with the other actinide fluorides. Another attempt made by [10] reports values of 1708, 1833, 1908 K (corrected to ITS-90: 1709, 1834, 1909 K). PuOF was formed in all these experiments as was seen by XRD. In 1950, Westrum and Wallmann [11] measured the melting point of PuF_3 with an optical pyrometer. They observed directly the fusion and solidification point and obtained a value for the melting point of 1699 ± 2 K (1700 ± 2 K in ITS-90). The samples were analyzed after the melting point measurements showing impurities in PuF_3. This melting point was also determined from the mass spectrometry analysis by knudsen effusion mass spectrometry (KEMS) as 1705 ± 10 K [1]. The measurement of the PuF_3 melting point was never measured before with the differential scanning calorimeter, the usual method for melting point measurements. Due to its relatively high melting point, the material of the crucibles usually used for these kind of experiments have to be modified. We investigated materials, both ceramic and metals, chemically compatible to the salt and resistant at high temperature. One of the aims of this work was to measure with good reproducibility the melting point of PuF_3 and identify the materials usable for the crucible for measuring its melting point. In second place we also wanted to measure the melting point of the molten fuel salt mixture and compare it with the modeled phase diagram.

2.2. METHOD

2.2.1. SAMPLE PREPARATION AND CHARACTERISATION

PuF_3 was synthetized by hydrofluorination of PuO_2. The synthesis procedure for this salt is shown in detail in [12] and consisted of two steps, the fluorination of PuO_2 and the production of PuF_4 that is consequently reduced to PuF_3 using Ar-H_2 (6%):

$$PuO_2 + 4HF \longrightarrow PuF_4 + H_2O$$

$$PuF_4 + \frac{1}{2}H_2 \longrightarrow PuF_3 + HF$$

The prepared PuF_3 was used for the study of the melting point of this pure component as well as for the melting point measurement of the MSFR salt mixture. For the last one, ThF_4 and UF_4 were also synthetized by hydrofluorination of, respectively, ThO_2 and UO_2 [13]. The LiF used for the mixture was purchased from Alfa Aesar and had a metal base purity of 99.99%. All the fluoride salts were stored and handled in argon glove boxes. Fluorides have the tendency to absorb water and, in particular, the actinide fluorides form oxyde and hydroxide in air [14, 15]. The argon gloveboxes where the salts were prepared had very low concentrations of water and oxygen, being less than 1 ppm. To remove the residual moisture from the purchased LiF, it was purified before preparing the mixture. The purification consisted of a heating cycle at 400°C for 4 hours in inert Argon atmosphere. For the actinide fluorides another purification was performed, described in [13]. The purity of the end-members was checked before preparing the mixture using the DSC method. The salts were considered pure if they showed one single peak at ± 2 K from the literature melting point. A single peak is also indication of the melting point of the salt, as described in [12]. The salt mixture LiF-ThF_4-UF_4-PuF_3 was prepared mixing the end members in an agate mortar into a fine powder. The salt mixture was considered homogeneous after 10 minutes of grinding.

2.2.2. DIFFERENTIAL SCANNING CALORIMETRY

The melting point of PuF_3 and the equilibrium data of the MSFR mixture were measured by Differential Scanning Calorimetry (DSC). The DSC is an established techniques for measuring phase transitions as melting and crystallization. The technique is based on the measurement of the heat flow between a sample and a reference during constant heating. A DSC has two compartments, one for the reference and one for the sample, that are subjected to the same controlled temperature program.

The instrument used in this study is a SETARAM Multidetector High Temperature Calorimeter (MDHTC96). The samples were heated and cooled in a furnace at constant rate, while a detector measures the heat flow change between the sample and the reference crucible as a function of temperature. The DSC sensor used in this study is based on series of B-type thermocouples that allow measurements from room temperature to

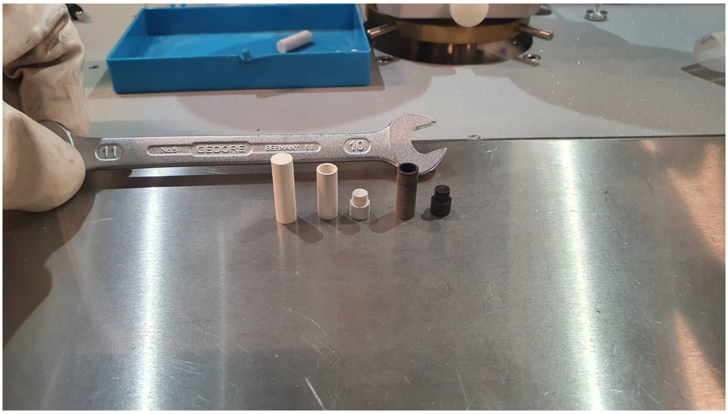

Figure 2.1: BN (left side) and graphite (right side) crucibles used for the melting point measurement.

1600°C.

The samples of MSFR fuel were encapsulated in crucibles developed in JRC-Karlsruhe to avoid vapour release [16]. The crucibles, designed for the calorimeter installed in our laboratories (SETARAM MD-HTC96), are made of stainless steel with a nickel liner in which the sample is placed. The nickel liner was placed in the stainless steel crucible as a barrier for the instrument detector against the corrosive fluoride vapours.

Due to the high melting temperature of PuF_3, other materials had to be used. Tests were done with crucibles made out of boron nitrite, graphite, glassy carbon and boron nitrate with liner in platinum and tungsten. Figure 2.1 shows three crucibles used for the melting point measurements of PuF_3, the two on the left side in BN and the one on the right side in graphite. The crucibles have a inner diameter of 1 cm and a height of 4 cm.

All these materials were chosen for their resistance to the molten salts. All the crucibles were baked in an argon filled furnace up to 400°C before the DSC experiments to evaporate the oxygen in the crucibles. However, it was still possible that oxygen was present inside the bulk of the materials.

The whole preparation of the samples and their encapsulation in the crucibles was performed inside argon glove boxes to avoid reaction of the samples with water or oxygen. Around 100 mg of sample was placed in the DSC crucibles. The heating chamber was purged and evacuated to very low vacuum twice before the experiments to eliminate possible impurities and prevent the oxidation of the crucible at high temperature.

The heating cycles consisted of ramps at a constant rate of 10 K/min, 5 K/min and 2 K/min to assess repeatability and to better observe the phase transition. The slowest heating rates allowed to observe more precisely the phase transition when this was not visible at the heating rate of 10 K/min. The maximum temperature reached was up to above the predicted melting temperature of the samples.

For the MSFR fuel samples, at least two heating ramps were performed. The first one was done to melt and completely homogenize the mixture. The second and third heating ramp were used for the measurements. The solidus temperature was identified from the onset of the peak, while the liquidus was determined from the change of slope in the DSC heat flow curve.

The PuF_3 melting point could be detected from all the DSC curves. Since PuF_3 is a pure compound, there was no need to homogenize it as was done for the mixtures for the MSFR fuel salt. The melting point could therefore be detected already from the first heating ramp. For PuF_3, the melting temperature was identified as the onset of the peak during heating. The experimental data were acquired and post-processed with the Calisto software v1.10 supplied by Setaram. The measured temperature values were corrected by a temperature calibration performed before the measurements using several reference metals (Sn, Pb, Zn, Al, Ag, Cu).

2.2.3. X-RAY DIFFRACTION

The diffraction pattern of the samples was measured firstly to check for the purity of the end members before preparing the mixtures. XRD was also used for observing the formation of oxides after a DSC measurement. The patterns were measured using a Bruker D8 X-ray diffractometer mounted in a Bragg-Brentano configuration. The diffractometer was equipped with a curved Ge monochromator (1, 1, 1), a ceramic copper tube (40 kV, 40 mA) and a LinxEye linear position sensitive detector. The diffraction patterns were recorded at room temperature by step scanning in the angular range 2θ from 7°to 110°. The X-ray diffraction data were analysed after the measurement using the FullProf suite [17].

For the XRD measurement, approximately 20 mg of sample was finely ground to powder in an agate mortar and mixed with an epoxy resin. The sample was embedded in the resin to avoid dispersion of the radioactive powder and to protect the hygroscopic sample from air.

2.3. RESULTS

2.3.1. MELTING POINT OF PuF_3

The melting point of PuF_3 was measured in crucibles of different materials (boron nitrite, graphite, glassy carbon and boron nitrate with liner in platinum and tungsten) to establish the best possible way to measure the melting point of high melting compounds. The purity of PuF_3 was checked before the melting point measurement with XRD. The XRD pattern of the freshly prepared PuF_3, in Figure 2.2, showed a pure compound with the PuF_3 P-3c1 phase only.

Firstly, PuF_3 was measured in a crucible of BN, a ceramic material with a high melting point and resistant to the corrosion of fluoride salts. In Figure 2.3 the DSC curves for two samples of PuF_3 are reported. Two cycles for each one of the two samples were performed. The melting point corresponds to the onset of the peak, determined by the Calisto software using the changes of the slope in the signal. The onset is shown in Figure 2.3 by the intersection of the baseline of the heat flow signal and the tangent at the beginning of the melting. For a single component, a single endothermic peak in the heat flow versus the temperature signal should be visible if the compound is pure. Two peaks are visible for the first heating curves (BN-1.1 and BN-2.1) of both PuF_3 samples. The presence of two peaks in the curves might indicate the presence of some impurities, PuO_2 or metallic contaminants, which affects the melting behaviour of PuF_3. Both samples

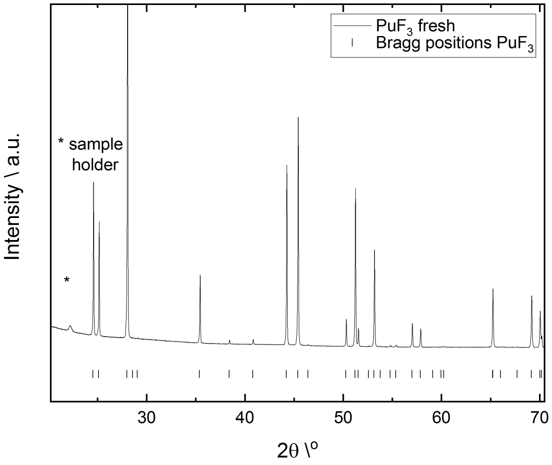

Figure 2.2: XRD pattern of fresh plutonium fluoride fitted with the PuF_3 Bragg positions (black lines)

used for the measurements shown in Figure 2.3 came from the same batch of PuF_3, that seemed pure as shown by the XRD (Figure 2.2). The second peak for the curves of BN-1.1 and BN-2.1 is believed to belong to a process happening during the melting. Likely a reaction of PuF_3 with oxygen, possibly present in the BN crucibles, might have happened at high temperature. More analysis after the melting point measurement are necessary to determine with certainty the origin of the two peaks.

All the measurement were calibrated using standards with known melting point. The first peak for the BN-1.1 sample has its onset at 1654 ± 2 K, calculated from the data in Figure 2.3 after calibration, while BN-2.1 has its onset at 1648 K (onset of the first peak). In the last case, the uncertainty is higher than 2 K, the usually considered uncertainty for these DSC measurements [18]; the peak is in-fact broader than the usual DSC peaks and it is more difficult to identify the onset of the peak. One single peak with the onset at a higher temperature, respectively 1676 and 1687 ± 2 K for BN-1.2 and BN-2.2, is visible for both the second heating curves of the two samples.

From the XRD pattern of PuF_3, in Figure 2.4, after melting in the BN crucible (only the sample BN-1 was analysed), it was found that traces of PuOF were present in the salt. It is possible that the second peak visible in the first heating curves (BN-1.1 and BN-2.1) and the peak on the second heating curves (BN-1.2 and BN-2.2) are relative to the formation of PuOF. The formation of plutonium oxyfluoride explains the different melting point found by DSC. During the melting measurement, it is not known when exactly PuOF started forming shifting the heat flow signal measured by DSC.

In Figure 2.5, the DSC curves of PuF_3 melted in crucibles of graphite and glassy carbon are shown. Two heating curves (graphite-1 and graphite-1.1) were recorded for the sample melted in the graphite crucible. Also in this case the first heating curve recorded for the sample melted in the graphite crucible showed a lower melting point, 1647 ± 2

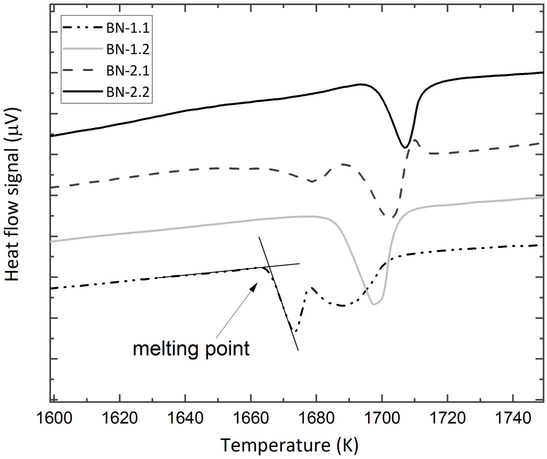

Figure 2.3: Determination of the melting point of two samples of PuF_3 in BN crucibles. BN-1.1 and BN-1.2 represent the measurement in one crucible, while BN-2.1 and BN-2.2 are relative to a second BN crucible.

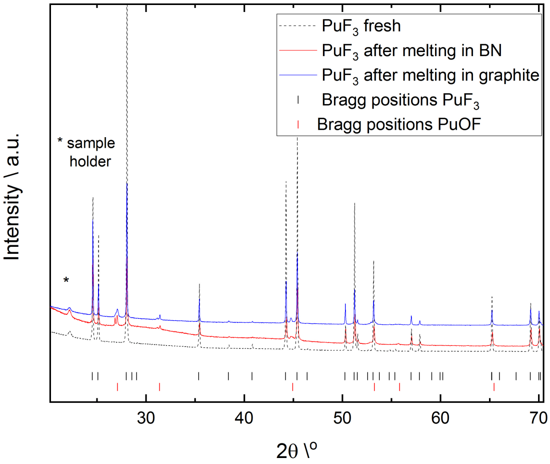

Figure 2.4: XRD pattern of plutonium fluoride before (black dashed curve) and after melting point measurement in the BN crucible (red curve) and graphite crucible (blue curve). The pattern of fresh PuF_3 was fitted with the PuF_3 Bragg positions (black lines), while the salts after melting point measurements show also the presence of PuOF (red lines).

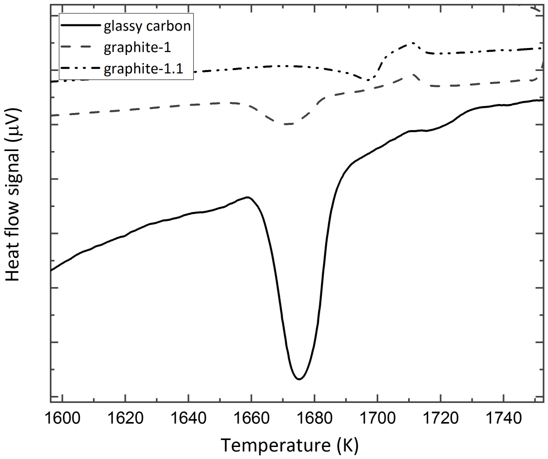

Figure 2.5: Determination of the melting point of two samples of PuF_3 in graphite and glassy carbon crucibles.

K, with respect to the melting point shown by the second heating curve, 1672 ± 2. The uncertainty of the onset point has been evaluated as 2 K, based on the results of the calibration and on the analysis of the peak. Figure 2.4 shows the XRD pattern of this sample after melting (blue line in Figure 2.4). The peaks relative to PuOF are visible, therefore also for this sample, in the graphite crucible the second heating curve might be influenced by the formation of PuOF. A third DSC curve relative to PuF_3 melted in a glassy carbon crucible is shown in Figure 2.5. In this case the onset of the peak is at 1658 ± 2 and the peak is much more intense than the previous two, the reason being that more salt, ca. 200 mg, was placed in the glassy carbon crucible. This salt was used after the melting for preparing a disk for the thermal diffusivity measurement, also presented in this thesis in Chapter 3. For this sample, a XRD has not yet been performed after the melting point measurement and it is not possible to say if PuOF was formed.

Considering that PuOF was always formed when melting PuF_3 in BN and graphite crucibles, we repeated the measurement of the melting point in crucibles of BN with a liner of Pt, firstly, and of W, secondly, both metals considered chemically resistant to the molten salt. Figure 2.6 shows one heating curve for the sample melted in the BN crucible with the liner in Pt, where the melting point was found to be 1683 ± 2 K. Two heating curves are shown for the sample molten in the BN crucible with a W liner, the first (BN + W liner 1.1) was done with an heating rate of 10 K/min. For this measurement the heating cycle was ended right after the melting temperature of PuF_3, this explains why the heat flow curve does not return to the baseline after the offset of the peak. The measurement was repeated with a heating rate of 5 K/min (BN + W liner 1.2) to test the repeatability of the results at a different heating rate. The melting point was measured at 1682 K. The error for this last measurement might be higher than 2 K because the peak is broader than usually for a DSC measurement. The XRD analysis on these samples after

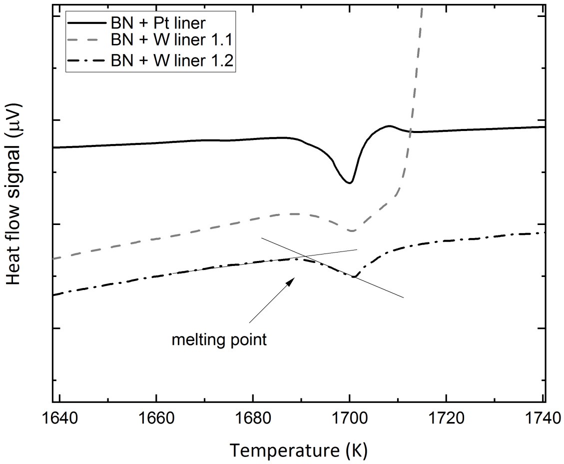

Figure 2.6: Determination of the melting point of two samples of PuF_3 in BN crucibles with a liner of platinum and tungsten.

melting was not performed because the sample molten in the BN crucible with Pt liner mixed with the Pt liner after melting and it was not possible to powder it and perform an XRD. The sample molten in BN and W liner has not been analyzed yet. Therefore it is not possible to demonstrate that PuOF was not formed. Nevertheless, observing the DSC curves, no other peaks are visible on this curves, a first indication that probably the samples did not form other compounds after the melting point measurement. The results for these measurements of Figure 2.6 are in better agreement respect to the other measurements in graphite, glassy carbon and BN crucible. The standard deviation among the measurement performed with the BN crucibles with liners is of 2 K, while it is 14 K among all the other measurements.

For all the measurements performed, the melting point was measured between 1647 and 1687 K, with a standard deviation bigger than the uncertainty of the melting measurement of 2 K. If we consider the two most reliable measurements only, the ones in the BN + Pt and W crucibles, the melting point of PuF_3 would be 1681 ± 2 K. The measurements performed with the BN + Pt and W liners are considered as the most reliable because of the single peak they showed also when repeated and because of the smaller standard deviation among the repeated measurements. The melting point of 1681 ± 2 K values is lower than the one measured by Westrum [11] of 1700 ± 2 K, where the uncertainty is the standard deviation among 11 measurements. Westrum used for the measurement a direct observation of the fusion point via a optical pyrometer. Tosolin [1] extrapolated the melting point as 1705 K, using KEMS. The melting point was extrapolated from the deviation of the linearity of the logarithm of the vapour pressure versus the inverse of the temperature. The intersection of two straight lines at the point where there was a deviation from the linearity, was considered as the melting point of PuF_3.

The reason for this discrepancy might be caused by the possible presence of contaminants in the salts, either the one used in this work or by Westrum and Tosolin. The salt was not further characterized after the melting point measurement.

Table 2.1 summarizes all the melting temperatures obtained in this work.

Table 2.1: Melting temperatures of PuF_3 measured by DSC in this work.

Material of the crucible	Batch name	Mass sample	Temperature	XRD
		mg	K	
BN	BN-1.1	47.1	1654 ± 2	yes
BN	BN-1.2	-	1676 ± 2	yes
BN	BN-2.1	60.7	1649 ± 10	no
BN	BN-2.2	-	1687 ± 2	no
graphite	graphite-1	59.2	1647 ± 2	yes
graphite	graphite-1.1	-	1672 ± 2	yes
glassy carbon	glassy carbon	220.1	1658 ± 2	no
BN + Pt liner	BN + Pt liner	45.3	1683 ± 2	no
BN + W liner	BN + W liner 1.1	53	1679 ± 2	no
BN + W liner	BN + W liner 1.2	-	1682 ± 2	no

The XRD was measured for all the samples before the melting point measurement. The column of this table is referred to the XRD measured after melting point measurement.

2.3.2. PHASE TRANSITION OF THE MSFR FUEL SALT: LIF-THF$_4$-UF$_4$-PUF$_3$

Figure 2.7 shows the heating curve measured by DSC for the mixture LiF-ThF$_4$-UF$_4$-PuF$_3$ (77.5-6.6-12.3-3.6 mol%). The salt mixture was measured in the stainless steel crucible with nickel liner developed by Beneš et al. [19].

In figure two peaks are visible, indicating the solidus point or eutectic point (the first peak) and the liquidus point (the second broader peak). The solidus point for this composition, as shown in Figure 2.7, is retrieved by the onset of the first peak. The offset of the second broader peak indicates the liquidus point, when the salt becomes entirely liquid. The measured temperatures for the eutectic and the liquidus are respectively 776 ± 2 K and 893 ± 10 K. The uncertainties are given based on the instrument uncertainty and is based on the calculation of Hohne [18]. The pseudo binary phase diagram of LiF-ThF$_4$ with fixed amount of ThF$_4$ (6.6 mol%) and PuF$_3$ (3.6 mol %) shown in Figure 2.8 was calculated using the thermodynamic data from the JRCMSD database, presented by Capelli et al. [20]. The pseudo binary phase diagram was plotted using the thermodynamic software FactSage [21] In Figure 2.8, the experimental points obtained by DSC for the studied mixture are shown. The two points are plotted on the modeled pseudo binary phase diagram and the difference between the experimental and modeled temperature is calculated on Factsage. While the experimental solidus point agrees with the calculated phase diagram, the experimental liquidus point is about 40 K higher than

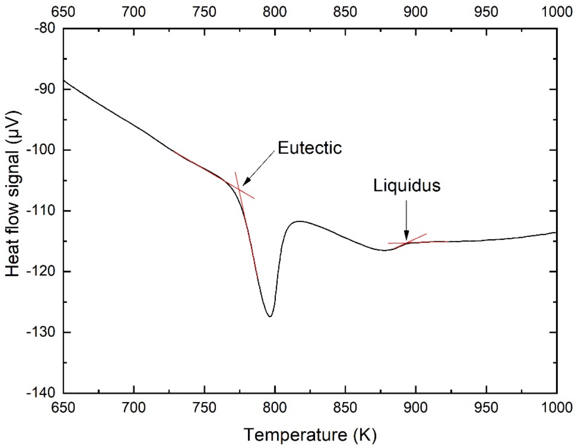

Figure 2.7: Heating curve of the molten salt mixture LiF-ThF_4-UF_4-PuF_3 (77.5-6.6-12.3-3.6 mol%). The heating rate was in this case 10 K/min.

the model, as shown by the distance between the experimental point and modeled line. Even considering the uncertainty of ± 10 K this difference is quite significant. It must be considered that a small error in the preparation of the salt might move the point closer to the LiF region of the phase diagram where there is a relatively steep liquidus. A difference of 1.5% towards the LiF component, slightly higher than the experimental uncertainty of the composition of ± 1.0 mol%, corresponds to a liquidus temperature shift of 40 K. This difference in the experimental versus calculated liquidus might suggest that the measurement has to be repeated with more precision of synthesis or that a correction in the thermodynamic database is needed.

2.4. CONCLUSIONS

This chapter presents the results on the melting temperature of PuF_3 and on the MSFR fuel mixture LiF-ThF_4-UF_4-PuF_3 (77.5-6.6-12.3-3.6 mol%). For both salts the melting temperature was measured by DSC. No experimental data were available in the literature for the MSFR mixtures, while only old data scattered between 1442 and 1909 K are available for PuF_3. For measuring the melting point of PuF_3, new crucible materials were tested. The crucible used for molten fluoride salts at JRC-Karlsruhe could not be used in the range of temperature where the melting point of PuF_3 was expected. A considerable effort was made to choose and manufacture a crucible in materials that could at the same time withstand the high melting temperature of PuF_3, avoid the formation of oxide and the corrosion due to the molten salts at high temperature. During the measurements we observed that the melting point of PuF_3 was influenced by the material of the crucibles in which it was molten. A difference of approximately 40 K between all the measurements was found: the measured melting point of PuF_3 was between 1647 and 1687 K. We noticed that it is important to check the purity of the sample before and after

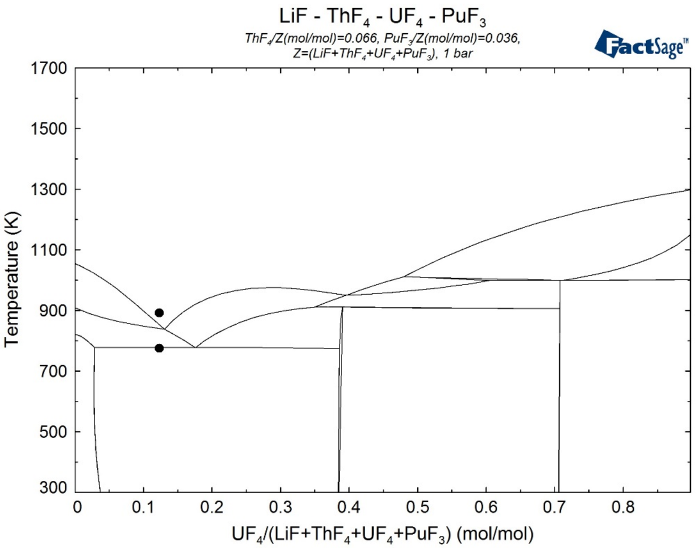

Figure 2.8: Pseudo binary phase diagram of LiF-UF_4 with fixed amount of ThF_4 (6.6 mol%) and PuF_3 (3.6mol%). The • represents the data measured in this work for the composition LiF-ThF_4-UF_4-PuF_3 (77.5-6.6-12.3-3.6 mol%).

DSC measurement by XRD. PuOF was formed when PuF_3 was melted in BN and graphite crucibles. The formation of the oxide phase was visible from both the DSC curves, where two peaks were present, and from the XRD patterns. We suggest to perform the XRD measurement also on the PuF_3 samples melted in Pt and W liners since this can confirm or not the oxidation of the sample after the melting point measurement. We also suggest to repeat the experiments in the crucible in BN plus W liner to optimize the melting point measurement.

For the MSFR mixture, the results were compared and plotted on the phase diagram modeled using the thermodynamic database assessed by Capelli et al. [20]. The measurement of the solidus temperature (776 ± 2 K) agrees well with the modeled phase diagram, while a difference of 40 K was found for the liquidus temperature (893 ± 10 K). This difference suggests a possible modification of the thermodynamic database or an experimental error in the salt mixture preparation.

The results presented in this work aim to support the safety assessment of the MSFR. The knowledge of the melting point of the salt mixture allows to avoid the risk of freezing of the fuel. The knowledge of the melting point of the end components allows to optimize the phase diagram and decreases the risk of solid precipitates.

2.5. ACKNOWLEDGEMENTS

The authors thank Daniel Bouexière for the XRD analyses. This work was supported by the by the Euratom research and training programme 2014-2018 SAMOFAR (Grant agreement No.661891) and by the ENEN+ project.

REFERENCES

[1] A. Tosolin, J.-Y. Colle, S. Mastromarino, P. Souek, L. Luzzi, R. J. M. Konings, and O. Bene, *Vaporization behaviour of a PuF_3 -containing fuel mixture for the Molten Salt Fast Reactor,* Journal of Nuclear Materials **527**, 151780 (2019).

[2] *A technology roadmap for generation IV nuclear energy system*, Tech. Rep. (U.S. DOE Nuclear Energy Research Advisory Committee and the Generation IV International Forum, 2002).

[3] *GIF, Annual Report 2015*, Tech. Rep. (GEN-IV International Forum, 2015).

[4] L. Mathieu, D. Heuer, E. Merle-Lucotte, R. Brissot, C. Le Brun, E. Liatard, J.-M. Loiseaux, O. Méplan, and A. Nuttin, *Possible Configurations for the Thorium Molten Salt Reactor and Advantages of the Fast Nonmoderated Version,* Nuclear Science and Engineering **161**, 78 (2009).

[5] W. R. Grimes, N. V. Smith, and G. M. Watson, *Solubility of Noble Gases in Molten Fluorides. I. In Mixtures of $NaFZrF_4$ (5347 mol%) and $NaFZrF_4UF_4$ (50464 mol%),* The Journal of Physical Chemistry **62**, 862 (1958).

[6] B. Merk and D. Litskevich, *On the burning of plutonium originating from light water reactor use in a fast molten salt reactor-A neutron physical study,* Energies **8**, 12557 (2015).

[7] E. Merle-Lucotte, D. Heuer, C. L. Brun, L. Mathieu, R. Brissot, E. Liatard, O. Méplan, and A. Nuttin, *Fast Thorium Molten Salt Reactors started with Plutonium,* in *ICAPP '06 : International Congress on Advances in Nuclear Power Plants. 6123* (Reno, Nevada, United States, 2006) p. 9.

[8] T. E. Phipps, R. L. Seifert, and O. C. Simpson, *The transuranium elements: research papers,* National Nuclear Energy Series Div IV **14 B** (1949).

[9] E. F. Westrum and J. C. Wallmann, *The melting point and the heat of sublimation of PuF_3, University of California, Radiation Laboratory. Contract No. W-7405-eng-48, UCRL-697*, Tech. Rep. (May 19, 1950).

[10] H. P. Robinson, *Manhattan Project Metallurgical Laboratory Report CN-2159*, Tech. Rep. (1944).

[11] E. F. Westrum and J. C. Wallmann, *The melting point and heat of sublimation of PuF_3 1,* Journal of the American Chemical Society **73**, 3530 (1951).

[12] A. Tosolin, P. Souek, O. Bene, J.-F. Vigier, L. Luzzi, and R. Konings, *Synthesis of plutonium trifluoride by hydro-fluorination and novel thermodynamic data for the PuF_3-LiF system,* Journal of Nuclear Materials **503**, 171 (2018).

[13] P. Souek, O. Bene, B. Claux, E. Capelli, M. Ougier, V. Tyrpekl, J.-F. Vigier, and R. J. Konings, *Synthesis of UF_4 and ThF_4 by HF gas fluorination and re-determination of the UF_4 melting point,* Journal of Fluorine Chemistry **200**, 33 (2017).

[14] C. Mandleberg and D. Davies, *The reaction of UF_4 with oxygen,* Journal of Inorganic and Nuclear Chemistry **20**, 58 (1961).

[15] S. Mukherjee, S. Dash, S. Mukerjee, and K. Ramakumar, *Thermodynamic investigations of oxyfluoride of thorium and uranium,* Journal of Nuclear Materials **465**, 604 (2015).

[16] O. Bene, R. J. M. Konings, S. Wurzer, M. Sierig, and A. Dockendorf, *A DSC study of the $NaNO_3KNO_3$ system using an innovative encapsulation technique,* Thermochimica Acta **509**, 62 (2010).

[17] J. Rodríguez-Carvajal, *Recent advances in magnetic structure determination by neutron powder diffraction,* Physica B: Physics of Condensed Matter **192**, 55 (1993).

[18] G. W. H. Höhne, W. Hemminger, and H.-J. Flammersheim, *Differential Scanning Calorimetry*, edited by S. B. Heidelberg (1996).

[19] O. Beneš, M. Beilmann, and R. J. M. Konings, *Thermodynamic assessment of the $LiFNaFThF_4UF_4$ system,* Journal of Nuclear Materials **405**, 186 (2010).

[20] E. Capelli, O. Bene, and R. Konings, *Thermodynamic assessment of the $LiFThF_4PuF_3UF_4$ system,* Journal of Nuclear Materials **462**, 43 (2015).

[21] C. Bale, E. Bélisle, P. Chartrand, S. Decterov, G. Eriksson, A. Gheribi, K. Hack, I.-H. Jung, Y.-B. Kang, J. Melançon, A. Pelton, S. Petersen, C. Robelin, J. Sangster, P. Spencer, and M.-A. V. Ende], *FactSage thermochemical software and databases, 20102016,* Calphad **54**, 35 (2016).

3

THERMAL CONDUCTIVITY OF SOLID ALKALI FLUORIDES

> *Nothing in life has to be feared;*
> *it is only to be understood.*
> *Now is the time to understand more,*
> *so we may fear less.*
>
> Marie Curie

In this work, the thermal diffusivity of a series of fluoride salts including Molten Salt Reactor fuel salt mixtures has been studied in their solid state. The alkali halides as LiF, KF, NaF and their ternary mixture FLiNaK were measured. The thermal diffusivity of LiF, being the only fluoride salt measured in literature, was compared to these literature results. Thereafter, the thermal diffusivity of PuF_3 *and molten salt fuel mixtures* $LiF\text{-}ThF_4\text{-}UF_4$ *(77.5-20.0-2.5 mol %) and* $LiF\text{-}ThF_4\text{-}UF_4\text{-}PuF_3$ *(77.5-6.6-12.3-3.6 mol %) have been measured for the first time. The Laser Flash facility was used to measure the thermal diffusivity as a function of temperature in the range from 500 K to 100 K below the melting point of each sample analyzed. It was found that the thermal conductivity, calculated from the measured thermal diffusivity, is very small for the molten salt fuel mixtures in their solid state, i.e. between 0.4 and 3 W/mK, while it is higher for the alkali fluorides, being between 1 and 10 W/mK.*

3.1. INTRODUCTION

In a preliminary list of transients in the Molten Salt Reactors (MSR)[1] some scenarios include the over cooling of the reactor core that can result in the fuel salt solidification and the precipitation of some elements in the coldest regions of the fuel circuit, e.g. in the heat exchangers [2]. The over cooling scenario and the consequent formation of frozen salt is of safety concern because a solid crust can be formed at the walls of the piping and at the freeze plug. In case of an event that requires the drainage of the fuel salt from the core, the freeze plug, a valve made of frozen fuel salt, melts and the molten salt is drained by gravitation into a storage tank underneath the core [3]. In case of fuel solidification, the crust can clog up one of the emergency draining orifices or the draining shaft, thus hindering the emergency draining. For the prediction of the melting behaviour of the freeze plug it is important to know the fuel salt characteristics.

In the case of a formation of a solid crust, it is important to know the heat transfer through the solidified salt, to understand the thermodynamics of the solidification process and the influence it will have on surrounding materials. This work focuses on one of the key properties of the salt of importance for the heat transfer; being the thermal conductivity, which governs the ability of the salt to conduct heat. In this work, we investigated the thermal conductivity of molten salt fuel systems considering the possible precipitates upon cooling of Molten Salt Fast Reactor (MSFR) fuel salts. The two fuel systems taken in consideration for the analysis are the LiF-ThF_4-UF_4 and the LiF-ThF_4-UF_4-PuF_3, the two options currently considered in the SAMOFAR project for the MSFR. The reference initial composition of the MSFR fuel containing only uranium as fissile element is LiF-ThF_4-UF_4 (77.5-20.0-2.5 mol %), called Fuel 1. The salt composition of the MSFR fuel containing uranium and plutonium as fissile elements is LiF-ThF_4-UF_4-PuF_3 (77.5-6.6-12.3-3.6 mol %), called Fuel 2. Upon cooling of the MSFR fuel, solid fluoride salts can precipitate. Using the developed JRCMSD thermodynamic database, the crystallization paths have been examined. From the pseudobinary phase diagram of the LiF-ThF_4 system with a constant amount of UF_4 set to 2.5 mol % [4], following the Fuel 1 composition, the precipitates can be retrieved. The first precipitate upon cooling is LiF occurring at the liquidus line at 850 K. Cooling further, at 830 K $Li_3(Th,U)F_7$ precipitates and finally at 826 K the solidus line is reached with disappearance of the last liquid phase. In the case of the Fuel 2 composition, the first precipitate upon cooling is LiF crystallizing at 853 K, followed by formation of solid PuF_3 at 835 K and $Li_3(Th,U)F_7$ solid solution at 780 K to reach solidus line at 776 K. The precipitates were analysed from the pseudobinary phase diagram of the LiF-UF_4 system with constant amount of ThF_4 set to 6.6 mol % and PuF_3 set to 3.6 mol % [5].

This work aims at investigating the thermal conductivity of the precipitates from the Fuel 1 and Fuel 2 upon cooling. Other single fluoride salts, namely NaF, KF and FLiNaK, were measured to compare the thermal conductivity of alkali and actinide fluorides. The influence of the mass of the cation and the density of the salt mixture on the thermal diffusivity was investigated. Since the thermal conductivity before the melting point was measured by other authors only for LiF, this was the only salt that could be compared with the literature [6, 7].

The thermal conductivity was obtained by the product of the thermal diffusivity α, the specific heat C_p and the density ρ:

$$\kappa = \alpha \rho C_p \tag{3.1}$$

The thermal diffusivity was measured experimentally with the laser flash method, developed initially by Parker et al. [8]. The laser flash method consists of heating with a laser pulse with energy less than 0.5 J on one side of a sample with two parallel faces. The resulting time dependent temperature rise on the other side of the sample due to the laser pulse is measured. From the time dependent temperature rise the thermal diffusivity can be derived: the faster the temperature at the other side of the sample increases, the higher is the thermal diffusivity. The thermal diffusivity, α, can be calculated as:

$$\alpha = 0.1388 \frac{d^2}{t_{1/2}} \tag{3.2}$$

where d is the thickness of the sample and $t_{1/2}$ is the time to the half maximum of the temperature rise of the sample after the heating pulse by the laser. Equation 3.2 is valid in a one dimensional case and considering an adiabatic case. The model was improved from 1961 and a more sophisticated model takes in consideration the finite duration of the heat pulse, heat losses [9], effect of radiation and convection [10] and radial heat transfer [11]. These properties have been added to Equation 3.2 as shown in [11] by Blumm and Opfermann, who demonstrated the accuracy of his model fitting experimental data for the thermal diffusivity. The model shown in [11] was used at JRC-Karlsruhe by Sheindlin et al. [12] and Ronchi et al. [13]. Sheindlin and Ronchi further improved the laser flash method to measure irradiated nuclear fuels and non-irradiated samples at very high temperatures. The actinide and alkali fluorides and the mixtures of fuel salts, corrosive and melting at high temperatures (up to 1600 K for PuF_3), were measured with the laser flash method. Their thermal diffusivity was measured from 550 K up to close to the melting point.

The remainder of the chapter is organized as follows. In Section 2, the method employed for the analysis is described, together with a thorough explanation of the sample preparation. In Section 3, the experimental results are presented. Finally, in Section 4, we draw the conclusions.

3.2. EXPERIMENTAL

3.2.1. SAMPLE PREPARATION

The samples measured were both pure alkali or actinide fluorides and mixtures of them. The alkali fluorides used in the experiments were LiF, NaF, KF of 99.99 w% metallic purity purchased from Sigma Aldrich. The actinide fluorides ThF_4, UF_4 and PuF_3 were synthesised and purified to analytical grade [14, 15] at JRC-Karlsruhe. Since the fluorides are very hygroscopic, they were handled in argon glove boxes in which the concentration of oxygen and water were monitored. These were constantly below 1 ppm for oxygen, and 2 ppm for water. LiF, NaF, KF were preliminary purified in order to remove residual moisture from the single fluorides. The purification consisted of heating the salts for 4 hours at 400°C in inert argon atmosphere. Starting from single fluorides, samples of LiF-ThF_4, LiF-ThF_4-UF_4 and LiF-ThF_4-UF_4-PuF_3 were prepared. The preparation of the mixtures consisted in grinding the components, in a selected molar ratio, together in an agate mortar until the mixture was considered homogeneous, after at least 10 minutes of grinding. LiF-ThF_4 was mixed in the molar ratio 75:25, the basic eutectic mixture for MSFR. The LiF-ThF_4-UF_4 salt was mixed in the molar ratio 77.5:20:2.5, that is the reference initial composition of the MSFR fuel started with uranium-233 [16]. The LiF-ThF_4-UF_4-PuF_3 was mixed in the molar ratio 77.3:6.6:12.5:3.6, composition considered for the MSFR fuel mixture containing PuF_3 [17].

3.2.2. PELLET PREPARATION

For the measurement of the thermal diffusivity, thin disks of salt were prepared. Three methods were tested in this work to prepare the samples:

1. the salt was pressed into pellets, these salts will be referred to with the superscript 'pp'
2. the salt was pressed in pellets and sintered afterwards, these salts will be referred to with the superscript 's'
3. the salt was melted and cooled to form solid like-glass salt, these salts will be referred to with the superscript 'm'.

METHOD 1

For preparing the pressed pellets a die was used [18]. The powder was finely grained, poured in the bore of the cylinder body of the die and sandwiched between two polished metal cylinders. The die was pressed by a hydraulic, automatic pistol-cylinder press. Approximately four tons of force was applied for 5 minutes on the disks. In general all the pressed pellets looked cloudy after being pressed into pellets. In Figure 3.1, on the left side, a pellet of LiF is shown (LiF-1^{pp}), that looks white and cloudy. Ideally, a pressed pellet without defects should appear clear and transparent like glass. The alkali halide crystals are optically transparent in a wide spectral range [19]. In the case of alkali fluorides, the pellets were not transparent. LiF, KF, NaF are white as powder and being their bulk modulus high, respectively 70, 29 and 48 GPa [20, 21], it was difficult to obtain transparent pellets. The bulk modulus indicates how compressible a substance is and a high bulk modulus means that a high pressure is necessary to compress a substance. LiF, shown in Figure 3.1, remained cloudy and was friable. The bulk modulus or hardness of LiF substantially exceeds that of other samples [22], therefore producing homogeneous transparent pellets requires very high pressure. Regarding the other alkali fluorides analyzed, the pellets of KF were the only ones that looked less cloudy and more transparent after pressing, its bulk modulus is the lowest between all the other alkali fluorides. PuF_3 is light purple as powder and when pressed, it maintained the color and looked opaque, a first sign that a dense disk was not created. Its bulk modulus of 116 GPa [23] is the highest between all the salts that were pressed.

METHOD 2

Some of the pellets showed defects, inhomogeneities or cracks on the surface. Inhomogeneities in the pellets can influence the thermal diffusivity measurements modifying the path of the heat through the disk. A second method of preparation was used on these pellets, namely LiF-2^{s}, Na-F-2^{s} and KF-2^{s}. These pellets were sintered in the furnace at 600°C for eight hours after being pressed. During the sintering, supposedly the pellets expanded and shrank due to the thermal treatment [24]. After the sintering procedure the pellets that presented some small cracks on the surface looked more homogeneous at the eyes. The density of the LiF-2^{s} and KF-2^{s} also increased, as is reported in Table 3.1. The pellet Na-F-2^{s} did not show any change after the sintering process.

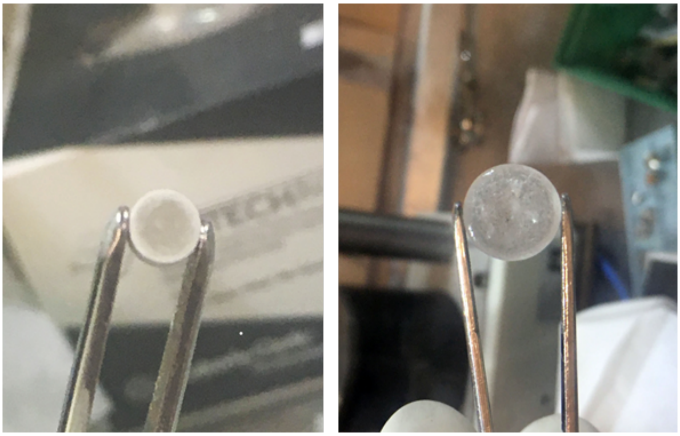

Figure 3.1: Photo of a pressed pellet of LiF, on the left side, and the re-solidified disk of LiF, on the right side.

METHOD 3

As a third and last method of preparation, the powder of salt was melted in a glassy carbon crucible, material that does not interact chemically with the molten salt and resists to its corrosion. The powder was heated up slowly in an inert atmosphere of argon to a temperature where it was completely molten. The liquid was allowed to solidify slowly, with a cooling rate of 4K/min, from the bottom of the container. This prevented the formation of voids in the solid sample. The crystallized salt was then polished to have disks with two parallel and flat surfaces required for the laser flash analysis.

A pressed pellet disk of LiF and the salt after melting and re-solidification are shown in Figure 3.1. The salt after re-solidification looks transparent to the eyes, indicating a high density of the salt itself. The pre-melted salt was also less fragile compared to the pressed pellet one.

SELECTION OF METHODS

The alkali fluorides (LiF, KF, NaF), FLiNaK and PuF_3 were analysed both as pressed pellets (pp) and as pre-molten salts (m). All the sintered pellets of LiF, NaF and KF broke during the measurement of the thermal diffusivity. Due to the scarcity of the actinide fluorides, it was decided to not create pressed pellets also for the fuel mixtures. The fuel mixtures were analysed only as pre-molten salts, therefore, a comparison between the thermal conductivity of the fuel mixtures as pressed pellets and pre-molten salts is not possible. The third method, based on melting and re-crystallization of the salt, was found the most reliable in producing solid disks of fluoride salts. While some of the pressed and sintered pellets were discarded because they presented cracks or broke during the laser flash measurements, the pre-molten disks of all the salts analyzed were measurable. Melting and producing solid-crystalline salt is also the method most representative for solid salt formation along cold walls in a MSR.

3.2.3. DENSITY MEASUREMENT

The measurement of the density is of high importance to have a value of the porosity of the pellets. The density was measured with the geometrical method (based on the mass and volume of the samples) on all the pellets that did not exhibit evident damage and had a very regular shape. Most of the molten and recrystallized salts, however, did not have a regular shape and their density was measured with the Archimedes method. The method relies on simply measuring the weight of an object in air and immersed in a fluid with known density.

The fluid used for this measurements was water.

This procedure was possible only for LiF, NaF, FLiNaK and for the LiF-ThF_4 mixture. The other salts have a high solubility in water [25, 26] and were dissolved before the measurement could be completed, thus, the procedure was not possible. For $PuF_3{}^m$, the density was retrieved from the XRD measurements using the following equation:

$$\rho = \frac{nM_w}{N_A V} \tag{3.3}$$

where n is the number of atoms per unit cell, M_w is the molecular weight, N_A is the Avogadro's number and V is the volume of the unit cell. The volume of the unit cell was determined by XRD analysis from the cell parameters [27]. The same calculation was done on the LiF, NaF, KF samples and is reported in Table 3.1. For the fuel mixtures, Fuel 1 and Fuel 2 , the density was calculated from the molar volume of the end members of the salt mixtures. The molar volume of the end member was calculated from their density ρ as

$$V_M = \frac{\rho}{M} \tag{3.4}$$

where M is the molar mass. For the Fuel 1 and Fuel 2 mixtures, the density of LiF, ThF_4, UF_4 and PuF_3 was taken from the literature, respectively from [23, 28–30]. It was assumed, based on previous studies of Beneš and Konings [31], that the densities of these mixtures followed ideal or close to ideal behaviour, i.e. that the density could be extrapolated by averaging the molar volumes of the corresponding end-members. In case of the Fuel 1 composition, the molar volume, V_M, of each mixture was therefore calculated as:

$$V_M(Fuel1) = 0.775 \cdot V_M(LiF) + 0.200 \cdot V_M(ThF_4) + 0.025 \cdot V_M(UF_4). \tag{3.5}$$

For the Fuel 2 composition, the molar volume was calculated according to:

$$V_m(Fuel2) = 0.775 \cdot V_M(LiF) + 0.066 \cdot V_M(ThF_4) + 0.123 \cdot V_M(UF_4) + 0.036 \cdot V_M(PuF_3). \tag{3.6}$$

Knowing the molar mass, M, of the Fuels 1 and 2, the density was then calculated as $\rho = V_M \cdot M$.

The measured density of the samples is reported in Table 3.1. For the four samples (LiF, NaF, FLiNaK and PuF_3) for which the measurement of the density was possible in the two forms of pressed pellets and pre-molten salts it was found that the density increases respectively for LiF, NaF, FLiNaK and PuF_3 of 17, 1, 6 and 23%. The larger increase of the density of pre-molten disks of PuF_3 and LiF compared with the other two salts is due to their higher bulk modulus [23, 32] and the higher difficulty in creating a dense pressed pellet.

Table 3.1: Properties of alkali fluorides pellets at 298K

Sample	mass mg	diameter mm	thickness mm	experimental density g / mL	volumetric density g / mL	literature value g / mL
LiF-1^{pp}	101.4	5.00	2.3	2.246^{G}	2.643	2.64 [28]
LiF-2^{pp}	96.8	5.00	2.1	2.349^{G}	2.643	2.64 [28]
LiF-2^{s}	96.6	5.00	2.0	2.461^{G}	2.643	2.64 [28]
LiF ^{m}	134.5	-*	1.9	2.638^{A}	2.643	2.64 [28]
LiF-2 ^{m}	224	-*	1.9	2.638^{A}	2.643	2.64 [28]
KF^{pp}	57.4	5.00	1.2	2.437^{G}	2.521	2.48[33]
KF-2^{pp}	127.5	5.00	2.8	2.320^{G}	2.521	2.48[33]
KF-2^{s}	127.1	5.00	2.6	2.491^{G}	2.521	2.48[33]
KF^{m}	91	-*	0.9	-	2.521	2.48[33]
NaF^{pp}	148	5.05	2.65	2.790^{G}	2.805	2.80[34]
NaF-2^{pp}	69.6	5.00	1.3	2.728^{G}	2.805	2.80[34]
NaF-2^{s}	69.6	5.00	1.3	2.728^{G}	2.805	2.80[34]
NaF^{m}	71.26	-*	1.2	2.814^{A}	2.805	2.80[34]
FLiNaK^{pp}	53.5	5	1.05	2.596^{G}	2.56^{C}	
FLiNaK^{m}	162.8	-*	1.0	2.744^{A}	2.560^{C}	
PuF$_3$^{pp}	194.7	5	1.4	7.086^{G}		9.34[23]
PuF$_3$^{m}	145.9	4.05	1.3	8716^{G}		9.34[23]
LiF-ThF$_4$^{m} (75-25)	161.9	-*	0.9	5.135^{A}	4.79^{C}	
Fuel-1^{m}	78.5	-*	1.35	-	4.957^{C}	
Fuel-2^{m}	101.4	-*	1.5	-	4.964^{C}	

[pp] These samples were pressed pellets of salt.

[s] These samples were sintered at 600°C for eight hours after being pressed.

[m] These samples were molten in a glassy carbon crucible.

[*] These samples had an irregular shape, therefore their density was not measured using the geometrical method and their diameter was not useful for the measurements.

[G] The density was measured geometrically by the weight and volume of the disk.

[A] The density was measured with the Archimedes method.

[C] The theoretical density of these mixtures of salt was calculated from the molar volume and molar mass of the mixture, approximating the molar volume of the mixture as the sum of the theoretical molar volume of its individual components.

3.2.4. LASER FLASH SET-UP

The thermal diffusivity measurements were carried out using the so-called LAF (LAser Flash) device, in Figure 3.2, designed and constructed at JRC-Karlsruhe [12]. In order to measure radioactive elements, the LAF facility is installed in a glove-box, which is surrounded by lead shielding and equipped with two manipulators. The measurements were conducted on small size disks with a diameter of ~ 5 mm. For the measurement of the thermal diffusivity it is necessary to know the sample thickness that was measured using an analogical caliper with a stem that rotates as it touches the sample. The thickness of the disks, from 1 to 2 mm, was measured at the centre of the disks and on the sides and it was the same for each pellet with an accuracy of 2.5 %. Each sample was checked to ensure that it did not have defects and that it had the two faces plane and parallel. Due to the transparency of all these samples to the laser pulse, a coating was applied to all samples by spraying a thin layer of graphite on both surfaces. A graphite coating reduces radiative transfer and serves as a black block to the laser light. The graphite is used to increase absorption of the laser pulse as well as sample emissions.

The specimen was mounted on a sapphire disk, which is transparent to the Nd-YAG pulse laser beam and can be easily replaced in case of corrosion or damage. The specimen was located at mid-height of a graphite tube and heated by a high frequency (HF) induction coil. The graphite tube could be raised and lowered by remote manipulators to allow the mounting of specimens. The tube was then positioned in the middle of a HF furnace surrounded by thermal shields. The selection of the optimum measurement point on the sample surface was performed looking at the surface of the sample with a microscope pointed on the sample. The temperature range for the sample studied in this work was from 500 to about 1500 K depending on the melting temperature of the sample analysed. The maximum temperature was set to be at least 100 K below the melting point in order to avoid sample decomposition.

The HF vessel was pumped down with turbomolecular pumps, its atmosphere could be regulated with a gas-inlet system up to vacuum conditions between 10^{-4} to 10^{-7}mbar.Then the vessel was filled with a static atmosphere of 10^{-3} mbar of nitrogen initially containing 0.1% of oxygen. This atmosphere is used to avoid the hydration of fluoride salts.

After stabilisation of the sample temperature (between 0.5 and 1 h in the lower temperature range) a focused laser pulse was shot on the lower face of the sample via an optical fibre. The laser spot was ~ 5 mm in diameter, the pulse duration was between 2 and 10 ms, depending on the thickness of the sample (for thicker samples a longer laser pulse was sent). To limit the temperature rise between the two faces of the sample, less than 1 J in energy was selected for each pulse. The thermal diffusivity was measured approximately each 100 K. For each temperature the laser pulse was shot three times to get three recordings per temperature.

The temperature variation on the upper side of each sample was recorded through an optical fibre by an InGaAs photodiode detector. The detector was calibrated with a thermocouple mounted in the center of a standard sample . After amplification, the detected signal was then digitalized and transmitted to a computer for data analysis.

The measured temperature transient was plotted as a function of the time for extracting the thermal diffusivity. The thermogram was fitted with Ronchi's code [13] that takes into consideration the radiation heat losses from both the disk surfaces, and also the radial heat losses. The measured thermograms were carefully inspected to ensure that heat transfer conditions were standard, as described in [12, 13]. From the thermogram, the Ronchi's code computes the thermal diffusivity at each temperature based on an analytical solution taking into account heat losses. The standard deviation, calculated from the fitting of the thermograms, of each thermal diffusivity measurements was always lower than 2%.

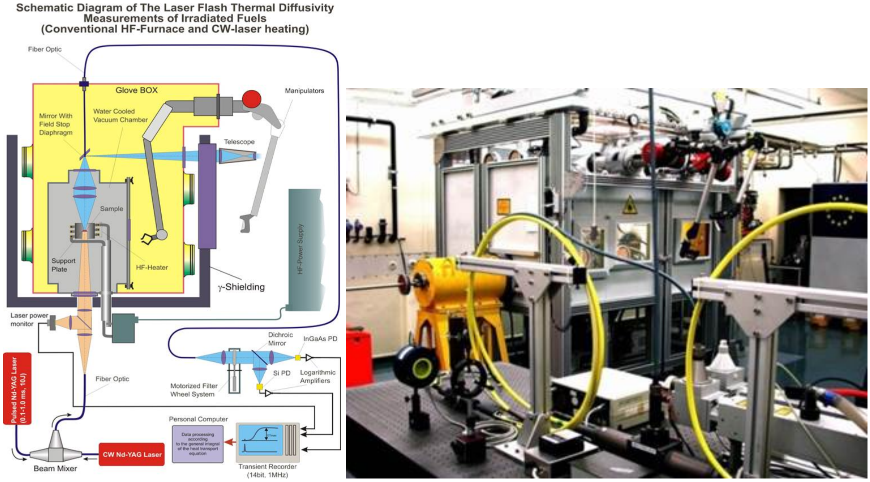

(a) Schematic setup

(b) Photo of LAF

Figure 3.2: Schematic laser flash setup for the thermal diffusivity measurement in the temperature range 500-1600 K

3.2.5. X-RAY COMPUTED TOMOGRAPHY

When pressing the powder in compact pellets, as for the sample indicated as pp in Table 3.1, it is possible that cracks on the surface or in the bulk of the pellets are formed. The pressed pellets might also be inhomogeneous in density and the measured thermal diffusivity might, therefore, be influenced by the density gradients. The presence of cracks and density gradients in the pressed pellets was seen using X-ray Computed Tomography (CT), which is a nondestructive measurement technique that allows to see images of the pellets [35]. The X-ray computed tomography was performed on samples placed on a vertical rotary stage located between a micro focus X-ray source and a digital flat panel detector (225 kV Nikon XTH 225 ST system).

3.2.6. XRD ANALYSIS

The one component fluoride samples (e.g. LiF, NaF, KF, PuF_3) were analysed before and after the laser-flash measurement by X-ray diffraction (XRD). This technique was used to check the purity of these samples before the LAF experiments, to calculate the density of samples as explained in Section 3.2.3 and to determine the possible formation of oxides during the LAF experiments. In these measurements the pellets were heated up to 100°C below the melting point in a vessel under vacuum. Even if oxidation was mostly improbable, the XRD patterns were checked since the oxidation could have been of influence on the thermal diffusivity.

The disks were broken and powdered by grinding in an agate mortar. The powder was homogenised and mixed with an epoxy resin. Approximately 20 mg of powder was embedded into the resin both to avoid dispersion of radioactive material in the glove box and to prevent further oxidation of the compounds in the nitrogen atmosphere of the glove box where the X-ray diffractometer is placed. The XRD measurements were carried out using a Bruker D8 Advance diffractometer mounted in a BraggBrentano configuration with a Cu K-alpha monochromator. The diffractometer was equipped with a LynxEye Linear Position Sensitive detector. The operation conditions were set at 40 kV and 40 mA. Powder diffraction patterns were recorded at room temperature across by step scanning in the angle range $10° \leq 2\theta \leq 120°$over a period of about 8 hours. Structural analysis was performed with the Fullprof2k suite software [36] by the Le Bail method.

3.3. RESULTS AND DISCUSSION

The thermal diffusivity of the alkali fluorides obtained in the frame of this work with our laser-flash facilities in the temperature range 500 K to 1100 K are plotted in Figure 3.5 and provided in Tables 3.3 and 3.4 (Appendix A). The results are compared for the alkali fluorides in form of pressed pellets and in form of pre-molten salts. Regarding the actinide fluorides, a comparison between the pressed pellet and the pre-molten disk was possible for PuF_3 only. The thermal diffusivity of PuF_3 and of the MSFR salt mixtures is plotted in the range 500 K to 1500 K in Figure 3.8 and provided in Tables 3.5 and 3.6. These results will be discussed in the subsequent sections in more detail.

3.3.1. THERMAL DIFFUSIVITY OF ALKALI HALIDES

The LiF salt was measured in the 500 to 1100 K range twice as pressed pellet and twice as pre-molten salt. This salt is the only one for which data on the thermal diffusivity, at temperatures below the melting point, are available to compare our results with the literature. Figure 3.3 shows the thermal diffusivity of LiF (both as pressed pellet and as pre-molten salt) together with the measured thermal diffusivity from Chang [7] and Yu and Hofmeister [6]. In these last two works, the authors measured melted and re-solidified samples and our values are well in agreement with the literature.

The thermal diffusivity varies slightly among the two LiF samples in the form of pressed pellets: with the biggest difference being 0.5 mm^2/s. The change in the thermal diffusivity among samples with the same chemical composition is tied to the densification of the pellets. However, the pellets did not present cracks or local variation in density as shown in Figure 3.4. The observed spread in thermal diffusivity decreases as temperature increases. The pellets become in-fact more compact at higher temperatures. At the maximum temperature the thermal diffusivity curve coalesces. This hypothesis is confirmed by the fact that the thermal diffusivity for the pre-molten LiF shows agreement between the two samples measured.

The thermal diffusivity in the 500 to 1100 K range obtained for various alkali fluorides in the form of pressed pellets and pre-molten salts is plotted in Figure 3.5. For each sample, the thermal diffusivity is highest at low temperature (T_{min}) and lowest at the

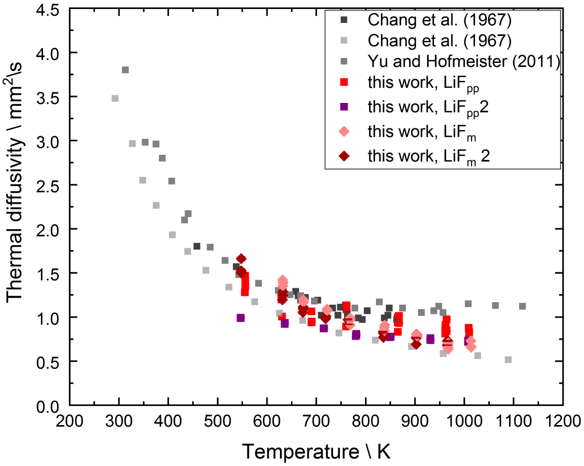

Figure 3.3: Thermal diffusivity of LiF as pressed pellets (LiF-1 and LiF-2) and as premolten salt (LiF-3 and LiF-4). The results are compared to the thermal diffusivity from Chang [7] and Yu and Hofmeister [6].

Figure 3.4: 2D computed Tomography on the pressed pellets of, from left to right, KF, LiF, NaF, PuF_3. The pellets have different colors because the attenuation of the X-rays, used to reconstruct these images, accounts for the number of atoms in the volume of material. Therefore PuF_3 is the darkest pellet because Pu has the highest atomic mass of all samples.

maximum run temperature (T_{max}), before the melting temperature of the alkali fluoride. The values for the thermal diffusivity range between 1.6 and 0.4 mm^2/s for the alkali fluorides in the form of pressed pellets in Figure 3.5a, while the alkali fluorides measured as pre-molten salts, in Figure 3.5b, have thermal diffusivity between 2.2 and 0.7 mm^2/s. The thermal diffusivity differs approximately 1 mm^2/s between samples with the same chemical composition but in a different physical state (as pressed salt or as pre-molten salt). The values are lower for the salts as pressed pellets respect to the pre-molten ones. The reason for this is in the higher density of the salts in their pre-molten state. The salts as pressed pellets have a higher porosity (i.e. lower density) and, therefore, might give a too low value of the thermal diffusivity.

The trend of the thermal diffusivity curves with the increase of temperature of the salts as pressed pellets and pre-molten salts is also different. The thermal diffusivity of pressed pellets decreases linearly with the increase of the temperature while this is not the case for the pre-molten salts. For the last ones, the derivative $\frac{d\alpha}{dT}$ is highest initially and decreases as temperature increases. At the lowest temperature, the standard deviations among the samples with the same chemical composition are below 2% for the pre-molten salts and below 4% for the pressed pellets. At the highest temperature, the thermal diffusivity has a standard deviation below 6 % for both pressed pellets and pre-molten salts. Among the pressed pellets of alkali fluorides, LiF has the highest α, followed by FLiNaK, KF and NaF. Concerning the pre-molten salts, this behaviour is different: NaF has the highest α , followed by FLiNaK, LiF and KF.

3.3.2. THERMAL CONDUCTIVITY OF ALKALI HALIDES

The thermal conductivity in Figure 3.6 was extracted via Equation 3.1 using the density, ρ, listed in Table 3.1 and the heat capacity, C_{p}, taken from Capelli et al. [37] and shown in Table 3.2. The C_{p} for the mixtures of salts used in this study was recalculated as the sum of the C_{p} for each component weighted for their molar fraction as:

$$C_p(mixture) = x(i) \cdot C_p(i) + x(j) \cdot C_p(j) + x(k) \cdot C_p(k) \tag{3.7}$$

where $C_p(mixture)$ is the heat capacity of the mixture of salts, $C_p(i)$ is the heat capacity of the single component and $x(i)$ is the molar fraction of the component. The density used for the calculation of the thermal conductivity was the experimental density from the geometrical or Archimedes measurement. For the salts for which this value was not available, the density from the literature was taken.

The thermal conductivity of the liquid alkali fluorides, LiF, Na, KF and FLiNaK was already measured by Smirnov et al. [38] as a function of temperature. They measured the thermal conductivity with the method of coaxial cylinders presenting results for the single alkali fluorides and their mixtures after their melting point in their liquid state. For the liquid salts, the thermal conductivity at the same temperature decreased in the series from lithium to sodium and potassium. They found that the thermal conductivity of molten alkali halides varies inversely related to their molar volume. Ohtori et al. [39] carried out Molecular Dynamics calculations for retrieving the thermal conductivity for alkali halides and found the same trend. The values reported by these authors are shown in Figure 3.7 together with our data on solid alkali fluorides. In this way, we obtain a complete picture of the thermal conductivity for a wide range of temperatures. In

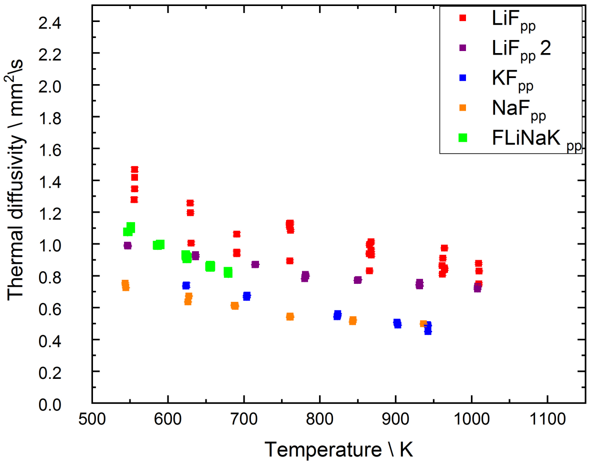

(a) Pressed pellets

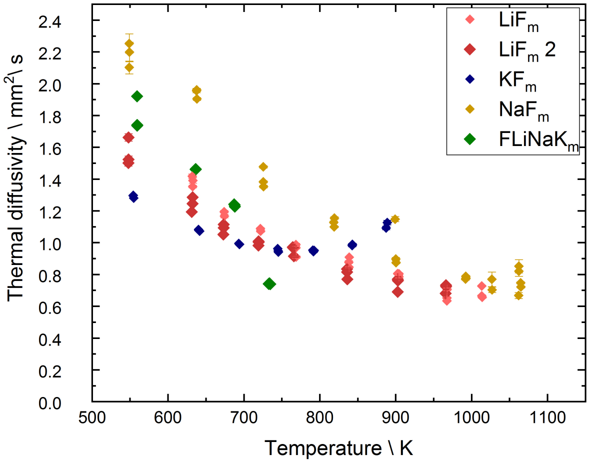

(b) Premolten salt

Figure 3.5: Thermal diffusivity of the alkali fluorides (LiF, NaF, KF, FLiNaK) as pressed pellets (a) and as premolten and resolidified salt (b).

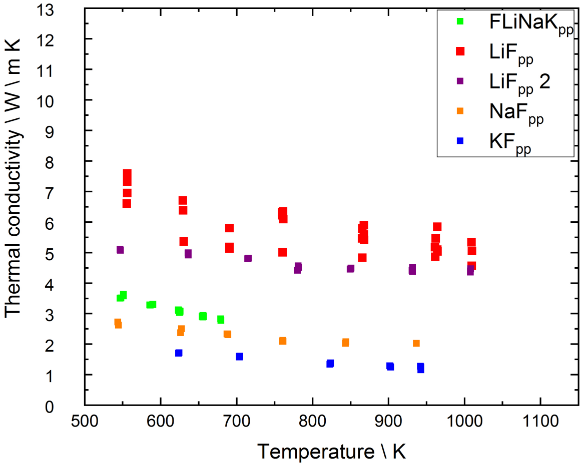

(a) Pressed pellets

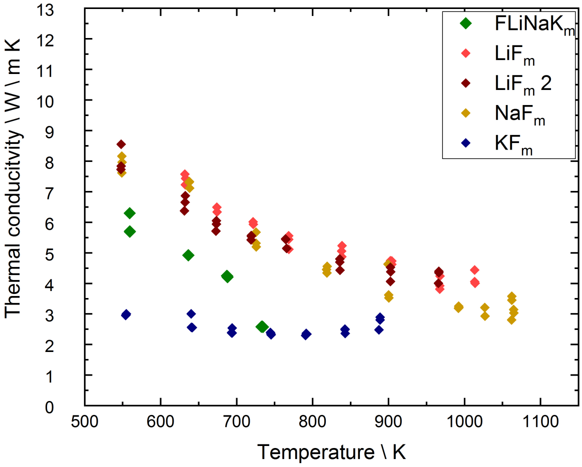

(b) Premolten salt

Figure 3.6: Thermal conductivity of the alkali fluorides (LiF, NaF, KF, FLiNaK) as pressed pellets (a) and as premolten and resolidified salt (b).

Table 3.2: C_p data of the compounds used in this study. C_p= heat capacity (J / kg K) [37].

Compound	composition	C_p= a + b T +c T^2 +d T^{-2}+ e T^3				
		a	b T	c T^2	d T^{-2}	eT^3
LiF(s)		43.309	$1.631 \cdot 10^{-2}$	$5.047 \cdot 10^{-7}$	-569,124	
NaF(s)		47.630	$1.479 \cdot 10^{-2}$		-464,300	
KF(s)		68.757	$-5.776 \cdot 10^{-2}$	$7.541 \cdot 10^{-5}$	-766,718	$-2.389 \cdot 10^{-8}$
FLiNaK(s)	46.5-11.5-42	54.494	$-1.497 \cdot 10^{-2}$	$3.191 \cdot 10^{-5}$	-640,059	$-1.003 \cdot 10^{-8}$
ThF_4(s)		122.173	$8.370 \cdot 10^{-3}$		-1,255,000	
UF_4(s)		114.519	$2.056 \cdot 10^{-2}$		-413,159	
LiF-ThF_4(s)	74.99-25.01	63.033	$1.433 \cdot 10^{-2}$	$3.785 \cdot 10^{-7}$	-740,662	
Fuel-1(s)	77.5-20-2.5	60.862	$1.483 \cdot 10^{-2}$	$3.911 \cdot 10^{-7}$	-702400	
PuF_3(s)		104.078	$7.070 \cdot 10^{-4}$		-1,035,500	
Fuel-2(s)	77.3-6.6-12.5-3.6	59.603	$1.576 \cdot 10^{-2}$	$3.901 \cdot 10^{-7}$	-611,686	

our work, for the solid salt we observe that the thermal conductivity diminishes with the increase of the temperature. On the other side, the thermal conductivity of NaF_m measured in this work is higher than expected if we consider that the thermal conductivity should decrease for the alkali fluorides with the increase of the atomic number of the alkali metal.

3.3.3. THERMAL DIFFUSIVITY AND CONDUCTIVITY OF PuF_3

The thermal diffusivity of PuF_3 was measured between 500 and 1400 K on both the salt as a pressed pellet and as pre-molten salts. Figure 3.8a shows the measured thermal diffusivity. Also for PuF_3 as for the alkali fluorides, the thermal diffusivity of the sample in the form of pressed pellet is lower than the sample in the form of pre-molten disk. Due to the high theoretical density and the high bulk modulus of PuF_3, it was difficult to make a dense pressed pellet and this caused the thermal diffusivity to be significantly lower than the pre-molten one. The measured density of ${PuF_3}^{pp}$ was 75 % of the theoretical one, while the one of ${PuF_3}^{m}$ was 93 %, confirming that the pre-molten disk was very dense and that the thermal diffusivity measured for this sample is more reliable. With values of thermal diffusivity below 0.7 mm^2/s, compared to the values of alkali fluorides between 2 and 0.8 mm^2/s at the lowest temperature, PuF_3 has a much smaller thermal diffusivity than alkali fluorides. The thermal diffusivity of PuF_3 diminishes of 40 % from 500 K to 1400 K. The thermal conductivity, calculated from the heat capacity of literature [4] and the experimental density, is show in Figure 3.8b.

3.3.4. THERMAL DIFFUSIVITY AND CONDUCTIVITY OF MOLTEN SALT REACTOR FUEL MIXTURES

The thermal diffusivity of the three salt mixtures of LiF-ThF_4 and MSFR-1 and MSFR-1 from 500 K to a temperature of 100 K below their melting point is plotted in Figure 3.8. With values of thermal diffusivity below 0.7 mm^2/s, compared to the values of alkali

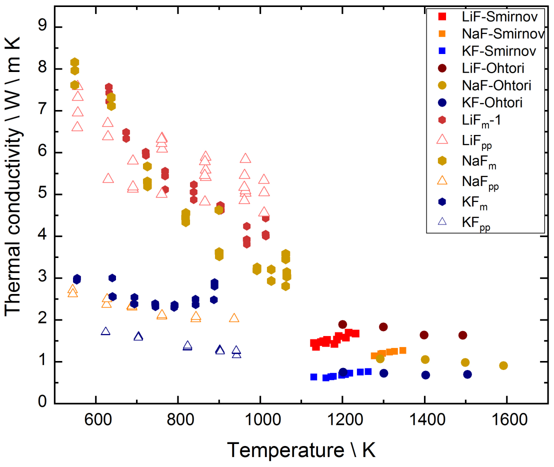

Figure 3.7: Thermal conductivity of LiF, NaF, KF measured in this work as pressed pellet and re-crystalized salt compared to the results obtained by Smirnov et al. [38] and Ohtori et al. [39] on the liquid salt.

fluorides between 2 and 0.8 mm^2/s at the lowest temperature, the actinide fluorides have a much smaller thermal diffusivity than alkali fluorides. The thermal diffusivity of the molten salt mixtures remains roughly constant with temperature, while for the studied alkali fluorides the thermal conductivity diminishes with temperature. It is also noticed that the thermal diffusivity diminishes with increasing number of components in the molten salt. It is high, ca. 0.7 mm^2/s, for PuF_3 and it decreases in the following order for LiF-ThF_4, LiF-ThF_4-UF_4, LiF-ThF_4-UF_4-PuF_3.

The thermal conductivity in Figure 3.9 was extracted via Equation 3.1 using the density, ρ, listed in Table 3.1 and the heat capacity, C_p, taken from Capelli et al.[37] and shown in Table 3.2.

3.4. CONCLUSIONS

The thermal diffusivity and conductivity of molten salt fuel is of particular interest for evaluating their capabilities as coolants and fuel in Molten Salt Fast Reactor (MSFR). these quantities are of importance in studying the heat transfer through frozen salt layers, directly linked to the thermal conductivity, at nominal and accident conditions. No reliable experimental values on the solid salts thermal conductivity are available in the literature.

In this work we measured the thermal diffusivity of a series of solid alkali fluorides (LiF, NaF, and KF), including the ternary mixture FLiNaK, of PuF_3 and of solid MSFR fuel mixtures (LiF-ThF_4, LiF-ThF_4-UF_4, LiF-ThF_4-UF_4-PuF_3). The thermal diffusivity has been measured in the temperature range from 500 K to 100 K below the melting point of each sample. In this range of temperature the measurement of the thermal diffusivity of

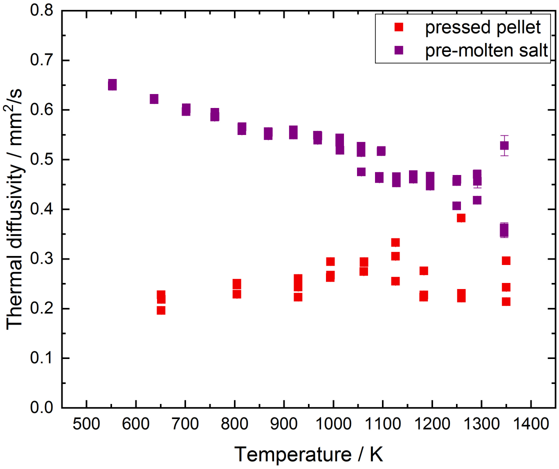

(a) Thermal diffusivity.

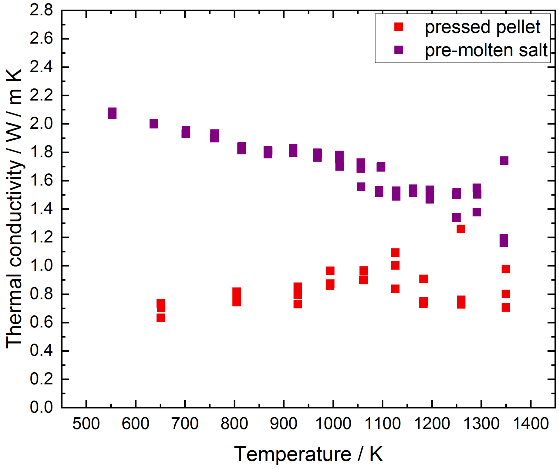

(b) Thermal conductivity.

Figure 3.8: Thermal diffusivity (a) and conductivity (b) of PuF_3. The PuF_3 was measured as pressed pellet and as premolten salt.

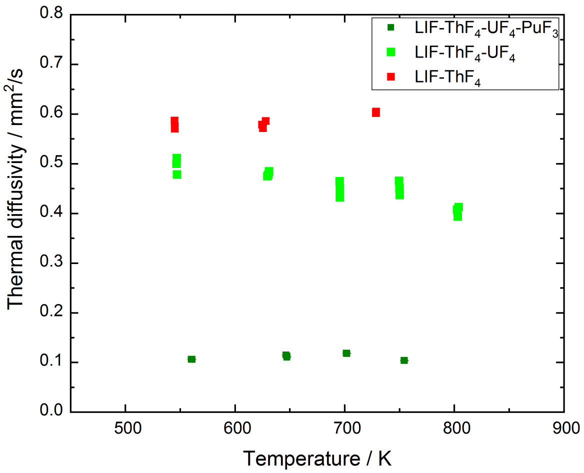

(a) Thermal diffusivity.

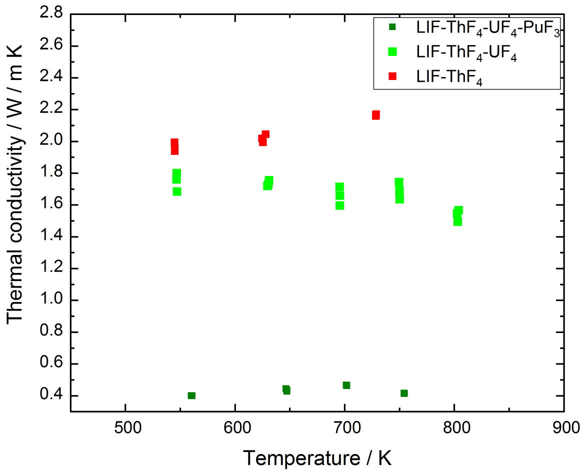

(b) Thermal conductivity.

Figure 3.9: Thermal diffusivity (a) and conductivity (b) of the Molten Salt Reactor fuel mixtures. The samples were measured as premolten salts.

MSFR fuel compositions is new. Alkali fluorides and PuF_3 have been measured in form of both pressed pellets and pre-molten disks showing that the salts in the pressed pellet form have lower thermal diffusivity than the salts as pre-molten salts. The difference was quite substantial for PuF_3 that has the highest theoretical density and bulk modulus. It was therefore difficult to produce a dense pellet by pressing. Alkali fluorides systematically have larger thermal conductivity than the molten salt mixtures. We also observed that the thermal conductivity is smaller for salt having more constituents. The only results present in literature for solid fluoride salts, between the ones considered here, were for LiF. The thermal diffusivity measured in this work for LiF showed good agreement with the literature values. These experiments are a preliminary work that can serve as a basis for further research on both the thermal conductivity of solid and liquid salt. We have determined the range of the thermal conductivity of alkali and actinide fluorides used in MSFR. We have also established a innovative method for measuring the thermal diffusivity of solid salts based on pre-melting the salt and analysing the formed crystal after re-solidification.

3.5. APPENDIX A

The measured thermal diffusivity for each compound studied in this work is reported in Table 3.3, 3.4, 3.5, 3.6. The standard deviation for the thermal diffusivity calculated from the fitting of the thermograms was always better than 2%.

REFERENCES

[1] R. Yoshioka, K. Furukawa, Y. Kato, and K. Mitachi, *Molten-Salt Reactor FUJI and Related Thorium Cycles,* in *Thorium Energy Alliance Spring Conference 2010* (Mountain View, 2010).

[2] B. M. Elsheikh, *Safety assessment of molten salt reactors in comparison with light water reactors,* Journal of radiation research and applied science **6**, 63 (2013).

[3] M. Tiberga, D. Shafer, D. Lathouwers, M. Rohde, and J. L. Kloosterman, *Preliminary investigation on the melting behavior of a freeze-valve for the Molten Salt Fast Reactor,* Annals of Nuclear Energy **132**, 544 (2019).

[4] E. Capelli, O. Beneš, M. Beilmann, and R. J. M. Konings, *Thermodynamic investigation of the LiF-ThF_4 system,* Journal of Chemical Thermodynamics **58**, 110 (2013).

[5] E. Capelli, O. Beneš, and R. J. M. Konings, *Thermodynamic assessment of the LiF$ThF_4PuF_3UF_4$ system,* **462**, 43 (2015).

[6] X. Yu and A. M. Hofmeister, *Thermal diffusivity of alkali and silver halide crystals as a function of temperature,* Journal of Applied Physics **109**, 033516 (2011).

[7] H. Chang, M. Altman, and R. Sharma, *The Determination of Thermal Diffusivities of Thermal Energy Storage Materials,* Transaction of ASME, Journal of Engineering for Power , 407 (1967).

[8] W. J. Parker, R. J. Jenkins, C. P. Butler, and G. L. Abbott, *Flash Method of Determining Thermal Diffusivity, Heat Capacity, and Thermal Conductivity,* Journal of Applied Physics **32**, 1679 (1961).

[9] J. A. Cape and G. W. Lehman, *Temperature and finite pulsetime effects in the flash method for measuring thermal diffusivity,* Journal of Applied Physics **34**, 1909 (1963), https://doi.org/10.1063/1.1729711 .

[10] R. D. Cowan, *Pulse method of measuring thermal diffusivity at high temperatures,* Journal of Applied Physics **34**, 926 (1963), https://doi.org/10.1063/1.1729564 .

[11] J. Blumm and J. Opfermann, *Improvement of the mathematical modeling of flash measurements,* High Temperatures- High Pressures **34**, 515 (2002).

[12] M. Sheindlin, D. Halton, M. Musella, and C. Ronchi, *Advances in the use of laser-flash techniques for thermal diffusivity measurement,* **69**, 1426 (1998).

[13] C. Ronchi, M. Sheindlin, M. Musella, and G. J. Hyland, *Thermal conductivity of uranium dioxide up to 2900 K from simultaneous measurement of the heat capacity and thermal diffusivity,* Journal of Applied Physics **85**, 776 (1999).

[14] P. Souček, O. Beneš, B. Claux, E. Capelli, M. Ougier, V. Tyrpekl, J. F. Vigier, and R. J. M. Konings, *Synthesis of UF_4 and ThF_4 by HF gas fluorination and re-determination of the UF_4 melting point,* Journal of Fluorine Chemistry **200**, 33 (2017).

[15] A. Tosolin, P. Souček, O. Beneš, J. F. Vigier, L. Luzzi, and R. J. M. Konings, *Synthesis of plutonium trifluoride by hydro-fluorination and novel thermodynamic data for the $PuF_3 - LiF$ system,* Journal of Nuclear Materials **503**, 171 (2018).

[16] E. Merle-Lucotte, D. Heuer, M. Allibert, M. Brovchenko, N. Capellan, and V. Ghetta, *Launching the Thorium Fuel Cycle with the Molten Salt Fast Reactor,* in *Proceedings of ICAPP 2011* (Nice, France, 2011) pp. 842–851.

[17] E. Merle-Lucotte, D. Heuer, M. Allibert, X. Doligez, and V. Ghetta, *Optimizing the burning efficiency and the deployment capacities of the molten salt fast reactor,* in *Proceedings of Global 2009* (Paris, France, 2009) pp. 1864–1872.

[18] J. M. Chalmers, *Infrared spectroscopy | sample presentation,* in *Reference Module in Chemistry, Molecular Sciences and Chemical Engineering* (Elsevier, 2013).

[19] S. L. Baldochi and I. M. Ranieri, *Alkali halide crystals growth,* in *Reference Module in Materials Science and Materials Engineering* (Elsevier, 2016).

[20] R. Srinivasa and S. Sanyal, *Structural and elastic properties of sodium halides at high pressure,* Physical Review, Serie 3. B - Condensed Matter (18,1978-) **42**, 1810 (1990).

[21] E. Broch, I. Oftedal, and A. Pabst, *Neubestimmung der gitterkonstanten von kf, cscl und baf2,* Zeitschrift fuer Physikalische Chemie, Abteilung B: Chemie der Elementarprozesse, Aufbau der Materie **3**, 209 (1929).

[22] Y. Sumino and O. L. Anderson, *Handbook of Physical Properties of Rocks*, edited by R. S. Carmichael, Vol. 2 (CRC Press, Boca Raton, Florida, 1982) p. 49.

[23] W. Zachariasen, *X-ray diffraction studies of fluorides of plutonium and neptunium, chemical identity and crystal structure,* Nat. Nucl. Energy Ser. Div. Iv. Sec. B **14**, 1462 (1949).

[24] M. R. Harvey, A. R. Teter, and R. L. Leggett, *Fabrication of oxide nuclear fuel pellets,* in *RFP-1255 UC-25 Metals, ceramics, and materials TID-4500* (U.S. Atomic energy commission, 1969).

[25] J. Faridi and M. E. Guendouzi, *Solubility of potassium fluoride in aqueous solution at different temperatures 298.15 K 353.15 K,* MATEC Web of Conferences **5**, 4 (2013).

[26] J. G. Reynolds and J. D. Belsher, *A Review of Sodium Fluoride Solubility in Water,* Journal of Chemical and Engineering Data **62**, 1743 (2017).

[27] W. G. Schlecht, *Calculation of density from x-ray data*,* American Mineralogist **29**, 108 (1944), https://pubs.geoscienceworld.org/ammin/article-pdf/29/3-4/108/4243350/am-1944-108.pdf .

[28] S.-A. M. KGaA., *Lithium fluoride - Product Specification Sheet,* ().

[29] G. Benner and B. Mueller, *Zur kenntnis binaerer fluoride des zr f4-typs: Hf f4 und th f4,* Zeitschrift fuer Anorganische und Allgemeine Chemie (1950) (DE) **588**, 33 (1990).

[30] S. Kern, J. Hayward, S. Roberts, J. Richardson, F. Rotella, L. Soderholm, B. Cort, M. Tinkle, M. West, D. Hoisington, and G. Lander, *Temperature variation of the structural parameters in actinide tetrafluorides,* Journal of Chemical Physics **101**, 9333 (1994).

[31] O. Beneš and R. Konings, *Thermodynamic properties and phase diagrams of fluoride salts for nuclear applications,* Journal of Fluorine Chemistry **130**, 22 (2009), fluorine & Nuclear Energy.

[32] S. Z. Hong, D. Jun, and X. Y. Wen, *First-principles calculations of the structural, electronic and optical properties of lif up to 300 gpa,* Physica B, Condensed Matter **406**, 3660 (2011).

[33] S.-A. M. KGaA., *Potassium fluoride - Product Specification Sheet,* ().

[34] S.-A. M. KGaA., *Sodium fluoride - Product Specification Sheet,* ().

[35] D. Phillips and J. Lannutti, *Measuring physical density with x-ray computed tomography,* NDT & E International **30**, 339 (1997).

[36] J. Rodríguez-Carvajal, *Recent advances in magnetic structure determination by neutron powder diffraction,* Physica B: Physics of Condensed Matter **192**, 55 (1993).

[37] E. Capelli, O. Beneš, and R. J. Konings, *Thermodynamic assessment of the LiF-NaF-BeF2-ThF 4-UF4 system,* Journal of Nuclear Materials **449**, 111 (2014).

[38] M. V. Smirnov, V. A. Khokhlov, and E. S. Filatov, *Thermal conductivity of molten alkali halides and their mixtures,* Electrochimica Acta **32**, 1019 (1986).

[39] N. Ohtori, T. Oono, and K. Takase, *Thermal conductivity of molten alkali halides: Temperature and density dependence,* Journal of Chemical Physics **130**, 1 (2009).

Table 3.3: Thermal diffusivity of pressed pellets of alkali halides measured with the LAF set-up. T = temperature (K), $\alpha = 10^{-6}$ (m^2/s)

FLiNaK pp		LiF pp		LiF pp 2		NaF pp		KF pp	
T	α	T	α	T	α	T	α	T	α
546	1.0751	761	1.1313	547	0.9863	544	0.7530	624	0.7348
548	1.0757	762	1.0858	547	0.9874	544	0.7248	624	0.7411
586	0.9920	868	1.0129	547	0.9919	626	0.6361	704	0.6781
586	0.9894	867	0.9302	636	0.9192	627	0.6722	704	0.6745
624	0.9216	868	0.9732	636	0.9310	687	0.6144	704	0.6639
624	0.9243	964	0.8389	636	0.9331	688	0.6072	823	0.5417
623	0.9327	965	0.8486	715	0.8691	688	0.6147	823	0.5498
656	0.8666	964	0.8773	715	0.8709	761	0.5395	824	0.5617
657	0.8590	1009	0.8289	716	0.8723	761	0.5388	902	0.5085
656	0.8624	1010	0.7492	780	0.7818	761	0.5463	902	0.5026
679	0.8277	1010	0.8629	781	0.8077	843	0.5106	903	0.4903
679	0.8136	961	0.8096	782	0.7982	844	0.5232	943	0.4493
679	0.8138	962	0.9102	849	0.7706	937	0.4978	943	0.4866
655	0.8572	962	0.8302	850	0.7716			942	0.4929
656	0.8527	866	0.9956	851	0.7763				
656	0.8549	865	0.9390	931	0.7432				
626	0.9174	865	0.8930	932	0.7356				
626	0.9092	761	1.1097	932	0.7585				
625	0.9059	760	1.1279	1008	0.7164				
590	0.9944	760	1.0615	1008	0.7227				
590	0.9936	691	0.9386	1008	0.7347				
590	0.9990	691	0.9487	1076	0.9463				
551	1.1005	691	1.0046	1077	0.9648				
551	1.0948	630	1.1964						
551	1.1100	630	1.2565						
		629	1.2782						
		555	1.4682						
		556	1.3454						
		556	1.4176						

Table 3.4: Thermal diffusivity of pre-molten pellets of alkali halides measured with the LAF set-up. T = temperature (K), α = 10^{-6} (m^2/s)

FLiNaK m		LiF m		LiF m 2		NaF m		KFm	
T	α	T	α	T	α	T	α	T	α
559	1.9210	632	1.4179	548	1.5011	549	2.1026	554	1.2966
559	1.7404	633	1.3533	548	1.6615	549	2.1994	555	1.2806
559	1.7369	633	1.3915	548	1.5233	549	2.2531	554	1.2983
636	1.4618	674	1.1673	631	1.1942	638	1.9562	640	1.0828
636	1.4629	674	1.1949	632	1.2455	638	1.9611	641	1.0783
636	1.4611	722	1.0878	632	1.2864	638	1.9044	642	1.0725
687	1.2413	722	1.0735	673	1.0521	726	1.3526	694	0.9889
688	1.2374	769	0.9096	673	1.1143	726	1.4768	694	0.9913
688	1.2275	769	0.9676	673	1.0936	726	1.3832	693	0.9946
733	0.7417	769	0.9882	719	0.9823	818	1.1283	745	0.9620
734	0.7441	838	0.8782	719	1.0079	819	1.1000	745	0.9484
735	0.7394	839	0.8462	719	1.0032	819	1.1548	745	0.9408
		839	0.9085	764	0.9719	900	0.8740	791	0.9531
		903	0.8058	765	0.9683	900	0.8976	792	0.9443
		904	0.8040	766	0.9157	899	1.1482	793	0.9511
		904	0.7853	836	0.8158	992	0.7720	843	0.9888
		968	0.6343	836	0.8339	992	0.7882	843	0.9850
		967	0.6528	836	0.7702	993	0.7769	843	0.9827
		968	0.7061	903	0.7611	1065	0.7474	887	1.0925
		1013	0.6651	903	0.6905	1065	0.7212	889	1.1266
		1014	0.7280	903	0.7695	1027	0.7039	889	1.1266
		1014	0.6567	966	0.6810	1027	0.7697		
				966	0.7243	1062	0.6680		
				966	0.7320	1062	0.8515		
						1062	0.8212		

Table 3.5: Thermal diffusivity of PuF_3 as pressed disk and as pre-molten disk measured with the LAF set-up. T = temperature (K), $\alpha = 10^{-6}$ (m^2/s)

PuF_3pp		PuF_3m		PuF_3m	
T	α	T	α	T	α
651	0.2279	553	0.6534	1056	0.5216
651	0.1964	552	0.6488	1056	0.5139
652	0.2186	553	0.6479	1056	0.5267
805	0.2287	637	0.6207	1097	0.5181
804	0.2474	637	0.6215	1097	0.5161
805	0.2510	637	0.6232	1057	0.4751
929	0.2606	702	0.6045	1093	0.4663
929	0.2433	702	0.6024	1093	0.4614
929	0.2231	702	0.5968	1128	0.4655
994	0.2625	759	0.5856	1128	0.4532
994	0.2671	760	0.5952	1128	0.4650
994	0.2946	760	0.5864	1162	0.4696
1062	0.2744	815	0.5580	1162	0.4605
1062	0.2945	815	0.5642	1162	0.4673
1062	0.2928	815	0.5661	1196	0.4527
1126	0.2549	868	0.5547	1196	0.4466
1126	0.3052	868	0.5479	1196	0.4668
1126	0.3328	868	0.5564	1250	0.4603
1183	0.2231	919	0.5510	1250	0.4070
1183	0.2758	919	0.5598	1250	0.4557
1183	0.2276	919	0.5495	1292	0.4563
1259	0.3823	969	0.5476	1292	0.4182
1259	0.2213	968	0.5389	1292	0.4704
1259	0.2306	968	0.5491	1346	0.5280
1350	0.2428	1013	0.5188	1346	0.3528
1350	0.2141	1013	0.5348	1346	0.3623
1350	0.2962	1013	0.5435		

Table 3.6: Thermal diffusivity of molten salt fuel mixtures measured with the LAF set-up. T = temperature (K), $\alpha = 10^{-6}$ (m^2/s)

LiF-ThF_4		LiF-ThF_4-UF_4		LiF-ThF_4-UF_4-PuF_3	
T	α	T	α	T	α
729	0.6049	547	0.4780	560	0.1066
728	0.6019	547	0.5001	561	0.1061
628	0.5858	547	0.5112	561	0.1065
626	0.5717	630	0.4753	647	0.1105
625	0.5789	630	0.4776	647	0.1127
545	0.5756	631	0.4847	646	0.1149
545	0.5704	696	0.4647	702	0.1178
545	0.5869	696	0.4326	702	0.1186
		696	0.4496	701	0.1188
		750	0.4511	754	0.1040
		750	0.4369	754	0.1037
		750	0.4657	754	0.1043
		803	0.4077		
		803	0.3935		
		804	0.4127		

4

AN ULTRASONIC SHEAR WAVE VISCOMETER FOR LOW VISCOSITY LIQUIDS

Our task, your task...is to try to connect the dots.

Donald Rumsfeld

An innovative method based on ultrasonic wave propagation has been developed for the determination of the viscosity of low viscous fluids. A waveguide is used to remotely transmit the ultrasonic waves from a shear piezoelectric transducer into the liquid. At the solidliquid interface, a guided wave mode, the shear mode, is used to extract the liquid viscosity. The amplitude of the reflected ultrasonic wave depends upon its operating frequency, the physical properties of the liquid (viscosity and density), and the waveguide (density and shear modulus). The results show that the attenuation of the amplitude of the waves, and thus the viscosity of the liquid, can be accurately retrieved using this method. Measurements on water, ethanol, and mixtures of water/glycerol illustrate that the method can successfully monitor changes in attenuation due to the viscosity of the liquid. The range of viscosities measured was between 0.8 and 60 mPa-s. Compared to literature values, the relative error for these measurements was lower than 12% while the uncertainty in the measurements was always lower than 5 %. Measurements were also performed varying the dimension of the waveguide and the container for the liquid with the goal of minimizing the liquid analyzed. Higher temperature measurements, up to 70°C, were also performed with the goal of transforming the current setup in a high temperature setup.

Parts of this chapter has been published in Measurement Science and Technology.
S. Mastromarino, R. Rook, D. De Haas, E. Verschuur, M.Rohde, J. L. Kloosterman. An Ultrasonic Shear Wave Viscometer for Low Viscosity Newtonian Liquids

Besides its ability to measure low viscosities, this method offers advantages such as the capability to perform in situ measurements, the omission of mechanical parts and the possibility to handle very small volumes of liquid.

4.1. INTRODUCTION

The fuel salt in Molten Salt Fast Reactors (MSFR) serves the dual function of both nuclear fuel and coolant. For this latter function of the salt it is necessary to evaluate its efficiency as a heat transfer medium. For example, the accurate measurement of the viscosity is necessary to predict the flow and turbulent heat transfer of the fuel salt through the primary reactor circuit. Even if the viscosity of molten salts has been studied since 1952, the measurements show large discrepancies [1]. Furthermore, the effects of adding actinide fluorides, as UF_4, ThF_4 and PuF_3, on the viscosity is still under investigation. Previously, experimental groups have developed suitable instruments based on different techniques, namely rotational and vibrational, for measuring the viscosity of molten salts. At the Oak Ridge National Laboratory Cohen and Jones [2] and later Cantor [3] used a modified form of the Brookfield rotational viscometer. Chrenkova [4] and a group in Kurchatov institute [5, 6] developed a torsion viscometer. Many of these techniques need a large amount of liquid for the measurement (in the order of 100 grams). This should be avoided for real fuel salt considering the high radioactivity of the salt. The characteristics of the salt of being corrosive, radioactive, liquid at temperatures above 500°C impose severe requirements on the measuring equipment: a remote measurement where the salt is not in contact with the instrumentation is preferred. Also the severe reaction of the salt with oxygen and moisture complicate the experimental manipulation of the apparatus and samples. An other important characteristic to take into consideration for the viscosity measurement is also that the predicted viscosity of the salt varies from approximately 2 to 15 mPa·s [7]. A sensitive method is required in this range of viscosity.

The necessity of the determination of the viscosity of liquid nuclear fuel used in the molten salt reactors (MSRs) led to the study of a technique which allows one to measure the ultrasonic attenuation of liquid in harsh environments. Measuring the viscosity of liquid nuclear fuel can be difficult because of the corrosivity and radioactivity of the nuclear fuel used in MSRs.

In many industrial applications one can find low viscosity liquids in harsh environments, such as high temperatures, high corrosion or high radioactivity. One example is the nuclear fuel used in the molten salt nuclear reactors (MSRs). Measuring the viscosity of liquid nuclear fuels is difficult because of the high temperatures and levels of corrosion and radioactivity. These conditions impose severe requirements on the measuring equipment: a remote measurement where the salt is not in close contact with the electronic instrumentation is preferred.

A technique that may overcome the aforementioned difficulties consists of the use of ultrasounds in a waveguide. The usage of ultrasound for measuring material properties started in 1949 with Mason et al., who placed the transducer in direct contact with the liquid [8]. This is, however, not possible for measuring corrosive liquids that can destroy the piezoelectric element in the transducer. The high temperature is also a limitation for the transducer. Above the Curie temperature of the transducer, the piezoelectric activity is lost and high-temperature transducers are not yet available [9]. Therefore, a waveguide is used to separate the transducer from the liquid.

In 1971, Hunston et al. [10] proposed the measurement of the shear properties of liquids using a strip waveguide immersed in a liquid. In their experiment, an aluminum strip is connected to a transducer and placed in a empty cell. The cell is then filled with the liquid sample to be measured until the sample touches the transducer. The change in attenuation of the waves is measured when the strip is in air and then when it is immersed in the liquid sample. The attenuation is expressed in terms of the viscosity. With this technique, Hunston measured a viscosity as low as 3.6 mPa·s with an error respect to the literature value between 30 and 40 %. Knauss et al. [11] repeated the measurement proposed by Hunston to obtain a better accuracy of the results. Through the use of a longer waveguide and a different frequency, a higher attenuation was achieved and the measurements of the viscosity had a maximum relative error of 11 %. The method proposed by the group of Hunston and Knauss is based on the attenuation of the wave in a waveguide completely immersed in the fluid. In their system the transducer is in contact with the fluid. This makes this system not suitable for corrosive fluids or at high temperature.

The potential applications of ultrasounds to measure viscosity at high temperature was first reported in 1996 by Shah [12]. Shah measured liquids with viscosities between 2 and 10 Pa·s up to 60°C. Prasad et al. [13] have reported ultrasonic studies based on longitudinal waves on glass melts using a measuring system comprising ultrasonic waveguides of alumina. They have developed an experimental apparatus to measure, in situ, the viscosity of molten glass at elevated temperatures (up to 1250°C). In their method, guided waves are generated through a cylindrical buffer rod and the reflection coefficient is measured. From the relation between the reflection coefficient of a wave at a solid-liquid interface and the acoustic impedance of a liquid, the product of density and acoustic velocity, the viscosity can be obtained knowing the density of the liquid [14]. Since the impedance determines the ability of an ultrasound wave to pass from one medium to another, in the reflection coefficient method, attention should be given to the choice of the material of the buffer rod. The effectiveness of this measurements method is reduced when there is a mismatch of the impedance between the solid and the liquid, which reduces the possible materials for the buffer rod suitable for low viscous liquids at high temperature.

More recently, Vogt et al. [15] measured the viscosity of glycerol (1.15 Pa·s) and the commercial Cannon VP450 viscosity standard (1.42 Pa·s) measuring the change in the attenuation coefficient, as proposed by Hunston, but using a cylindrical wire as the waveguide. A rectangular waveguide was used instead by Cegla [16], who obtained the density and viscosity of a liquid simultaneously by measuring the attenuation and the velocity of the guided waves [17]. Both Cegla and Vogt have measured the viscosity of different liquids, from 1 to 13 Pa·s with errors relative to the literature values of maximum 4 %.

Gitis et al. [18] also used the measurement of the attenuation coefficient, but proposed an alternative approach to using a rectangular waveguide. Gitis et al. identified the limit of the method in placing a transducer on the strip end surface of the waveguide. The attenuation, and the accuracy of the measurement, can be increased if the surface of contact between the piezoelectric element and the waveguide is higher. Gitis et al. designed a set up in which the waveguide is shaped as a ribbon and it is hermetically sealed in a vessel filled with the liquid sample. The intensity of the waves and their attenuation is optimized by using an angle ultrasonic transducer glued to the waveguide, obtaining a higher surface of contact with the waveguide. The difference in amplitude between the signal when the vessel is empty and then filled with the sample is used for the measurement. With this method Gitis et al. measured the viscosity of liquids as low as 1 mPa·s with a relative error of 1 %. A substantial increase in the accuracy was achieved for the attenuation method for measuring the viscosity. The disadvantage of this method for measuring aggressive liquids is that the waveguide has to be completely immersed in the liquid, therefore a large volume (more than 200 ml approximately) is needed. When measuring molten salt fuels, for example, a large volume has to be avoided because of their high radioactivity.

Table 4.1 summarizes the previous measurements that have been done using a waveguide for measuring the viscosity of fluids. These works have been based on the measurement of either the reflection coefficient at the solid-liquid interface or the attenuation of the longitudinal, torsional or shear modes in cylindrical or rectangular waveguides when immersed in a liquid sample. Both the techniques have been successful in different ranges of viscosity reporting results with relative error as low as 1 % [18]. While the reflection coefficient technique has the difficulty of finding a waveguide that is compatible to the liquid, the attenuation measurements have met the difficulty to reach the necessary accuracy of the measurement. For many of these techniques a large amount of liquid is needed, an incompatible characteristic for harsh liquids.

In this work we have chosen to measure the viscosity from the attenuated shear waves in a plate waveguide for several reasons. First, the shear waves do not show dispersion, the wave packets do not change phase velocity while travelling along the waveguide and maintain their shape [15]. Second, these waves do not convert into other modes when the plate is immersed in a liquid, making the interpretation of the measured signal easier [16]. Third, the shear waves are highly attenuated by the viscosity of the liquid resulting in a high sensitivity to low viscous liquids [20]. The advantage of the set up proposed in this work is that a very thin plate and a small amount of liquid are used for the measurement, differently than the set up proposed by [18]. The set up proposed is very similar to the one used by [16], but we used this method for measuring low viscous liquids.

This non-destructive method is based on wave pulses of short ultrasonic waves at high frequencies (MHz range) travelling through a plate that is partially immersed in the liquid. The piezo-electric transducer is placed on top of the waveguide, and is, thus, physically separated from the liquid, eliminating problems that might arise from a liquid under harsh conditions. The distance of the transducer from the liquid and the small interface between transducer and plate waveguide will allow the transducer to remain at low temperature. By doing measurements at different immersion depths the determined attenuation of the wave pulse can be used to derive the viscosity. The attenuation is measured while the waveguide is immersed in the liquid, therefore it is easier to perform an experiment varying the temperature.

In the section 4.2 of this chapter, the theory on which the ultrasonic technique is based is described. A more descriptive section is dedicated to the shear horizontal wave attenuation method since this is the chosen mode for the measurements presented here.

Table 4.1: Previous measurement of the viscosity using a waveguide.

	Hunston (1972) [19]	**Knauss (1973)** [11]	**Shah (1996)** [12]	**Vogt (2004)** [15]	**Cegla (2005)** [16]	**Prasad (2008)** [13]	**Gitis (2012)** [18]
Viscosity (Pa·s)	0.00364 - 100	0.001 - 0.02	1.994 - 10.45	1	1 - 13	18 - 6300	0.001 - 1
Error (%)[a]	30 - 40	11	3	2	4	3	1
Method	attenuation of the SH0 mode	attenuation of the SH0 mode	reflection coefficient technique	attenuation of T(0,1) and L(0,1)	attenuation of the Quasi-Schoelte mode	reflection coefficient technique	attenuation of T(0,1) and L(0,1)
Frequency (MHz)	1.6	2.1	1 - 2.25	0.25 - 0.4	0.5	0.25	2 - 5
Fluid	polydimethyl-siloxilane, toluene solution of polystyrene	toluene, water, propanol, dibutyl phthalate, diethyl phtalate	calibration fluids	glycerol (1% water) and Cannon VP450	glycerol, honey, water with suspensions	glass	40, 50 and 60 % solutions of saccharose in water
Waveguide	aluminum plate (1.1 mm thick)	aluminum plate (1.1 mm thick)	plexiglas, graphite, aluminum plates	steel rod (0.25 to 2.5 mm radius)	steel plate (1 mm thick)	aluminum rod (4.75 mm radius)	aluminum plates (0.3 x 140; 0.2 x 200 mm)
Temperature (°C)	30	25	30 - 60	room temperature	room temperature	up to 1250	20 - 40

[a] The error is relative to the literature value.

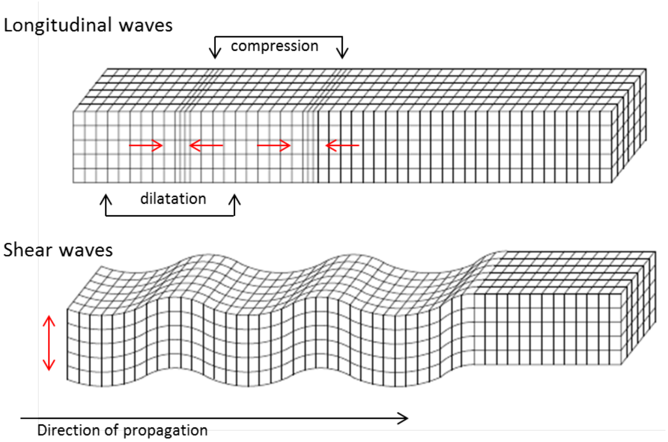

Figure 4.1: Propagation of longitudinal and shear waves.

Then, in section 4.3, the experimental set-up and procedure are described. Section 4.3.2 is dedicated to the data processing and section 4.3.3 to the determination of the accuracy of the method. Results are shown in section 5.3, followed by conclusions.

4.2. BACKGROUND

The principle used for evaluating the viscosity of liquids is based on a high frequency wave that is transmitted in a solid guide and attenuated by the shear motion within the liquid in which the guide is immersed. A transducer generates a wave and sends it through the waveguide. The wave's mode can be generally of two different types, depending the way in which the piezoelectric material inside the transducer is cut. The two main kind of waves are longitudinal and shear waves, as shown in Figure 4.1. The longitudinal waves, also known as pressure waves, have the same displacement direction as the propagation direction of the waves, meaning that they expand and contract in the propagation direction of the waves. While the longitudinal waves transmit in liquid, gas and solids, shear waves can be sustained by solids only [21, 22]. Shear waves are polarized perpendicularly to the propagation direction. More specifically, in the case of a thin plate with respect to the wavelength of the signal, these waves are polarized in the plane of the plate.

When the plate is embedded in another material, the shear wave energy can partially leak towards this material via their mutual interface and be attenuated. The attenuation of the shear waves is different depending on the medium surrounding the plate.

When the embedding material is a liquid, the waves are transmitted in the liquid as bulk waves [23]. In this case there is a distinction between the transmission of waves that can occur if the liquid is viscid or inviscid. If the liquid shows no viscous behaviour, only out-of-plane displacements, shown only by longitudinal waves, can be transmitted in the liquid since shear stresses do not exist in inviscid liquids [24]. Consequently the attenuation of the longitudinal waves will be only due to the radiation of energy into the medium [25]. When the plate is immersed in a viscous liquid, shear stresses may appear as well in the surrounding liquid and the guided waves, both longitudinal and shear, propagating in the plate can be attenuated due to viscous dissipation [17].

The shear wave that is excited in this work is the plate mode commonly referred to as SH0 mode. This mode does not introduce longitudinal waves in the surrounding liquid. Therefore, shear is the only mechanism that causes energy loss in the plate.

The rate of the attenuation of the shear wave depends on the material properties of the waveguide and of the surrounding liquid, together with the frequency of the propagated wave. By measuring the attenuation of the reflected shear wave in the plate, the viscosity of a Newtonian fluid can be calculated by the approximation derived by Cegla et al [26],

$$\alpha = -\frac{1}{2h}\left(\frac{2\rho_f \omega \eta}{G\rho_s}\right)^{1/2}, \tag{4.1}$$

where α is the attenuation of the wave, h is the thickness of the plate, ρ_f is the liquid density, η is the liquid dynamic viscosity, G is the shear modulus of the plate, ρ_s is the plate density and ω is the angular frequency of the shear wave. The derivation of Equation 4.1 is shown in the Appendix A 4.6. This formula works well if the frequency thickness, being the product $h \cdot \omega / 2\pi$, is up to about 2 MHz·mm. Above this value, the SH0 mode shape becomes frequency dependent. Cegla et al. [26] showed that the deviation between Eq. 4.1 and its exact solution is 0.04% when the frequency-thickness is 1 MHz·mm. For this reason, this value for the frequency-thickness will be used in this work.

The dissipation of the shear waves in the liquid depends on the viscosity, and thus on the shear stress. It can be shown [17] that the attenuation shows an exponential decay along the direction of propagation, i.e. $\sim e^{-\alpha X_1}$. From the derivation of the velocity profile in the liquid one can recognise a length scale over which the shear waves propagate in the liquid perpendicularly to the plate surface. This length scale is the viscous skin depth of the wave that defines the distance a wave will travel before the amplitude of the wave decays with a factor of $1/e$. The viscous skin depth, δ, is defined as:

$$\delta = \left(\frac{2\eta}{\rho_f \omega}\right)^{1/2}. \tag{4.2}$$

For example, the measurements in water with a viscosity of ca. 1 mPa·s and a density of 1000 kg/m^3 using a transducer with a frequency in the MHz range, result in a the viscous skin depth in the μm range. The same is valid for the highest viscosity we measured ($\sim$ 50 mPa·s). This means that the container holding the liquid can be very small and will allow measurements with merely a few ml of liquid.

4.3. EXPERIMENTAL SETUP

The temperature range of interest for the measurement of the viscosity of molten salts is between 400 and 1200°C. In the ultrasonic method presented in this work, the viscosity is measured using a piezoelectric transducer that can not operate at these high temperatures. Above the Curie temperature of the transducer, it does not generate waves anymore. Therefore, a waveguide is used between the transducer and the investigated liquid. The setup (see Figure 4.2a) was designed to excite and transmit shear waves through

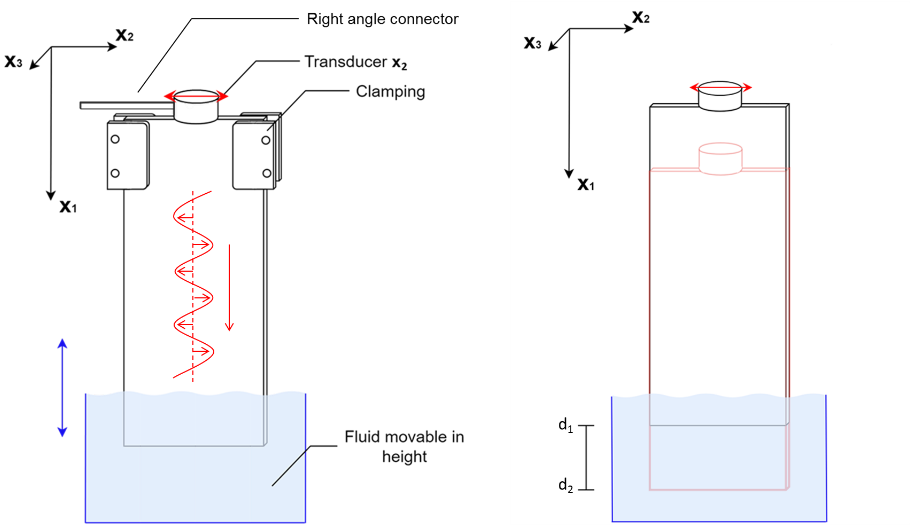

(a) (b)

Figure 4.2: Schematic of the waveguide immersed in liquid. The clamping is shown (a) as well as the mechanism of immersion depth (b).

the waveguide. The waveguide is a metallic plate, with a melting point higher than the operating temperature of the molten salt, that is immersed in a liquid of which the viscosity has to be measured. The waveguide guides the ultrasonic waves generated by the transducer, placed at one end of the waveguide, to the liquid and back to the transducer. The transducer converts the electrical signal into a mechanical signal, a displacement wave, which is transferred to the waveguide. A shear transducer V-155RM by Olympus (Normal incidence shear wave) with a peak frequency of around 5 MHz and a diameter of 13 mm is used for the production of shear waves. The transducer is clamped at the top of the plate and is used to excite SH (shear horizontal) waves, with displacements in the x_1x_2 plane. Note that by rotating the transducer around the x_1 axis, by $\pi/2$ rad, the polarisation of the waves can be chosen to flexural waves if desired (not in this work). The transducer is such that the direction of the polarization of the shear wave is in line with the right angle connector. After transmission to the plate, the wave moves along the x_1 direction. Its path should be free of obstructions that may cause distortion of the wave. As such, the clamps (indicated by Clamping in Figure 4.2a) are put at some distance from the middle of the plate to prevent the distortion. By putting pressure at the edges and at the centre of the plate, it was tested if the clamps would be of influence on the wave attenuation. No change in the amplitude of the reflected wave was observed when pressure was applied on the edges of the plate, while the wave was strongly attenuated when pressure was applied in the centre, confirming that the clamping can be safely attached to the sides of the plate. To install the transducer, pressure is applied downwards on top of the transducer, after which it is clamped on the sides and the pressure on the top is released. To enhance traction between the transducer and the very thin plate (0.1 mm thickness), a shear couplant SWC-2 by Olympus (couplant and adaptors) is used. The

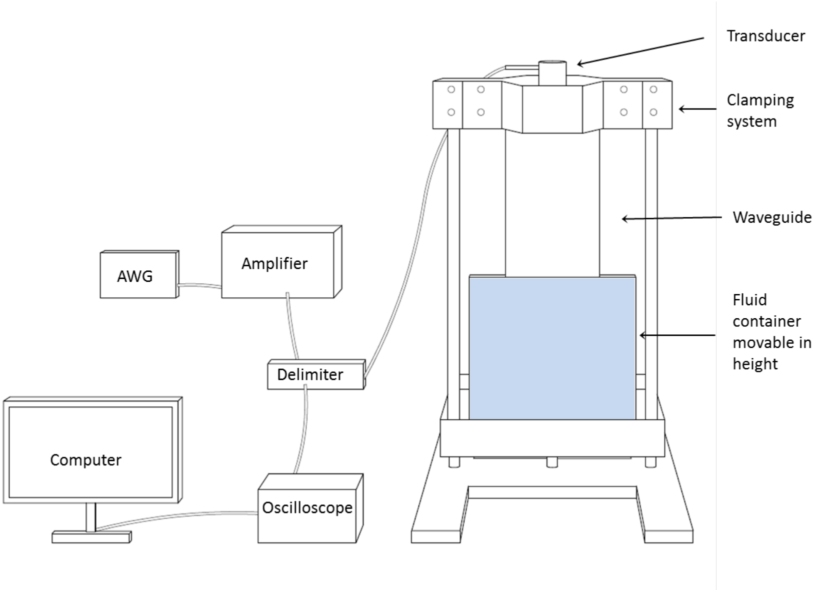

Figure 4.3: Schematic of the setup including the electronics to record the waves.

connection between the transducer and the plate is essential in the stability of the transmitted signal. This connection depends on the alignment of the transducer on the place. To obtain an intense signal, the middle of the transducer has to be exactly on the place as this maximizes the contact area between the transducer and the plate.

Figure 4.3 shows a schematic drawing of the experimental setup. In Figure 4.4, a photo of the experimental setup for measuring the viscosity at room temperature is shown. Connected to the transducer, an arbitrary waveform generator DG1022A by Rigol (Arbitrary Waveform Generators, AWG) is used to generate a sinusoidal wave packet of 40 cycles with a frequency in the ultrasonic range. Each wave packet consists of 40 cycles to assure that a sinusoidal wave is obtained at a constant chosen frequency. A wave packet consisting of few cycles shows an exponential decay that interferes with the measurement of the attenuation. The wave packet is repeated with a delay of 30 ms. This delay is needed as the waves get reflected many times in the waveguide before they are fully attenuated. The amplitude of the generated signal is chosen as high as possible, to get the highest signal to noise ratio. The amplitude of the generated signal can be limited by a couple of things: the generator, the amplifier, the oscilloscope, and the transducer. The signal generator has a maximum output voltage of 10 Vp-p (Peak-to-Peak Voltage). The transducer is preferably used with no voltages higher than 100 V. If the transducer is used a long time at continuous excitation voltages of 300 V or higher, it could be re-poled to a longitudinal wave transducer. This is an irreversible effect, so good care has to be taken in not exposing the transducer to these voltages continuously. The oscilloscope used is the Keysight InfiniiVision DSOX2024A, which has a maximum input voltage of 200 Vp-p. The maximum voltages for the transducer and the oscilloscope are higher than the

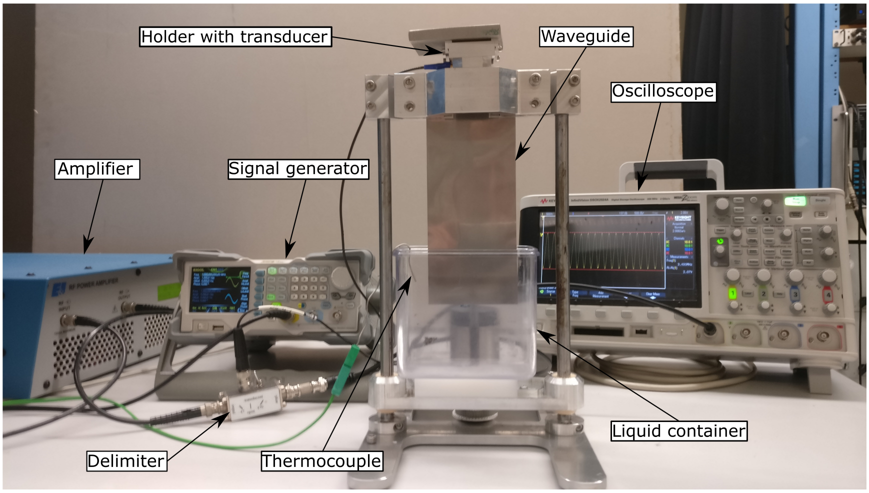

Figure 4.4: Photo of the setup used for the room temperature measurements of the viscosity. All the electronic parts are shown and indicated.

maximum output voltage of the signal generator. Therefore, a radio frequency amplifier 2100L by E & I (E. I. Innovation, 100W, 10 kHz - 12 MHz RF amplifier) is used to amplify the signal outputted by the generator. The amplifier used in this work can only withstand an input signal of +13 dBm without damage, corresponding to 1 V. This limits the output signal of the generator to $2\sqrt{2}$ Vp-p. To be below the limit, the amplitude of the wave is set to 1 Vp-p. The amplifier has a gain of 50 dB, which amplifies the 1 Vp-p signal to around 300 Vp-p. This is higher than recommended for the transducer, but as the waves are sent in bursts, it is not excited continuously with this voltage. The oscilloscope is not made to withstand these high voltages, and therefore a delimiter was fabricated to limit the voltage that is sent to the oscilloscope. The delimiters is placed between the amplifier, the transducer and the oscilloscope. The delimiter splits the input signal from the transducer and the received signal and decreases the voltage sent to the oscilloscope while sending the amplified signal to the transducer.

The SH0 waves propagate along the plate until the location where the plate is in contact with the liquid. By inserting the plate into the liquid, as shown in Figure 4.2b, the shear waves are attenuated due to the viscous shear the liquid exerts on the plate. The signal is then entirely reflected at the end of the plate, travels back to the transducer and is recorded. The measurement of the attenuation α is based on the intensity of the waves at two immersion depths of the plate in the liquid as follows:

$$\alpha = -\frac{1}{2(d_2 - d_1)} ln \frac{S_2(\omega)}{S_1(\omega)}, \tag{4.3}$$

where $d_1 < d_2$ are two different immersion depths, and $S_2(\omega)$ and $S_1(\omega)$ are the received signal amplitudes at the respective immersion depths and at frequency ω. The immersion depth is altered by moving the liquid container, placed on an elevator that can be steered automatically with an electromotor. A ruler can be used to gauge the insertion

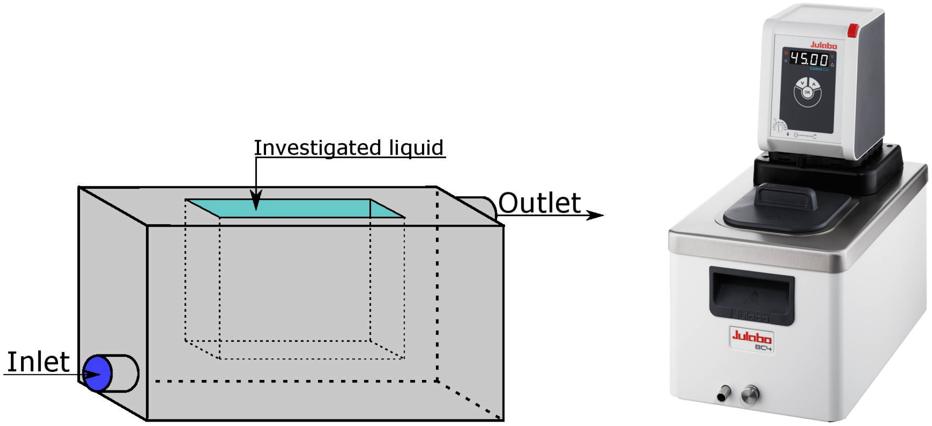

(a) Liquid container for high temperature measurements

(b) Thermostatic bath

Figure 4.5: Schematic of the container for the measurements at high temperature (a). The container is heated at a temperature between 25 and 70°C by flowing water heated using a thermostatic bath (b).

depth, although it can also be set at a regular insertion depth by the electromotor. In principle it is sufficient to perform a measurement at only two different depths to evaluate the attenuation and consequently from equation 4.1, calculate the viscosity. However, to increase the accuracy of the measurements, the plate was immersed in the liquid at several immersion depths, typically ten. Each measurement was performed by increasing the immersion depth of the stainless steel plate by steps of 0.40 cm. The height of the container (82 mm) allowed to obtain the signal from a minimum of ten immersion depths. The maximum volume of the container is 45 ml, this is a small volume for a density measurement and it is ideal for measuring liquids in a harsh environment. It must be noted that hysteresis in the level of the liquid was observed, where the liquid could differ in height by approximately 0.5 mm between the cases where the plate was inserted into the liquid and the cases where the plate was extracted from the liquid. This phenomenon, caused by the creation of a thin film of liquid during extraction of the plate, was mainly observed for viscous liquids, in the order of 50 mPa·s, while it was not observed for water. Therefore, it was chosen to perform measurements by inserting the plate in the liquid only.

The liquid temperature was recorded during the experiments using a thermocouple that was immersed in the liquid.

HEATING SETUP

Considering the final application of the waveguide viscometer for measuring molten fuel salt, liquid at a temperature above 300°C [27], the setup was modified for performing measurements at high temperature. The first step was to design a setup for measuring liquids at a temperature higher than room temperature. A container was fabricated made of stainless steel and having a double wall. The container was heated by water flowing through the double wall. Figure 4.5a shows a schematic view of the liquid container. The water is heated by a thermostatic bath (in Figure 4.5b [28]) before entering the container through two hoses attached to the inlet and outlet nozzle of the liquid container. The thermostatic bath controls the temperature of the water that is pumped though the double wall with an accuracy of 0.03°C. The setup can work from 20°C to 70°C, another setup should be designed in the future for the application at higher temperatures. The space indicated as "investigated liquid" in the figure is where the liquid under investigation is placed.

FALLING BALL VISCOMETER

The results obtained with the waveguide viscometer had to be validated. For the used liquids, there are experimental data in literature that can be used as a reference. However, for some liquids, like the water/glycerol mixtures, less experimental data are available in the literature, and the fractions in the mixture may change over time. This might cause a false comparison between the experimental results and the literature results. To take this into account, a simultaneous measurement of the viscosity with another viscometer would be ideal. A commercial falling ball viscometer [29] was used to get a reference viscosity for the liquids. The falling ball viscometer consists of a turnable tube and a ball. The liquid, of which the viscosity has to be measured, and the ball are inserted in the tube. The time it takes to the ball to fall through the liquid is measured. The falling time is directly proportional to the viscosity as it will be explained. Three forces are acting on the falling ball: the gravitational force, the buoyancy force and the drag force. Since the ball rolls in the fluid, the drag is caused by the friction of the fluid against the ball. The principle of the falling ball viscometer only works for laminar flows, which means that the ball may not fall too fast through the tube. The tube in this falling ball viscometer is inclined by a predefined angle of 10°[30]. As the tube is inclined, the ball does not only fall through the tube, but it also rolls and, thus, follows a well defined path. To determine all the forces acting on the falling ball, a constant K has to be empirically determined by doing experiments on calibration fluids with a well-known viscosity. The expression for the viscosity of the measured fluid results in:

$$\eta = K(\rho_b - \rho_l)\,t \tag{4.4}$$

where η is the viscosity in mPa·s, K is the ball constant in mPa·cm^3/g·s, ρ_b and ρ_l are the density in g/cm^3 of the ball and the liquid respectively, and t is the time in seconds it takes for the ball to fall. The ball constants K are already determined by the manufacturer of the viscometer [29].

The falling ball viscometer, shown in Figure 4.6 is equipped with a circulation jacket filled with water that might be heated to measure the viscosity at temperatures between 25 and 50°C. The thermostatic bath, used also for the waveguide setup, is used to pump water with a fixed temperature around the falling tube. There are some considerations that have to be taken into account when doing measurements with the falling ball viscometer. The inner tube and the used ball have to be cleaned very neatly. Every little particle influences the falling time of the ball and thus gives an error in the results. The same holds for air bubbles inside the inner tube. Another thing that has to be kept in mind is the thermal expansion of the liquid. If the water from the thermostatic bath heats the liquid inside the inner tube, the liquid expands. The expansion builds up pressure inside the inner tube and if this becomes too high, the tube may break. Therefore,

1. Falling tube
2. Ball
3. Circulation jacket
4. Screw
5. Set screw
6. Gasket
7. Cover
8. Brace
9. Jacket tube
10. Hollow stopper
11. Stopper
12. Capillary
13. Closing plate
14. Gasket for falling tube
15. Threaded bush
16. Connecting rod

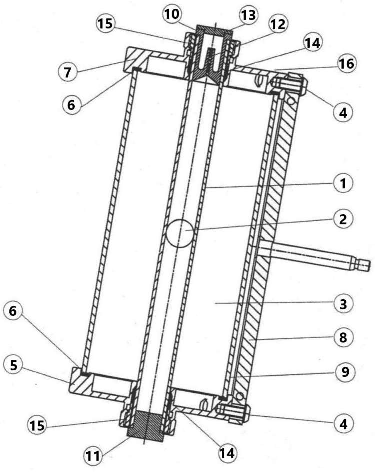

Figure 4.6: A schematic representation of the falling ball viscometer.[29]

the closing plate has to be taken off when the liquid is heated. In this way, the pressure in the inner tube stays the same as the pressure around the tube.

4.3.1. Materials and equipment

Waveguide

The choice for the material of the waveguide was based on the resistance to corrosion in contact with molten fluoride salts. Several studies have been done to test the chemical resistance of metals and other reactor materials to fluoride salts [31, 32]. The waveguide should be able to send and receive the signal to and from the liquid or the material that has to be investigated. This should be done losing the minimal amount of intensity of the signal. Metals work well in this sense, ceramic materials as alumina, graphite or boron nitrate, although very good in resistance to corrosion of fluoride salts, are very porous and highly attenuate all the waves. When a graphite rod was tested as a waveguide for measuring the attenuation in water, no signal back was detected. Therefore, thin metallic plates were used as a waveguide, in this work, mainly of stainless steel due to its availability. This is not a metal resistant to corrosion and it was used on common liquids only, to study the method and develop the setup. A tungsten plate was also tested, as this is a good material for both its resistance to corrosion and acoustic properties. The properties of the plates used are shown in Table 4.2.

The thickness of the plate is an important parameter since it determines how much the liquid attenuates the waves. The signal intensity rises with increasing thickness of the waveguide, but the attenuation decreases with increasing thickness, which follows from equation 4.1. In thin plates, the liquid attenuates the waves more than in thick plates as the surface to volume ratio is higher. On top of this, there is a maximum thickness of the plate after which dispersion of the waves occurs. Above the cut-off frequency-thickness

Table 4.2: Material properties and dimension of the waveguides.

Material	Thickness	Width	Length	Density	Shear modulus	SH0 velocity
	mm	mm	mm	[Kg/m^3]	[GPa]	[m/s]
Stainless steel	0.202	80.2	203.5	7874	74.86	3083.3
Stainless steel	0.203	60.6	201.5	7800	74.19	3084.0
Stainless steel	0.206	40.8	200.0	7734	73.42	3081.2
Tungsten	0.108	80.1	200.3	18231	147.4	2839.0

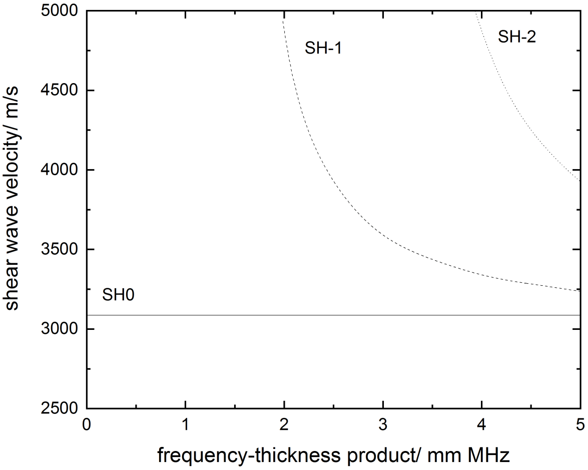

Figure 4.7: Wave velocity of the fundamental shear horizontal wave mode and the first two higher order shear wave modes as a function of the frequency-thickness product of a stainless steel plate.

product, higher-order shear wave modes exist besides the SH0-mode. For a frequency of 3.5 MHz, this maximum thickness is 0.44 mm for a stainless steel plate and 0.40 mm for a tungsten plate calculated using [33]:

$$fh = \frac{nc}{2}, \tag{4.5}$$

where f is the frequency of the wave, h is the thickness of the plate, n is any positive integer and c is the shear wave velocity.

The above described effect can be seen in Figure 4.7. The phase velocity as a function of the frequency-thickness product for the fundamental and higher-order SH modes is displayed for a stainless steel plate. Above the cut-off frequency-thickness, the fundamental shear horizontal wave mode is not the only shear wave mode present in the plate. For stainless steel, this cut-off frequency-thickness is 1.5 mm·MHz calculated using equation 4.5.

In theory, it would be better to choose a very thin plate as the attenuation will be more significant, and the exponential fit can be more accurate. There is, however, a downside using a thinner plate, which is the lower signal-to-noise ratio of the reflected signal because a thinner plate is more subject to mechanical fluctuation that will interfere with the intensity of the signal

The width of the plate needs to be at least larger than the width of the transducer. The dimensions of the setup restrict the length of the plate. The plate has to fit in the setup, and the container with the liquid has to be able to move upwards to perform measurements as a function of the insertion depth. The more the liquid level can move upwards, the better the measurement is because more measurements can be performed, increasing the accuracy of the results.

The thickness of the plate was measured with the 3732XFL-1 electronic micrometer by Starret. The micrometer was NIST calibrated and had accuracy of 0.002 mm. The width of the plate was measured with the 799A-6/150 electronic caliper by Starret, with accuracy of 0.02 mm. The caliper was also NIST calibrated. The length of the plate was measured with a measuring tape with an uncertainty of 0.1 mm, as reported by the manufacturer of the measuring tape.

Other properties of the plate, such as shear modulus and density, have to be known in order to accurately evaluate the liquid viscosity using equation 4.1. The density of the plate was calculated by the ratio of mass and volume, thereby measuring the weight with a common balance. The shear modulus can be obtained via $G = v_s \rho_s$ by knowing the density and the velocity of the shear wave in the metallic plate. The shear modulus, measured for the plates used and reported in Table 4.2, is in agreement with the values in literature [34]. The velocity of the shear wave in the metallic plate, v_s, was measured from the time of arrival of the first shear signal. Between each reflection, the wave travelled from the top of the plate to the bottom and then back to the transducer. This means that the shear wave velocity can be calculated by using $v_s = \frac{2l}{\Delta t}$. The velocity is in agreement with the range of literature values for the metals [35]. For stainless steel, a range of values for the shear wave velocity and shear modulus is reported since they depend on the different grades of purity of the metal [35].

CONTAINERS

Different containers are used to verify if the results on the viscosity are independent on the volume of the liquid measured. For measuring the molten salt properties it is important to minimize the amount of liquid needed for a viscosity measurement. Two of the containers, the ones in perspex, are for measurements at room temperature, while the stainless steel container is for the measurements at higher temperatures. In Table 4.3, the size of the containers is shown. The volume in the table is the maximum volume that fits in the container. Less liquid can be put in the container, but the immersion depth that can be reached is, as a consequence, also lower.

LIQUIDS

Five different Newtonian fluids and one non-Newtonian fluid have been analysed. The model used in this work is only valid for Newtonian fluids, but it can be used to investigate if the fluid is Newtonian or not by measuring the amplitude of the SH0 mode as function of the immersion depth of the plate in the liquid as it is explained in Section

Table 4.3: Dimensions of the containers.

Material	Height mm	Depth mm	Width mm	Volume ml
glued plates of perspex	80.5	15.2	110.6	135
glued plates of perspex	81.7	4.9	109.5	45
Stainless steel	98.0	17.2	104.6	175

4.4.1. The Newtonian fluids have a dynamic viscosity in the range between 0.8 and 50 mPa·s. Water, ethanol, both with a low viscosity, and three mixtures of water and glycerol with increasing volume fraction of glycerol, have been measured. For the water/glycerol mixtures, the two liquids were stirred until they were homogeneously mixed to last for the duration of an experiment (ca. half an hour). The mixtures were then stirred again and the experiment was repeated in order to check for the repeatability. The ratio between water and glycerol was chosen in order to have viscosity between 10 and 50 mPa·s, which is the range of the viscosity of interest for the future application of this technique to molten fluoride salts.

As the non-Newtonian fluid, in this work, ethylammonium nitrate (EAN), an ionic liquid with chemical formula $C_3H_8N_2O_3$, was selected.

The density of the liquids was calculated from the mass and volume ratio using an Erlenmeyer flask of 25 ml to measure the volume. The densities of the different solutions are summarized in Table 4.6.

Table 4.4: Properties of the liquids.

Liquid	Density [Kg/m^3]	Uncertainty %
Water	994.4	1.3
Ethanol 95 %	870.8	1.1
Water/Glycerol 40/60 vol %	1163.6	1.9
Water/Glycerol 30/70 vol %	1172.0	1.5
Water/Glycerol 25/75 vol %	1199.6	2
EAN	1197.2	1.5

4.3.2. DATA PROCESSING

The data were recorded using LabVIEW. The program recorded a predefined number of signal windows, 128 in this work, displayed on the oscilloscope. Each signal had a number of wave periods visible on the oscilloscope that depends on the used frequency. For the used frequencies in this research, each recorded signal contained between 15 and 20 wave periods. To obtain the signal strengths at each immersion depth, the 128 windows showing the reflected waves were averaged before calculating the intensity of the averaged wave. The background noise was considered to be a random signal with zero mean and a fixed variance, so when the windows were averaged, the background noise cancelled out. On top of that, the amplitude was constant over the whole signal, which means that the rms of this signal was the amplitude divided by $\sqrt{2}$.

For Newtonian liquids, the intensity of the reflected signal exponentially decays as a function of the immersion depth of the waveguide in the surrounding liquid, following:

$$S(x) = S_0 e^{-2\alpha(x-x_0)}, \tag{4.6}$$

which is a rearrangement of equation 4.3. Therefore an exponential curve was fitted through the measured rms of the intensity reflections at each immersion depth:

$$S_{fit}(x) = C_1 e^{C_2(x-x_0)}, \tag{4.7}$$

where x is the immersion depth of the plate and the two coefficients C_1 and C_2 are determined in such a way that the exponent fits the data best. Equation 4.6 and 4.7 were combined to obtain the attenuation as:

$$\alpha = -C_2/2. \tag{4.8}$$

4.3.3. ACCURACY OF THE VISCOSITY EVALUATION AND OF THE ATTENUATION MEASUREMENTS

The uncertainty of the viscosity derivation has been determined by applying:

$$\epsilon(\mu) = |\mu_0|\sqrt{2\left(\frac{\epsilon(h)}{h}\right)^2 + 2\left(\frac{\epsilon(\alpha)}{\alpha}\right)^2 + \left(\frac{\epsilon(\rho_s)}{\rho_s}\right)^2 + \left(\frac{\epsilon(G)}{Gs}\right)^2 + \left(\frac{\epsilon(\rho_f)}{\rho_f}\right)^2 + \left(\frac{\epsilon(\omega)}{\omega}\right)^2}. \tag{4.9}$$

In Eq. 4.9, $\epsilon(h)$ is the uncertainty in the thickness of the plate, $\epsilon(\rho_s)$ and $\epsilon(G)$ are the uncertainties in the density and shear modulus of the plate, $\epsilon(\rho_f)$ the uncertainty in the density of the liquid and $\epsilon(\omega)$ the uncertainty in the frequency. The $\epsilon(h)$ is based on the uncertainty of the caliper used for measuring the thickness of the plate, that is 0.002 mm. The uncertainty of the balance (i.e. 0.01 g) and of the volume measurement (i.e. 0.04 ml) is used to calculate $\epsilon(\rho_f)$ resulting in a relative uncertainty between 1.1 and 2.0 %. The relative uncertainty of 1% for both the density and shear modulus of the plate is retrieved experimentally according to the method given in section 4.3.1. The uncertainty in the angular frequency, $\epsilon(\omega)$, is the uncertainty of the frequency of the waves sent by the generator multiplied by 2π. The frequency of the generator has an uncertainty of 1 ppm, which corresponds to $3 \cdot 10^{-6}$ MHz for a frequency of 3 MHz.

The uncertainty in the attenuation $\epsilon(\alpha)$ was calculated through a total least-squares approximation of the data. The confidence bounds for the fit from equation 4.7 were calculated considering parameters that are a measure of the fit: the inverse R factor from QR decomposition of the Jacobian, the degrees of freedom for the error, and the root-mean-squared error [36]. By combining these parameters, 95% confidence intervals for the fit parameters and thus the attenuation was obtained. The difference between the fitted coefficient C_2 and one of the 95% confidence bounds was used for calculating the uncertainty of the attenuation. The relative uncertainty measured in α was up to 1%.

Substituting the standard deviations of the experimental dta to the total error on μ, one obtains the relative uncertainty of 5% in the viscosity.

4.4. RESULTS

4.4.1. ATTENUATION OF THE WAVE PULSE BY NEWTONIAN AND NON-NEWTONIAN FLUID

As described in Section 4.3, the attenuation of the shear waves in liquids was retrieved from the amplitude of the measured shear waves at a range of immersion depths. Figure 4.8a shows the measured decrease in intensity of the SH0 mode as a function of the immersion depth of the stainless steel plate with width of 80 mm in a mixture of water and glycerol 30/70 vol %. To show the repeatability of the method, three experiments, shown in figure 4.8a, were performed. The intensity differs between each set because the energy transferred by the transducer to the plate may vary (e.g. by disconnecting it in between two measurement series). According to Equation 4.3, however, only the ratio of two intensities for two or more immersion depths is of importance. It can be seen that the exponential fit predicts the attenuation accurately as shown in figure 4.8b. The experiments were therefore considered to be sufficiently repeatable. The exponential fitting for the intensity of the SH0 mode is valid only for Newtonian fluids for which the viscosity of the liquid is independent of the shear rate in the liquid. Non-Newtonian liquids have an apparent viscosity that depends on the shear rate in the liquid. This means that Equation 4.3 does not hold for non-Newtonian fluids. Therefore, the signal may not decay exponentially as a function of immersion depth for non-Newtonian fluids. This procedure was followed for each liquid analysed. The viscosity was then obtained using Equation 4.1.

A non-Newtonian fluid, the ionic salt EAN, was measured and the amplitude of the SH0 mode for the plate immersed in the salt is shown in Figure 4.9 as function of the immersion depth. It is evident that for the ionic salt the decay is not exponential and therefore the Equation 4.6 is not valid. This means that it is possible to recognise if a fluid is Newtonian or not from the fitting of the amplitude of the SH0 mode as function of the immersion depth. Since Equation 4.6 is not valid, another model has to be derived for evaluating the attenuation and the viscosity of non-Newtonian fluids from these experiments.

4.4.2. VISCOSITY MEASUREMENTS AS FUNCTION OF THE GLYCEROL CONTENT

At room temperature, liquids with a viscosity ranging from 0.8 to 60 mPa·s have been measured. The results showed that the viscosity of water/glycerol mixtures is very sensitive to the amount of water content in the mixture. Especially with very small amounts of water content, the viscosity drops significantly with the addition of water. The viscosity of a water/glycerol mixture with only 1% water is almost 20% lower than the viscosity of pure glycerol [37, 38]. In Figure 4.10, the viscosity of the water/glycerol mixtures as a function of glycerol content is plotted. These are results for a liquid temperature of 22 ± 0.5°C. The experimental values are compared in Figure 4.10 with the results obtained by Cheng [38] and revised by Volk and Kähler [39], shown by the dotted line.

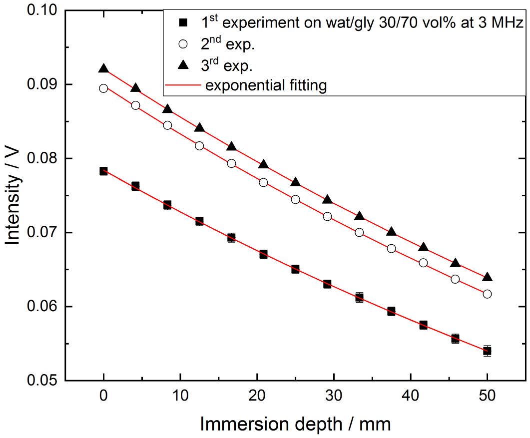

(a)

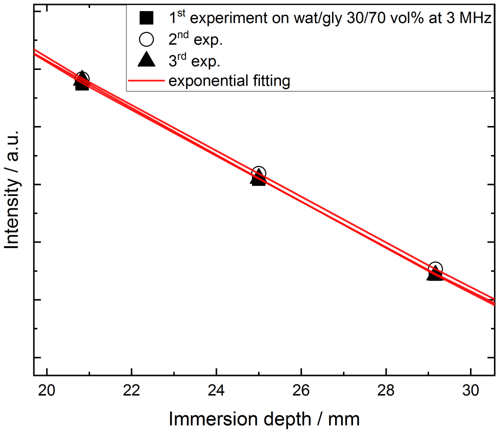

(b)

Figure 4.8: Amplitude of the SH0 mode for a stainless steel plate immersed in a mixture of water and glycerol 30/70 vol % at 3 MHz. The intensity was measured each 0.40 cm of immersion of the plate in the liquid. An exponential curve was fitted through the measured rms of the intensity reflections to retrieve the attenuation of the waves (α=3.82 ± 0.03, ■; α=3.79 ± 0.03, ○ ;α=3.72 ± 0.02, △). The experiment was repeated three times in order to increase the accuracy by averaging. The amplitude was normalized (b) to show the repeatability of the three measurements in retrieving the attenuation.

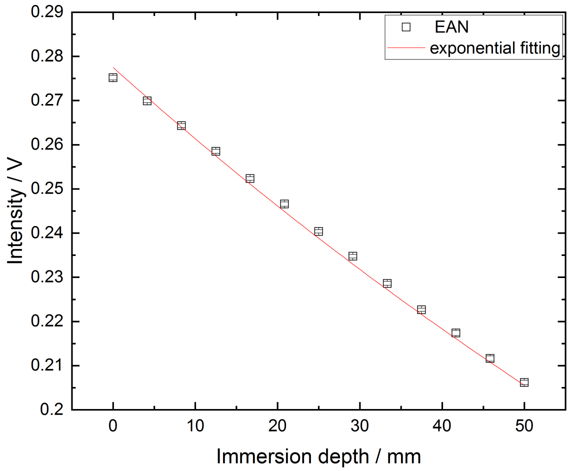

Figure 4.9: Amplitude of the SH0 mode for a stainless steel plate immersed in a ionic salt at 3 MHz. The intensity was measured each 0.40 mm of immersion of the plate in the liquid. An exponential curve was fitted through the measured rms of the intensity reflections

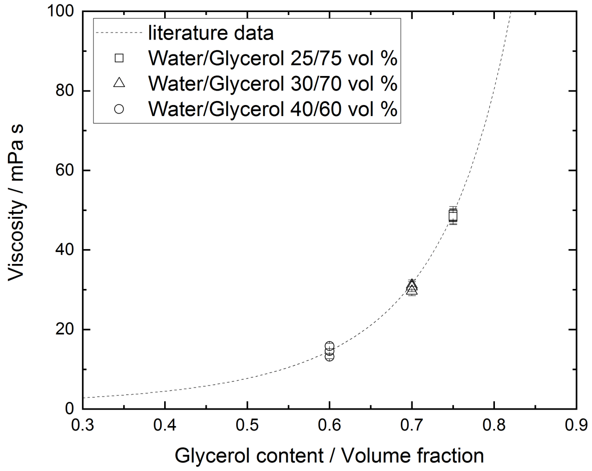

Figure 4.10: The viscosity of the water/glycerol mixtures,(◯ 40/60 vol %, △ 30/70 vol %, □ 25/75 vol %) as a function of volume% of glycerol at 22 ś 0.5 °C measured with the waveguide and calculated with an empirical formula (dashed line) by Cheng [38] and [39].

The viscosity measured in this work agrees within 5% to the results of Cheng. Besides the strong dependence on the water content, the viscosity of the mixtures is also very sensitive to the temperature fluctuations of the liquid as it is shown in Figure 4.11, where the results around room temperature are shown. In the temperature range between 19 and 22 °C the viscosity drops by almost 7%/°C. Therefore, it is important to measure the temperature of the liquid during measurements. The results are compared to the literature data by Cheng [38] in Figure 4.11 showing good agreement.

The measured attenuation and the viscosity calculated from the averaged attenuation measured at one single frequency is reported in Tables 4.5 and 4.6. The results are compared to the literature values and to the experimental results obtained with a commercial falling ball viscometer [29], used to validate the results obtained with the waveguide viscometer. In Figure 4.13a, the comparison between the viscosity measured with the ultrasonic waveguide viscometer and the literature values shows a good agreement. For the low viscosity of water, with measured viscosity of 0.88 ± 0.04 mPa·s, the relative error to the literature value is 2 %, while it is 4 % to the measurement performed with a falling ball viscometer. For ethanol, with a measured viscosity of 1.19 ± 0.07, the relative error is higher: the relative error to the literature value is 12 % and it is 4 % to the falling ball viscometer. The ethanol 95% was purchased by Sigma Aldrich, but impurities might be present in the liquid. A slightly different composition of the purchased ethanol might change its viscosity. In fact, the measurement of the viscosity of ethanol performed with the falling ball viscometer has a lower relative error (in agreement with the error found for all the other liquids) with the measurement done with the acoustic method. This supports the hypothesis that the purchased ethanol has a different composition (due to impurities, moisture or different percentage of methanol and 2-propanol) that the one found in literature.

A comparison between the viscosity for all the liquids measured by the SH0-wave technique versus the viscosity obtained with the falling ball viscometer is presented in Figure 4.13b. Table 4.6 shows that the results obtained with the waveguide viscometer are slightly higher than the viscosity obtained with the falling ball viscometer. The viscosity measured with the ultrasonic setup corresponds better to the literature data than to the falling ball viscometer. Only the experimental viscosity of ethanol is significantly higher than the theoretical viscosity obtained from the literature and more measurements need to be done on ethanol to see if this is systematically the case.

4.4.3. INFLUENCE OF THE FREQUENCY ON THE VISCOSITY

For the three mixtures of water and glycerol, the attenuation was measured at several frequencies between 2.4 and 3.6 MHz. For Newtonian fluids, the measured viscosity should be independent of the applied transducer frequency [40]. However, measurements at different frequencies were performed to increase the accuracy of the result by averaging. The attenuation measured experimentally for the three mixtures at different frequencies is shown in figure 4.12a. The predicted curve for each liquid is calculated by using the viscosity published by Cheng [38]. According to Equation 4.1, the attenuation follows a square root dependency on the frequency of the waves. Both the attenuation and viscosity displayed in Figure 4.12 are found by taking the mean viscosity from three measurements at each frequency. The attenuation follows a square root dependence on the

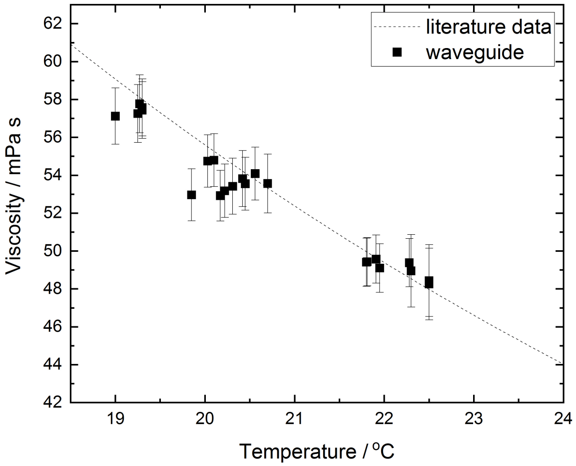

Figure 4.11: The viscosity of the 25/75 volume% water/glycerol mixture measured with the ultrasonic viscometer ■ as a function of the liquid temperature, compared to the literature data by Cheng [38] (dashed line).

frequency of the waves as the predicted curve fits the attenuation measurements. The temperature during the measurements was between 21.8 and 22.4 ±0.2°C. The results can be found in Table 4.5 and 4.6. For the water/glycerol mixtures measured at different frequencies, the measured viscosity is within 5% of the literature data and within 9% of the falling ball viscometer.

Table 4.5: Attenuation α measured with SH0 waves for each liquid at a certain temperature and frequency or range of frequency.

liquid	T °C	f MHz	α np/m
water	26.3 ± 0.1	3.0	0.587 ± 0.009
Ethanol 95 %	26.2 ± 0.1	3.0	0.638 ± 0.018
Wat/Gly 40/60 vol %	22.1 ± 0.1	3.0	2.576 ± 0.024
Wat/Gly 30/70 vol %	21.7 ± 0.1	3.0	3.775 ± 0.026
Wat/Gly 25/75 vol %	19.3 ± 0.1	3.0	5.624 ± 0.011
Measurements varying the frequency			
Wat/Gly 40/60 vol %	22.1 ± 0.1	[2.6; 3.6]	-
Wat/Gly 30/70 vol %	21.8 ± 0.2	[2.6; 3.6]	-
Wat/Gly 25/75 vol %	22.4 ± 0.1	[2.6; 3.6]	-

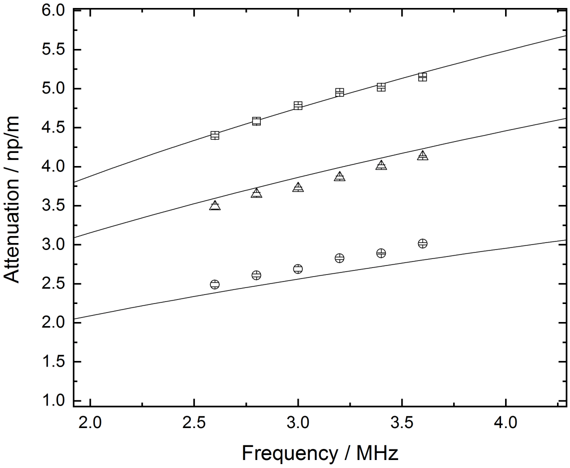

(a)

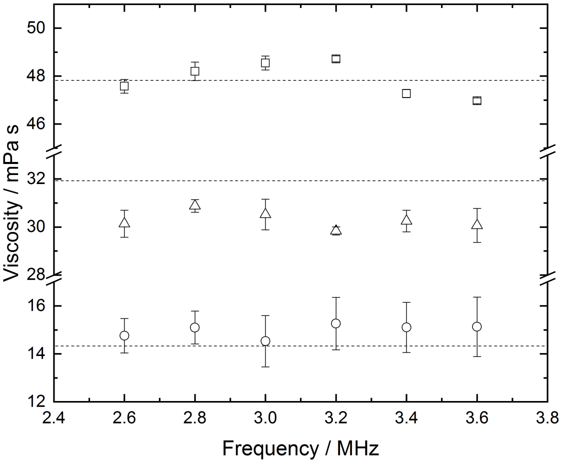

(b)

Figure 4.12: The measured attenuation of the mixtures water/glycerol as a function of frequency (a) is used in order to retrieve the viscosity of the liquid. The liquid viscosity(b) for the water/glycerol mixtures from the ultrasonic measurement (○ 40/60 vol %, △ 30/70 vol %, □ 25/75 vol %) are compared to the reference values. For both the attenuation and the viscosity, the values by Cheng [38] (dashed lines) are used as reference.

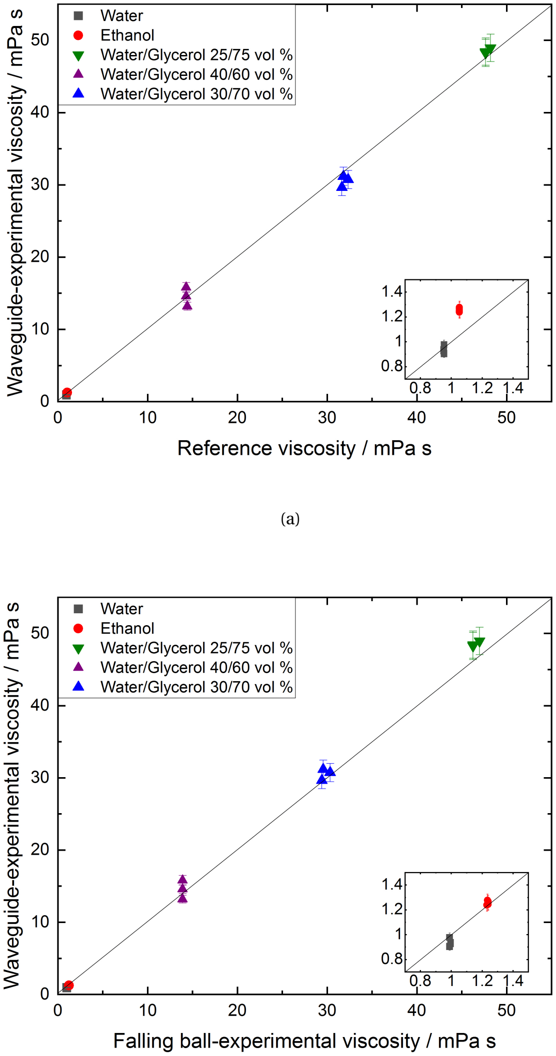

(a)

(b)

Figure 4.13: The viscosity from the shear guided waves attenuation for all the liquids measured is compared to the theoretical viscosity (a) and to the results from the falling ball viscometer (b) for the liquids at the same temperature. The error bars indicate the uncertainty of the method calculated as in section 4.3.3.

Table 4.6: Viscosity μ calculated from the attenuation measured with SH0 waves. These results are compared with the viscosity obtained from literature and measured in this work with a commercial falling ball viscometer.

liquid	μ mPa·s This work	lit. μ mPa·s Literature	Ref	E_R to lit. %	μ^b mPa·s Falling ball	E_R^b %
water	0.881 ± 0.039	0.8633	[41]	2.0	0.840	4.0
Ethanol 95 %	1.193 ± 0.066	1.053	[42]	11.7	1.235	3.5
Wat/Gly 40/60 vol %	14.530 ± 1.069	14.328	[38, 39]	1.4	13.885	4.4
Wat/Gly 30/70 vol %	31.049 ± 0.637	31.929	[38, 39]	2.8	29.767	4.1
Wat/Gly 25/75 vol %	57.430 ± 0.230	57.880	[38, 39]	0.78	55.82	2.9
Measurements varying the frequency						
Wat/Gly 40/60 vol %	14.980 ± 1.030	14.328	[38, 39]	1.4	13.885	4.4
Wat/Gly 30/70 vol %	30.26 ± 0.610	31.929	[38, 39]	2.8	29.767	4.1
Wat/Gly 25/75 vol %	48.549 ± 0.295	47.827	[38, 39]	1.5	46.493	4.2

[b] These values were obtained with the falling ball viscometer.

4.4.4. INFLUENCE OF THE PLATE DIMENSIONS AND MATERIAL ON THE VISCOSITY DETERMINATION

Different plates are used in this research, and their properties are shown in Table 4.2. The influence of the size of the plate is investigated with three stainless steel plates of different sizes. The viscosity of water and of the water/glycerol mixture (25-75 vol%) was measured with each one of the plates. It was taken in consideration that the plate needs to be at least as wide as the transducer (13 mm) to transfer the full waves from the wave generator into the plate. The plate also needs to be clamped to the setup as shown in Figure 4.5. This is done on the top of the plate next to the transducer on both sides. The waves only travel through the central region of the plate, so it is not necessary to make the plate very wide. A plate of 20 mm would, in theory, have enough space to be clamped next to the transducer and transfer the waves without interference. In the current setup, the smallest width of the plate that can be clamped into the setup is 40 mm. To ensure that this is sufficient, two other plates with a width of 60, and 80 mm are also investigated. The width of the plate needs to be minimized to minimize the liquid volume, which is one of our requirements as mentioned in the introduction part of this chapter 4.1. All three plates give good results (within 7 %) in the viscosity measurements, as seen in Figures 4.14a and 4.14b.

Figure 4.14a shows the results of the viscosity of the water/glycerol mixture (25-75 vol%), for the three plates, as function of the liquid temperature. The results are compared to the literature values by Cheng [38] shown as a dashed line in the plot. For each plate, the results are in agreement with the literature values with a maximum relative error of 6%. From Figure 4.14a, it can be observed that the results obtained with the smallest plate (the one with width of 40 mm) are the most accurate (within 2%), and the results obtained with the plate with width of 60 mm are the least accurate, with relative error of 6%. Unfortunately, these measurements were done at the end of the experimental research when all the other measurements (dependence of the attenuation on the viscosity, temperature and frequency) were already performed with the bigger plate, with width of 80 mm. These measurements could not be repeated to check the effective higher accuracy on all the experiments in this work.

Figure 4.14b shows the results of the viscosity of water measured with the three stainless steel plates. The results are compared to the literature values [41] for water. For water, the results obtained with the three plates have a relative error within 9%, except for a single measurement with the plate with width of 80 mm that has a relative error of 19 %. In this case, the results obtained with the smallest plate have high relative error and the ones with the plate with width of 60 mm are the ones with smallest relative error. This shows that these measurements have to be repeated to check their repeatability. However, with these preliminary results we can predict that the viscosity can be measured with smaller plates.

The tungsten plate is also used as it has a much higher melting temperature than stainless steel and can withstand the corrosion by the molten salt. The viscosity of water measured with the tungsten waveguide is shown in Figure 4.15 and is compared to the literature values at the same temperature. In this case, the measured viscosity has a relative error up to 43 % with respect to the literature values. The reason of this difference might be found in the small thickness, 0.108 mm, of the tungsten plate. The intensity of the reflected waves in the tungsten plate was lower of almost 50 mV respect to the one in stainless steel plates due to its smaller thickness, as explained in section 4.3.1, leading to a small S/N ratio. Moreover, the contact area between the plate and the transducer was smaller than with the stainless steel plates, which leads to a lower signal intensity. A thicker plate of tungsten is therefore recommended in future tests to obtain higher accuracy.

4.4.5. INFLUENCE OF THE VOLUME OF THE LIQUID AND THE DIMENSION OF THE CONTAINER ON THE VISCOSITY

The height of the container determines the maximum immersion depth of the plate. A large immersion depth gives more accurate results because it is possible to obtain data with larger attenuation. A large difference along the propagation direction attenuates more the waves. Here, a trade-off has to be made between choosing an as small as possible volume, necessary to measure the small available amount of molten salt, and an as large as possible immersion depth to obtain more accurate results. In Figure 4.16, the error in the measured viscosity as a function of difference in immersion depth between the first and the last measurement point is shown for the different liquids. Each signal was collected increasing the immersion depth of the waveguide constantly by steps of 4 mm in order to have a significant attenuation. In a small volume and therefore with a small immersion depth, only few signals were recorded with a significant attenuation (i.e. 2 measurements for an immersion depth of 10 mm). Figure 4.16 shows how increasing the immersion depth and increasing the measurements collected (12 for the maximum immersion depth of 50 mm in this setup), the error diminishes.

The error for water is larger than the error for the water/glycerol mixtures. This is due to the lower attenuation of the waves in water and, thus, the lower signal to noise ratio.

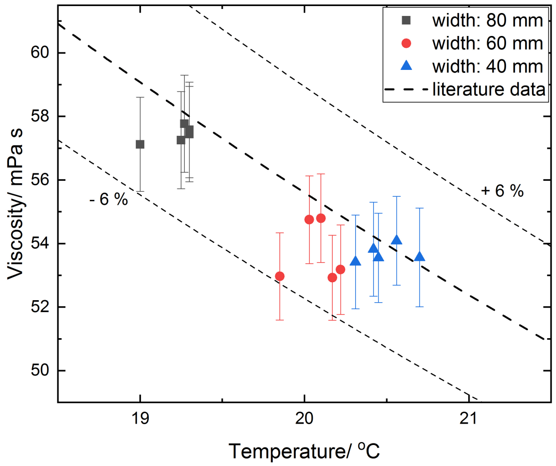

(a)

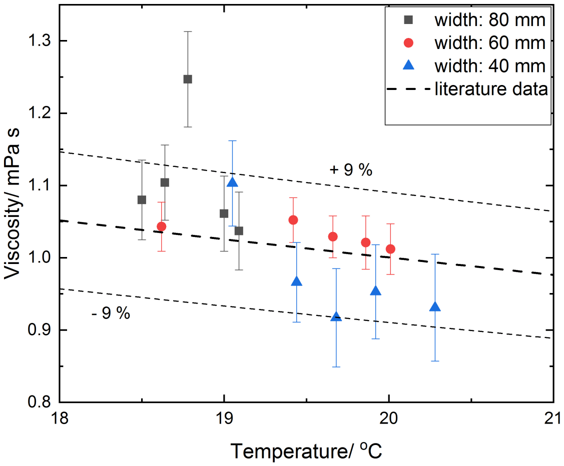

(b)

Figure 4.14: Viscosity of the mixture water/glycerol 25-75 vol % (a) and of water (b) measured with the three different plates. The literature data from Cheng [38] are used as comparison for the water/glycerol mixture, while the literature data from an online engineering toolbox [41] are used as a comparison for the water results.

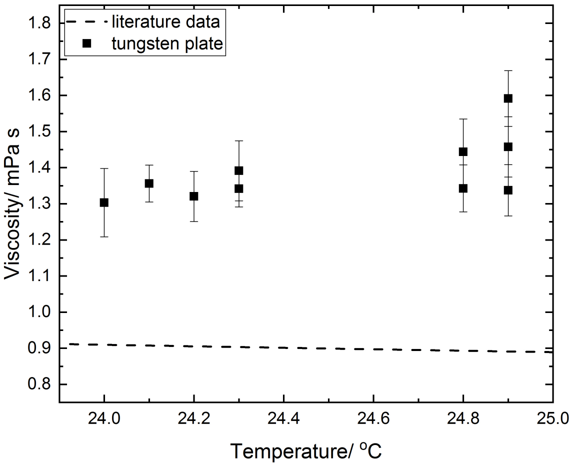

Figure 4.15: Viscosity of water measured with the tungsten plate and obtained from literature data [41]. An overestimation of 15% was found in this case in the experimental values due to the fluctuations of the signals.

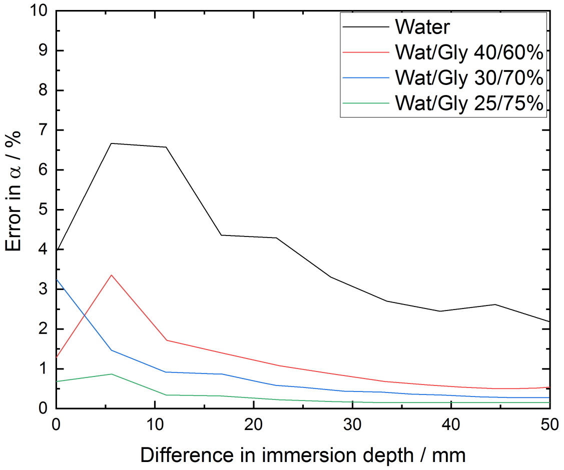

Figure 4.16: Relative error in the viscosity as a function of the difference in immersion depth between two measurement point for different liquids.

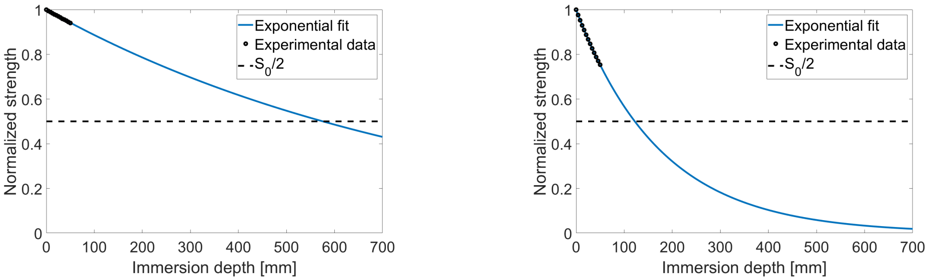

(a) Water

(b) Water/glycerol 40/60 volume%

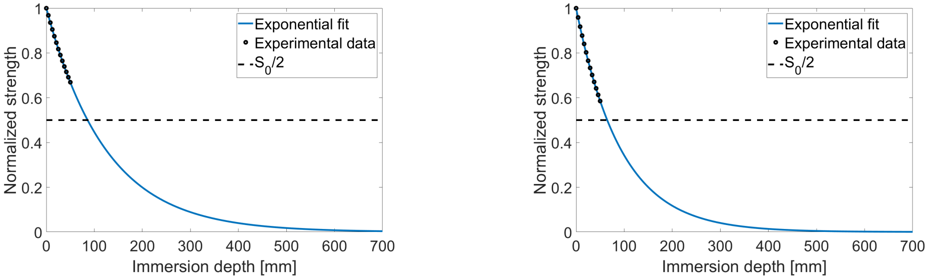

(c) Water/glycerol 30/70 volume%

(d) Water/glycerol 25/75 volume%

Figure 4.17: Normalized signal strength of the wave signal as a function of immersion depth in water (a), water/glycerol 40/60 volume % (b), water/glycerol 30/70 volume % (c), water/glycerol 25/75 volume % (d) fitted with an exponential fit.

For water, the error in the attenuation is above 2% for the maximum difference in immersion depth between the first and the last measurement point. For the water/glycerol mixtures, the error in the attenuation is lower than 0.5% for this maximum difference in immersion depth.

Since the attenuation of the water is much smaller than the attenuation of the water/glycerol mixtures, it should also be considered that only a small part of the exponential decay is visible in the measurements on water. In figure 4.17, the experimental data of the different liquids are plotted with the exponential fit extended. It can be seen that, in this work, the attenuation in an experiment with water only covers a small part of the exponential decay of the intensity of the waves. For the water/glycerol mixtures, however, the intensity of the waves decreases between 20 and 40%, depending on the mixture ratio. Therefore, the exponential fit is more accurate and so is the viscosity measurement. For increasing the accuracy in the water measurements, the liquid container should be made higher.For the water/glycerol mixtures, the height of the container can be made smaller to reduce the amount of fluid used.

With regards to the other dimension: the maximum width of the liquid container is limited by the geometry of the setup and is about 100 mm for the current setup. The minimum width of the container is limited by the width of the plate. Therefore, in the current setup the minimum width of the container should be 41 mm, being the smallest plate 40 mm in width. If a plate of only 20 mm could be fitted in the setup, the width of

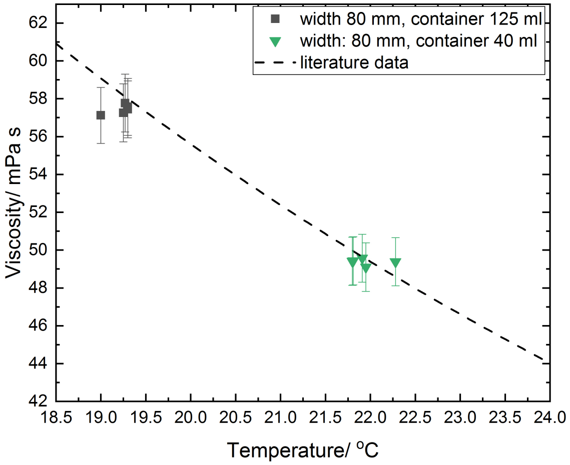

(a)

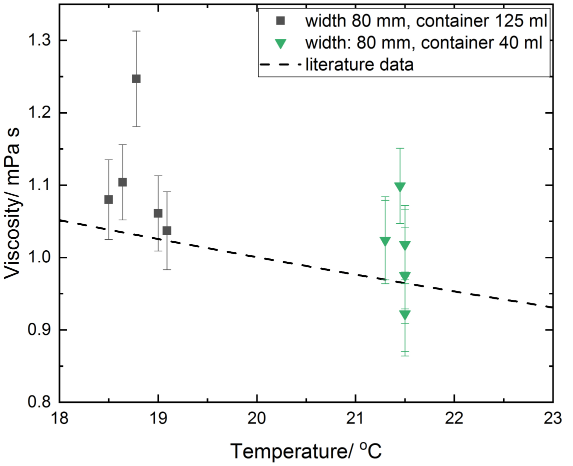

(b)

Figure 4.18: Viscosity of the mixture water/glycerol 25-75 vol % (a) and of water (b) measured in two containers. The data points colored in grey are relative to the measurements in the bigger container (volume of 125 ml), while the green data points are relative to the 40 ml container. The literature data from Cheng [38] are used as comparison for the water/glycerol mixture, while the literature data from an online engineering toolbox [41] are used as a comparison for the water results.

the container can be brought down to about 21 mm.

The depth of the container can be very small, being in the order of magnitude of the thickness of the plate (μm). The viscous layer, responsible for the attenuating effect, is, in fact, extremely small (in the order of μm).

However, a small depth of the container might lead to some practical problems. First of all, the plate needs to be perfectly straight, otherwise it could touch the sides of the container. Another problem is that the liquid level in such a thin container is not perfectly flat. At the walls of a very thin container the liquid may creep up by the capillary effect, resulting in irregular liquid heights. In this work, the thinnest container investigated has a width of about 5 mm, as reported in Table 4.3. With all the used containers, good results were obtained as is shown in Figure 4.18. The results obtained with the smallest container filled with the water/glycerol mixture 25/75 vol %, in Figure 4.18a, agree well with the literature data and are comparable in relative error and standard deviation to the results obtained with the bigger container. The results for water obtained with the small container are shown in Figure 4.18b. In this case the results are more scattered and deviate from the literature value. The results are, however, comparable to the ones obtained with the bigger container. This indicates that the thickness of the container does not need to be more than 5 mm. The thickness of the container might be smaller, with the consideration previously done for avoiding the creeping of the liquid, but this was not yet tested in this work. The liquid volume needed to measure the viscosity of a liquid can be approximately calculated using these suppositions. Practically, an estimate can be made of a container with not more of 10 ml, being the usual maximum available amount of fluid. Thus, the container can be of dimensions lx w x h = 30 x 5 x 70 mm. This makes the method valid for measuring the viscosity of the radioactive molten salt, using a small amount of radioactive fluid.

4.4.6. VISCOSITY MEASUREMENTS UP TO 100°C

The development of the higher temperature setup resulted in new challenges. First, when the liquid is heated, a temperature profile is present in the plate above the liquid [43]. The transducer on top of the plate can not operate at temperatures higher than 50°C. Therefore, the waveguide should allow the decreasing of the temperature from the hot liquid (at maximum 75°C in this work) to less than 50°C on the top of the plate. The temperature profile in the plate may also affect the waves in the plate. A temperature gradient makes the properties of the plate, as density and shear modulus, differ throughout the plate. The intensity of the wave signal, a function of density and shear modulus, will also be different when the temperature profile is different between two immersion depths. For example, if the shear modulus increases, the intensity of the signal decrease because the material opposes the motion of its particle more strongly. The influence of the temperature profile was not investigated in this work, but it has to be studied in future research. A second challenge to account for measurements at higher temperature is that the liquid can more easily evaporate and condensate on the plate, modifying the viscous layer on which the method is based.

Pure glycerol has been measured with the heating setup in a temperature range between 30 and 70°C. The same glycerol, with a purity of more than 99.7%, has been measured with the falling ball viscometer to compare the results. With the falling ball viscometer, the viscosity of the glycerol could only be measured up to 50°C, as this is the limit of the thermometer in the setup. Two different balls (type 3 and 4 in [29]) were used to cover the range of viscosity in the investigated temperature range. In Figure 6.2, the waveguide results, the falling ball results, and literature data are plotted. The experimental results obtained with the waveguide setup are close to the literature data. The measured viscosity at the different temperatures are within 15% from the literature data. It should be noted that the temperature profile is changing in the container when the temperature is increased. Changing the temperature, some time should be waited until the temperature is stabilized. After stabilization, approximately ten minutes, a temperature gradient was found in the first cm below the surface of the liquid. By dipping a thermocouple lower in the liquid it was confirmed that the liquid in the container has a constant temperature. At each step in the temperature, we waited ten minutes to stabilize the temperature of the liquid, but since the container is open, the temperature at the top of the container is lower. The difference between the top and the bottom in temperature was 1°C. This means that the measurements at high temperatures may not represent the viscosity at the measured temperature, but at a slightly lower value.

The current results indicate that the ultrasonic waveguide viscometer can be used to calculate the viscosity of liquids above 55 mPa·s at temperatures up to 70°C within 15%. For a better accuracy, the liquid has to be better insulated to obtain a smaller gradient in temperature in the container, or the setup could be adjusted to fit in a container with a greater height so the amount of immersed liquid at a constant temperature becomes larger.

The results from the falling ball viscometer are, however, not corresponding to the literature data and the results of the waveguide viscometer. Furthermore, when other balls are used, with different properties, the viscosity significantly changes. The source of error for the falling ball viscometer has to be further studied in order to be able to compare results from the ultrasonic viscometer for liquids with no literature data at high temperature.

4.5. CONCLUSIONS

The technique based on ultrasonic wave propagation for deriving the viscosity of liquids is a promising technique for measuring a wide range of low viscosity liquids between 0.8 and 50 mPa·s. The shear horizontal mode (SH0) was used to measure the dynamic viscosity of Newtonian liquids at room temperature. The experimental results compare quite well to literature values with a relative error within 3 % except for ethanol that showed results off by 11.7% . The results by the ultrasonic viscometer were also compared to the results by a commercial falling ball viscometer. In this last case the relative error was slightly more significant, but still less than 5 % for all the liquids. The ultrasonic viscometer showed the capability of measuring small variations of viscosity for liquids with low viscosity, as for the measurements of the water/glycerol varying the glycerol content and the temperature. The viscosity of the water/glycerol mixtures was measured at different frequencies ranging between 2.6 and 3.6 MHz. The results showed, as expected, that the viscosity of the mixtures is independent of the wave frequency.

Also in this study, the sensitivity of the ultrasonic method with respect to the dimension of the plate and the container, and the temperature of the liquid was investigated.

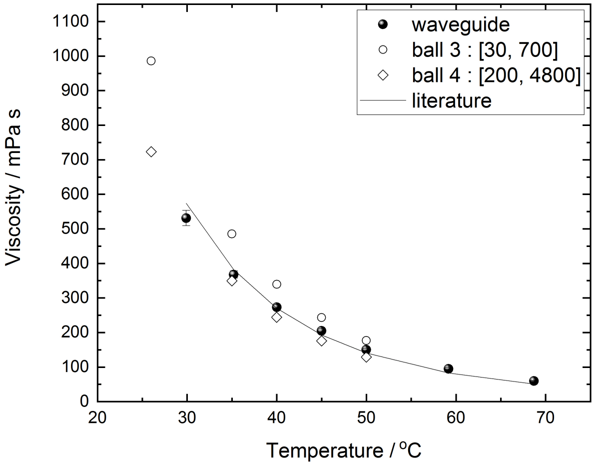

Figure 4.19: Viscosity of pure glycerol measured with the waveguide and with the falling ball viscometer using two different balls (3 and 4) with a different viscosity range of operation compared to literature data [38].

The viscosity was not influenced by the width. The results of the plates with width 40, 60 and 80 mm, were all in good agreement with the literature. The waves only travel through the middle of the plate, so making the plate wider than practically necessary (wider than the transducer) does not contribute to the accuracy of viscosity measurements. Varying the thickness, 0.1 mm. instead of 0.2 mm, and the material of the plate, tungsten instead than stainless steel, the results were not in agreement with the literature. A plate too thin causes more fluctuations in the signal. More measurements have to be performed with a thicker plate of tungsten or a thinner plate of stainless steel to understand the origin of the error.

One of the goals of the research was to minimize the liquid volume needed for the measurement of the viscosity. The smallest volume used in this work is 44 ml, which gave viscosity results corresponding to literature data. Even smaller containers could be used in the setup, and by adjusting the setup using less wide plates, the volume could be decreased to 10 ml. In future research, a liquid container with only 10 ml could be used to see if this still gives viscosity results in agreement with the literature data.

The viscosity of pure glycerol was obtained within 8% of literature data up to temperatures of 70°C. In future research, the heated liquid has to be isolated better, or the container has to be made larger to get more accurate results. Other liquids with lower viscosity have to be tested.

Finally, this work shows that this type of viscosity measurement is suitable for liquids with low viscosity in a harsh environment, where the electronic parts should be kept apart from the liquid. Future applications of this ultrasonic viscometer will address the possibility of performing measurements at higher temperatures. The possibility to measure non-Newtonian fluids will also be considered. The use of a smaller waveguide will also be studied in order to reduce the amount of liquid necessary for the measurements even further. This method has many advantages for high temperatures, high corrosion and high radioactivity liquids.

4.6. APPENDIX A

In this appendix the attenuation caused by viscous losses will be derived. For a cross section of a plate waveguide it can be expressed by use of the average power flow:

$$\alpha = \frac{\frac{\partial P}{\partial z}}{2P_{area}}, \tag{4.10}$$

Where, considering z as the propagation direction, $\frac{\partial P}{\partial z}$ describes the power lost across the boundary of the waveguide and P_{area} is the total average power flow across the cross section of the waveguide. We assume, for simplicity, that the fluid is Newtonian. This means that its shear relaxation time, the time that it takes for material to not feel the stress of a certain strain anymore, is less than $\frac{1}{\omega}$. With this assumption, the viscous skin depth, the width of the layer in which the liquid has a viscous dissipation effect on the ultrasonic waves, is defined as:

$$\delta = \left(\frac{2\eta}{\rho_f \omega}\right)^{1/2}, \tag{4.11}$$

where η is the liquid viscosity, η_f is the liquid density and ω is the angular frequency. Therefore an expression for the velocity in the liquid adjacent to the waveguide can be expressed as

$$v = v_0 e^{-y/\delta}0 \tag{4.12}$$

where v_0 denotes the surface velocity of the waveguide and y denotes the distance from the surface in the liquid. The quantity $\frac{\partial P}{\partial z}$, the change in average power flow due to the viscous effect of the liquid, is the power leaving the waveguide cross section. Therefore it is the dissipated power over a unit surface area, $1/2\tau_0 v_0$, where τ_0 is the viscous drag on the plate:

$$\tau_0 = \eta \frac{\partial v}{\partial y} = -\eta . \frac{v_0}{\delta} \tag{4.13}$$

The change in average power flow This quantity can be found then by integrating the power flow per unit width of the plate across the top and bottom surfaces of the plate

$$\frac{\partial P}{\partial z} = 2 \int_0^1 \frac{1}{2} \tau_0 v_0 dx \tag{4.14}$$

Where the factor of two before the integral comes from the two surfaces along which power is dissipated into the liquid.

Rearranging Equation 4.14, $\frac{\partial P}{\partial z}$ becomes:

$$\frac{\partial P}{\partial z} = -v_0^2 \left(\frac{\rho_f \omega \eta}{2}\right)^{1/2}. \tag{4.15}$$

The second quantity that has to be evaluated to find the guided wave attenuation is the term P_{area}, the average power flow across the cross section of the plate of thickness h.

P_{area} can be found using the Poynting vector, that represents the power flow across an area:

$$P_{area} = \int_0^1 \int_0^h \frac{-v^* \sigma}{2} dy dx \tag{4.16}$$

where v^* is the complex conjugate of the velocity and σ the stress at any point within the cross section. The velocity and stress field variation can be described using the displacement distribution for the SH mode (Rose, 1999). For the SH modes, the particle displacement vectors have only one component, that means, $u_y(y,t) = u_z(z,t)$. The particle displacement vector along the x direction is:

$$u_x = B e^{i(kz-\omega t)} \tag{4.17}$$

where B is an arbitrary wave amplitude, k is the wavenumber of the mode ($k = \frac{\omega}{c} = \frac{2\pi}{\lambda}$), where c and λ are respectively the sound velocity and wavelength of SH waves is the liquid. The velocity and stress field variation can be then derived as:

$$v_x = \frac{du_x}{dt} = -i\omega B e^{i(kz-\omega t)} \tag{4.18a}$$

$$\sigma_x = G\frac{du_x}{dt} = -ikBGe^{i(kz-\omega t)} \tag{4.18b}$$

Where the stress field depends on G, the shear modulus of the plate. Hence,

$$P_{area} = \int_0^1 \int_0^h \frac{\omega k B^2 G}{2} dy dx \tag{4.19}$$

and using the identities $k = \frac{\omega}{c}$ and $c = \left(\frac{G}{\rho_s}\right)^{1/2}$, with ρ_s the density of the plate, yields

$$P_{area} = -\frac{1}{2}\omega^2 B^2 \left(G\rho_s\right)^{1/2} h \tag{4.20}$$

Now, substituting the expression $v_0 = -i\omega B$ for the velocity at the interface into the $\frac{\partial P}{\partial z}$ term obtained earlier yields the guided wave attenuation:

$$\alpha = \frac{\frac{\partial P}{\partial z}}{2P_{area}} = \frac{-v_0^2\left(\rho_f \omega \eta/2\right)^{1/2}}{-\omega^2 B^2 \left(G\rho_s\right)^{1/2} h} = \frac{i\omega B^2\left(\rho_f \omega \eta/2\right)^{1/2}}{-\omega^2 B^2 \left(G\rho_s\right)^{1/2} h} \tag{4.21}$$

after rearranging and cancellations,

$$\alpha = -\frac{1}{2h}\left(\frac{2\rho_f \omega \eta}{G\rho_s}\right)^{1/2} \tag{4.22}$$

This formula works well for frequency-plate thickness products up to about 2 MHz mm. The frequency-thickness products used in this work are all below 1 MHz mm and therefore the equation 4.1 was used to measure the attenuation and calculate the viscosity.

4.7. ACKNOWLEDGMENTS

The authors acknowledge Martin Verweij, Paul van Neer and the acoustic group of TUDelft for the private communications and for the borrowing of their instruments and laboratory. SM acknowledge the H2020 SAMOFAR project for funding this project. SM acknowledges Stefano Mastromarino for the drawings of the setup. This project has received funding from the Euratom research and training programme 2014-2018 under grant agreement No 661891.

REFERENCES

[1] K. A. Tasidou, J. Magnusson, T. Munro, and M. J. Assael, *Reference Correlations for the Viscosity of Molten* $LiF-NaF-KF$*,* $LiF-BeF_2$*, and* $Li_2CO_3-Na_2CO_3-K_2CO_3$*,* Journal of Physical and Chemical Reference Data **48**, 043102 (2019).

[2] S. I. Cohen and T. N. Jones, *ORNL-2278, Oak Ridge National Laboratory (ORNL)*, Tech. Rep. (1957).

[3] S. Cantor, W. T. Ward, and C. T. Moynihan, *Viscosity and Density in Molten* BeF_2LiF *Solutions,* The Journal of Chemical Physics **50**, 2874 (1969).

[4] M. Chrenkova, V. Danek, R. Vasiljev, A. Silny, V. Kremenetsky, and E. Polyakov, *Density and viscosity of LiF-NaF-KF-KBF*$_4$*-B*$_2$*O*$_3$ *melts,* Journal of molecular liquids **102**, 213 (2003).

[5] A. Merzlyakov, V. Ignatiev, and S. Abalin, *Viscosity of molten lithium, thorium and beryllium fluorides mixtures,* Journal of Nuclear Materials **419**, 361 (2011).

[6] A. Merzlyakov, V. Ignatiev, and S. Abalin, *Viscosity of LiF-NaF-KF eutectic and effect of cerium trifluoride and uranium tetrafluoride additions,* Nuclear Engineering and Design **278**, 268 (2014).

[7] R. Serrano-López, J. Fradera, and S. Cuesta-López, *Molten salts database for energy applications,* Chemical Engineering & Processing: Process Intensification **73**, 87 (2013).

[8] W. P. Mason, W. O. Baker, H. J. Mcskimin, and J. H. Heiss, *Measurement of shear elasticity and viscosity of liquids at ultrasonic frequencies,* Physical Review **75**, 936 (1949).

[9] T. Stevenson, D. G. Martin, P. I. Cowin, A. Blumeld, A. J. Bell, and T. P. Comyn, *Piezoelectric materials for high temperature transducers and actuators,* Journal of material science **26**, 9256 (2015).

[10] D. L. Hunston, *Determination of the high frequency viscoelastic properties for polymers using shear mode strip delay lines,* Journal of Polymer Science Part A: Polymer Chemistry **35**, 201 (1971).

[11] C. J. Knauss, D. Leppo, and R. R. Myers, *Viscoelastic Measurement of Polybutenes and Low Viscosity Liquids Using Ultrasonic Strip Delay Lines,* Journal of Polymer Science: Symposium , 179 (1973).

[12] V. Shah, K. Balasubramaniam, and P. W. G. Mayer, *Effect of viscosity on ultrasound wave reflection from a solid / liquid interface,* Physics **34**, 817 (1996).

[13] V. Prasad, K. Balasubramaniam, E. Kannan, and K. L. Geisinger, *Viscosity measurements of melts at high temperatures using ultrasonic guided waves,* Journal of Materials Processing Technology **207**, 315 (2008).

[14] V. V. Shah and K. Balasubramaniam, *Measuring Newtonian viscosity from the phase of reflected ultrasonic shear wave,* Ultrasonics **38**, 921 (2000).

[15] T. K. Vogt, M. J. S. Lowe, and P. Cawley, *Measurement of the Material Properties of Viscous Liquids Using Ultrasonic Guided Waves,* IEEE Transactions on Ultrasonics, Ferroelectrics, and Frequency Control **51**, 737 (2004).

[16] F. B. Cegla, P. Cawley, and M. J. S. Lowe, *Material property measurement using the quasi-Scholte modeA waveguide sensor,* The Journal of the Acoustical Society of America **117**, 1098 (2005).

[17] P. B. Nagy and R. M. Kent, *Ultrasonic assessment of Poissons ratio in thin rods,* The Journal of the Acoustical Society of America **98**, 2694 (1995).

[18] M. B. Gitis and V. A. Chuprin, *Application of surface and normal ultrasonic waves for measuring the parameters of technical fluids: I. Shear viscosity measurements,* Technical Physics **57**, 671 (2012).

[19] D. L. Hunston, C. J. Knauss, M. B. Palmer, and R. R. Myers, *Viscoelastic measurements of poly(dimethylsiloxanes) and a polystyrene solution using the layered waveguide technique,* Transactions of the Society of Rheology **16**, 45 (1972).

[20] M. S. Greenwood and J. A. Bamberger, *Measurement of viscosity and shear wave velocity of a liquid or slurry for on-line process control,* Ultrasonics **39**, 623 (2002).

[21] L.-L. WANG, *Chapter 6 - one-dimensional visco-elastic waves and elastic-visco-plastic waves,* in *Foundations of Stress Waves* (Elsevier, Oxford, 2007) pp. 219 – 264.

[22] K. H. Swapan, *Chapter 6 - exploration geophysics,* in *Mineral Exploration (Second Edition)* (Elsevier, 2018) second edition ed., pp. 103 – 122.

[23] T. Vogt, M. J. S. Lowe, and P. Cawley, *Ultrasonic waveguide techniques for the measurement of material properties,* AIP Conference Proceedings **615**, 1742 (2002).

[24] S. Kostek, B. K. Sinha, and A. N. Norris, *Thirdorder elastic constants for an inviscid fluid,* The Journal of the Acoustical Society of America **94**, 3014 (1993).

[25] J. N. Sharma and V. Pathania, *Propagation of leaky surface waves in thermoelastic solids due to inviscid fluid loadings,* Journal of Thermal Stresses **28**, 485519 (2005).

[26] F. B. Cegla, P. Cawley, and M. J. S. Lowe, *Fluid bulk velocity and attenuation measurements in non-Newtonian liquids using a dipstick sensor,* **17**, 264 (2006).

[27] D. E. Holcomb and S. M. Cetinee, *ORNL/TM-2010/156, Oak Ridge National Laboratory (ORNL)*, Tech. Rep. (2010).

[28] Julabo - The temperature control company, *Corio CD heating circulator*, Julabo.

[29] Fungilab Leading Viscosity Technology, *kinematic-viscometers: viscoball*, Fungilab.

[30] F. Hoppler, *Hoppler kugelfall viskosimeter,* (Germany, 1932).

[31] J. H. De Van and R. B. Evans, *ORNL-0328, Oak Ridge National Laboratory (ORNL)*, Tech. Rep. (1962).

[32] K. Sridharan and T. R. Allen, *Molten Salts Chemistry* (Elsevier Inc., 2013) pp. 241–267.

[33] H. Songling, Z. Yu, W. Zheng, W. Shen, and S. Hongyu, *Theory and Methodology of Electromagnetic Ultrasonic Guided Wave Imaging* (Springer, 2019) pp. 31–151.

[34] ASM Handbook Committee, *Properties and Selection: Irons, Steels, and High-Performance Alloys* (ASM International, 1990).

[35] R. C. Weast, M. J. Astle, W. H. Beyer, and J. A. Van Allen, *Handbook of Chemistry and Physics*, 65th ed. (CRC Press, 1986).

[36] N. R. Draper and H. Smith, *Applied Regression Analysis*, 3rd ed. (Hoboken, NJ: Wiley Interscience, 1998).

[37] J. A. Trejo González, M. P. Longinotti, and H. R. Corti, *The viscosity of glycerolwater mixtures including the supercooled region,* Journal of Chemical & Engineering Data **56**, 1397 (2011), https://doi.org/10.1021/je101164q .

[38] N.-S. Cheng, *Formula for the Viscosity of a GlycerolWater Mixture,* Industrial & Engineering Chemistry Research **47**, 3285 (2008).

[39] A. Volk and C. J. Kähler, *Density model for aqueous glycerol solutions,* Experiments in Fluids , 59 (2018).

[40] M. Schirru, X. Li, M. Cadeddu, and R. Dwyer-Joyce, *Development of a shear ultrasonic spectroscopy technique for the evaluation of viscoelastic fluid properties: Theory and experimental validation,* Ultrasonics **94** (2018), 10.1016/j.ultras.2018.07.002.

[41] E. ToolBox, *Engineering ToolBox water - dynamic and kinematic viscosity,* (2004).

[42] E. ToolBox, *Engineering ToolBox ethanol - dynamic and kinematic viscosity,* (2018).

[43] F. B. Cegla, P. Cawley, J. Allin, and J. Davies, *High-temperature (>500řc) wall thickness monitoring using dry-coupled ultrasonic waveguide transducers,* IEEE Transactions on Ultrasonics, Ferroelectrics, and Frequency Control **58**, 156 (2011).

5

DISSOLUTION OF FUEL SALT INTO WATER

For me chemistry represented
an indefinite cloud of future potentialities
which enveloped my life to come in black volutes
torn by fiery flashes, like those which had hidden Mount Sinai.
Like Moses, from that cloud I expected my law,
the principle of order in me, around me, and in the world.

Primo Levi

In this work we present a comprehensive description of the interaction of solid Molten Salt Fast Reactor (MSFR) fuel salt with water. For the salt, the binary systems LiF-ThF$_4$ *and the ternary system LiF-ThF*$_4$*-UF*$_4$ *were analysed. As a preliminary salt, LiF-NaF-KF, which is considered as a coolant for MSFR and which is commonly used as simulant of the fuel salt, was analysed. The three salts have been mixed with water in the ratio of 10 g/l (also 5 g/l for the LiF-ThF*$_4$*-UF*$_4$ *salt) to simulate the scenario of the fuel leakage in water during storage of the salt. The experiments were repeated for different conditions of physical state. To maximize the dissolution process, a part of the fuel salt was ground to powder to increase the contact surface exposed to the aqueous phase. Experiments were performed at a constant temperature of 25řC and 75řC to evaluate the effect of temperature. Furthermore, we studied also the effect of gamma radiation on the salt solubility, performing experiments under irradiation in a Co-source. After dissolution, the concentration of the single fluorides in water was determined by inductively coupled plasma-optical emission spectroscopy. The hydrate compounds formed in these systems have been determined using powder X-ray diffraction, while the possible change of oxidation state of uranium was studied by X-ray absorption spectroscopy. The current results are important for understanding the system behaviour during a hypothetical interaction with water for a long time.*

5.1. INTRODUCTION

Nuclear technology still needs development to support the advancement of nuclear reactors and address public concerns about nuclear energy. In 2000, six types of Generation IV nuclear reactors were proposed. The Molten Salt Fast Reactor (MSFR) is one of these innovative nuclear concepts [1] with the major goals of sustainability, safety and reliability, economic competitiveness and proliferation resistance. The particularity and innovation of the MSFR technology is the use of liquid fuel; a mixture of molten fluoride salts, such as LiF-ThF_4-PuF_3-UF_4, currently being considered as fuel for MSFRs [2].

Liquid fuel has several advantages, especially for reactor safety [3, 4]. In accidental conditions during which the salt overheats, the fluid fuel salt can be automatically drained via freeze plugs into storage tanks under the reactor core. These tanks are designed such that the fuel can be confined for a long period without overheating. In a preliminary design of MSFR, cooling rods are placed in these draining tanks, each consisting of a thick layer of inert salt surrounded by a central channel where cooling water can circulate [5].

Following a hypothetical situation in which molten fuel salt and water come into contact [6], it might be necessary to wait before the radiation levels decrease sufficiently to permit on-site examination and repair [7]. During this time the fuel salt can dissolve in water leading to possible radioactive release. The thermodynamic and chemical reaction between the salt and water have to be understood to ensure the safety of the emergency draining system.

The physical effects of mixing molten fuel salt and water have been studied previously at Oak Ridge National Laboratories [8]. Their study considered the dissolution of a different fuel salt (LiF-UF_4-ThF_4-BeF_2) with respect to the one used for MSFRs.

This paper presents a series of experiments performed to understand the interaction of solid MSFR fuel salt with water. We analysed mixtures of fuel salt-water to simulate the situation of fuel leakage in water. We investigated the dissolution of fuel salt (LiF-ThF_4 and LiF-ThF_4-UF_4) in water, as well as the dissolution of FLiNaK, the ternary eutectic alkaline metal fluoride salt mixture LiF-NaF-KF (46.5-11.5-42 mol %) considered as a secondary coolant for MSFR. The latter experiments served also to optimize the method before handling of actinides.

The experiments were carried out under different conditions of temperature (25řC and 75řC), radiation (γ-irradiation) and sample morphology (powder and fragments) to investigate the influence of these parameters on the salt solubility. The study of the dissolution of MSR fuel salt in water under γ-irradiation was of particular interest because it simulates an environment under irradiation due to the decay of fission products.

After the dissolution experiments, we examined the solvent by chemical analysis. Inductively coupled plasma optical emission spectroscopy (ICP-OES) was employed for detecting chemical elements in the liquid part. X-Ray diffraction (XRD) and X-ray absorption spectroscopy (XAS) were employed to analyse the solid part of the solution after filtration and drying. The possible formation of metal oxide and hydroxide phases was determined by XRD since we found this could influence the dissolution of the salt in water. In fact, the formation of an oxide crust when the salt is in contact with water can prevent the further dissolution of the fluoride salt as well as influence the melting point and the corrosion behaviour of the salt. The water can react with fluoride molten salts to produce highly corrosive HF and metal oxides of much higher melting point [9]. The possible change of oxidation state of uranium to the very soluble hexavalent state was evaluated by XAS. We determined the solubility of the cations at different temperatures to understand the probable course of events in the weeks following the postulated accident. Finally, a complete analysis of the dissolution of the different cations and of the formation of hydrate compounds after chemical reaction will be presented.

5.2. METHOD

5.2.1. SAMPLE PREPARATION

The alkali fluorides used as starting materials were LiF, NaF, KF of 99.99 w% metallic purity purchased from Alfa Aesar. The MSFR fuel samples analysed in this study contained in addition ThF_4 and UF_4 which were synthesised from oxide precursors and purified to analytical grade according to the procedure described in detail in [10]. LiF, NaF, KF were preliminary purified in order to remove residual moisture from the single fluorides, a drying procedure was applied for 4 hours at 400řC under argon flow using the flow rate of 0.5 l/min at 1 bar. The provenance and purity of the starting materials is shown in Table 5.1. All samples were handled inside a dry argon-filled glove-box because of their high sensitivity to water and oxygen. The oxygen and moisture content in this glove-box was constantly monitored and was under 1 mg/kg for oxygen and under 2 mg/kg for water. The purity of the starting end-members was analysed by X-ray diffraction and DSC to check if the end-members were pure/dried at the moment of the synthesis of the salt. Peaks relative to oxides and oxyfluorides were not detected.

Starting from single fluorides, samples with fixed LiF-ThF_4 and LiF-ThF_4-UF_4 molar ratios of nominally 78:22 and 76.2:21.3:2.5 were prepared. The first salt containing only LiF and ThF_4 is the basic eutectic mixture for MSR. The second one containing UF_4 is the composition with the lowest melting point in the pseudo-binary LiF-ThF_4 system with fixed concentration of UF_4 at 2.55 mol% [11], set as proposed concentration of a fissile material in the MSFR [12]. The last salt composition is one of the recommended fuel options for a MSR system containing only the three cations mentioned above. The prepared stoichiometric mixtures were heated for 2 h to a maximum temperature of 1300 K, higher than the highest melting point of the end-members, to completely homogenize the sample. One sample of the salt mixture LiF-ThF_4-UF_4 was left unmolten to compare the results with the one of [8], that examined the salt at the same conditions.

A part of the melted and re-solidified salt was ground to powder. When mixed with water, the ground salt would present a large surface area to the aqueous phase increasing the rate of dissolution. The remaining salt was used as fragments to study the influence of the surface in contact with water. The salt in both forms was mixed with water to simulate an accidental situation of fuel leakage in water or vice-versa. Two procedures were followed at this stage. In the first case, samples of ~10 mg of salt was mixed with ~ 1 ml and 2 ml of water to have respectively initial ratios of ~ 10 and 5 g/l. Several vials containing each the same amount of salt and water were prepared. After time intervals ranging from 1 to 30 days, the water for one of these vials was filtered for chemical analyses while the other vials were left for studying a longer dissolution. In the second case, ~ 100 mg of salt was mixed with ~ 10 ml of water, having again an initial concentration of 10 g/l.

Table 5.1: Provenance and purity of materials used.

Salt	Supplier	Initial Weight Fr. Purity	Purification Method	Analysis Method
LiF	Alfa Aesar	0.999	drying	XRD
KF	Alfa Aesar	0.999	drying	XRD
NaF	Alfa Aesar	0.999	drying	XRD
ThF_4	JRC-Karlsruhe	0.995	HF/drying	XRD/DSC
UF_4	JRC-Karlsruhe	0.995	HF/drying	XRD/DSC

After the same time intervals of the previous procedure, ~ 200 μl of the supernatant water (the clear water overlying the salt deposited by precipitation) was taken each time for the chemical analysis. The collected supernatant water looked transparent and free of particles of salt. All the mixtures studied in this work are summarised in Table 5.2. The water extracted was collected in vials and analysed with ICP-OES while the remaining powder or fragment was dried in the furnace for one hour at the temperature of 100řC for a successive analysis with XRD and XAS.

Table 5.2: Summary of the experiments

Composition	Initial equivalent content of salt in water g/l	Form	Condition
FLiNaK (46.5-11.5-42)	10	powder	25 °C
	10	fragments	25 °C
$LiF\text{-}ThF_4$ (78-22)	10	powder	25 °C
	10	fragments	25 °C
	10	powder	Irradiated at 1kGy, 25 °C
	10	powder	75 °C
$LiF\text{-}ThF_4\text{-}UF_4$ (76.2-21.3-2.55)	10	powder	25 °C
	10	fragments	25 °C
	10	powder	25 °C, from unmolten powder
	10	powder	25 °C[b]
	5	powder	25°C[b]
	10	powder	25 °C, supernatant water[b]
	10	fragments	25 °C, supernatant water[b]
	10	powder	Irradiated at 1kGy, 25 °C
	10	powder	75 °C

[b] These solutions were analysed in JRC-Karslruhe with a Ultima2, HORIBA Jobin Yvon instrument.

5.2.2. CO-60 IRRADIATION FACILITY

The dissolution experiments under irradiation were carried out using a cobalt-60 gamma ray source (Atomic Energy of Canada, 'Gammacell 220') at the RID of TU Delft. The source is illustrated and technically described in [13]. High doses of gamma-radiation can be given to materials to be investigated; about 1 kGy per hour. Such doses can be used to investigate the effect of radiation on dissolution of molten salt in water. The mixture of water and salt was placed in a stainless steel crucible tightly closed in order to avoid any leakage of material. The crucible was approximately 1 cm in diameter and 2 cm in height. The crucible was centrally placed in the sample chamber of the source prior to being mechanically lowered into the irradiation zone of the Co-60 source. Inside, the gamma radiation field is homogeneous due to the positioning of multiple Co-60 sources surrounding the sample chamber.

5.2.3. INDUCTIVELY COUPLED PLASMA-OPTICAL EMISSION SPECTROSCOPY

Elemental concentrations in solution were analysed by inductively coupled plasma-optical emission spectroscopy (ICP-OES). This is an analytical technique that can be used to determine trace of ions in a solution by using inductively coupled plasma source, made by ionizing argon gas. The plasma source dissociates the sample into its constituent atoms or ions, exciting them to a level where they emit light of a characteristic wavelength.

Two instruments were used in this work. The first one is a Perkin Elmer Optima 4300 DV purged with nitrogen installed at the Reactor Institute Delft at TU Delft. The second one is a High Resolution ICP-OES instrument (Ultima2, HORIBA Jobin Yvon, Longjumeau, France) installed at JRC-Karlsruhe. In this second instrument, the R446 photomultiplier (Hamamatsu Photonics, Shimokanzo, Japan) was replaced by a more sensitive, multialkali photocathode (R955, Hamamatsu Photonics) and the sample introduction system and the torch plasma have been installed in a glove-box. This adaptation of the original ICP-OES setup was done in order to guarantee protection against α and β radiation of the investigated radioactive sample solutions. Same experiments were repeated with the two instruments in order to address the match between the two instruments.

All solutions and samples were prepared gravimetrically. The samples were acidified with 0.81 M nitric acid to ensure that the elemental components remained in solution [14, 15]. The solutions were prepared from high purity water (18.2 MΩ cm) from a MilliQ Element (Millipore) water purification system and Suprapur Nitric Acid 65% [16]. For the analysis, the aliquots of samples from the dissolution mixture were diluted to 10 ml with high purity water.

Measurements were carried out in duplicate and repeated on two different days. The relative standard deviation (RSD) of the within-day repeatability typically varied between 0.8% and 1.6%. The between-day variability fluctuated between 0.5% and 2.8%.

The instruments were calibrated for the cations using the ICP-OES single element standard solutions containing 1000 mg/kg of each lithium, sodium, potassium, thorium, uranium (Plasma standard solution, Specpure, Alfa Aesar). These were suitably diluted to obtain standard solutions with concentration of 0, 0.2, 0.4, 0.6, 0.8, 1 mg/Kg, within the detection limit for all analytes.

5.2.4. XRD analysis

The possible formation of oxide or hydroxide was analysed by X-Ray diffraction (XRD). A PANalytical XPert PRO X-ray Diffraction System mounted in a BraggBrentano configuration with a Cu K-alpha monochromator, a copper tube (40 kV, 40 mA), and a X Celerator fast detection system was used to measure the diffractograms. For the measurement, the ground powders were deposited on a silicon wafer to minimize the background. An air-tight sample holder with a Kapton window was designed to measure the radioactive and very hygroscopic sample with the X-Ray diffractometer. The sample holder was closed in an Ar glove-box to ensure the sample purity during the measurement as well as to avoid contamination. The studied materials must indeed be contained to ensure that no radioactive contamination is released during the preparation of the specimen as well as to preserve the quality of the sample during the measurement. The data were collected by step scanning in the angle range 10ř ≤ 2θ ≤ 120ř over a period of about 8 h. Structural analysis was performed with the Fullprof2k suite software [17] by Le Bail method [18].

5.2.5. X-ray absorption spectroscopy

X-ray Absorption Near Edge Structure (XANES) and Extended X-ray Absorption Fine Structure (EXAFS) measurements were performed at the Dutch-Belgian Beamline (DUBBLE, Beamline 26) of the European Synchrotron Radiation facility (ESRF, Grenoble) [19]. Only XANES results are presented in this work since the interest for this work was only in studying the valence state of the cations. Measurements were performed on small amounts (less than 10 mg) of powdered samples mixed with boron nitride (BN) and pressed into pellets. XANES spectra were collected at room temperature in the transmission mode at the U L_{III} edge. Energy calibration was achieved by measuring the K XANES spectrum of a Y reference foil (17038 eV) before and after the sample measurement. The XANES spectra have been normalized using linear functions for pre- and post-edge modelling. The white-line maxima have been taken as the first zero-crossing of the first derivative. The pre-edge removal and normalization correction were performed using the ATHENA software[20].

5.3. Results

5.3.1. Dissolution of FLiNaK in water

As described in section 5.2.1, ten vials containing each one 1 ml of water and 10 mg of FLiNaK (half of the vials contained powdered FLiNaK and half as fragments) were analysed. After mixing the FLiNaK salt with water, the mixtures were maintained at room temperature during the dissolution. The elemental concentrations of potassium, sodium and lithium released from the FLiNaK salt into water are shown in Figure 5.1. The concentration of the three ions released from the powdered salt is similar to that of the ions released from the salt left as fragments, although the dissolution rate was expected to be higher in the first case due to the larger contact area of the salt with water. We believe that the reason for this similar dissolution of powder and fragments in water is that the equilibrium of the dissolved ions was established faster than the minimum time of one day in which we performed the analysis.

The XRD pattern of FLiNaK demonstrated that it consisted of LiF, NaF and KF and no new compound was formed as shown also by An et al. [21]. This means that in solution most ions are in a free state and their concentration in water depends only on the solubility of the ions itself and on their molar fraction in the salt. Comparing in Figure 5.1 the concentration in water of the three cations, it is clear that potassium in Figure 5.1a has a higher concentration in water due to its higher solubility [22] and its high molar fraction (42 mol %) in the composition. Even if LiF is the most present fluoride in the composition (46.5 mol %), its solubility in water is much lower than the one of KF [23] and this is confirmed in Figure 5.1b by the low amount of lithium released in water from FLiNaK. The concentration of lithium in water was 3 times lower than that of potassium. NaF has a solubility 20 times higher than the one of LiF [24] , but due to its small molar fraction in the FLiNaK salt (11.5 mol %), the concentration of sodium, shown in Figure 5.1c, and lithium are comparable. It can be observed from the concentration curves of the three cations that the concentration of lithium has a completely different trend than the other two cations, i.e. very high concentration at the beginning and a sharp decrease between 1 and 7 days.

5.3.2. DISSOLUTION OF LIF-THF$_4$ IN WATER

Eight vials containing LiF-ThF$_4$ in the proportion 78-28 mol% were prepared. Five of them contained the salt ground to powder mixed with water with an initial concentration of 10 g/l. The other three contained water and salt in the same concentration of 10 g/l but the salt was left as a single fragment of 10 mg for each vial. Figure 5.2 shows the concentration of the two cations, lithium and thorium in water. The solubility of lithium fluoride is higher than the one of thorium [23, 25] and this is also reflected by our results where we measured a much smaller concentration of thorium in water. At the temperature of 25 ř C, the concentration of lithium rose constantly during three weeks. After 30 days the concentration of lithium diminished again.

Figure 5.2a shows that the fragments that were not powdered dissolved less lithium in water most likely due to the smaller contact area. In this case the effect is higher than for the FLiNaK salt dissolved in water. Within the exposed time period, lithium as powder dissolved 2-3 times faster than from fragments. Comparing Figure 5.2a with Figure 5.1b, it is also noticeable that the lithium was initially more concentrated in water when FLiNaK was dissolved in water. LiF-ThF$_4$ in the proportion 78-28 mol% form Li$_3$ThF$_7$, while FLiNaK does not form a new compound after melting and successive crystallization. We believe that it is the formation of the intermediate compound that is responsible for the lower dissolution.

Figure 5.2b shows the concentration of thorium in water from the salt. This cation has a very low concentration in water and in some cases (i.e. the solutions left dissolving for 2 and 3 weeks) the cation was not detectable by the spectrophotometer. The error is also very high in these measurements due to the low concentration of the cation, which is difficult to detect.

Also with LiF-ThF$_4$ in water, we noticed that the salt grounded to powder indicated higher dissolution rate compared to the salt in fragments.

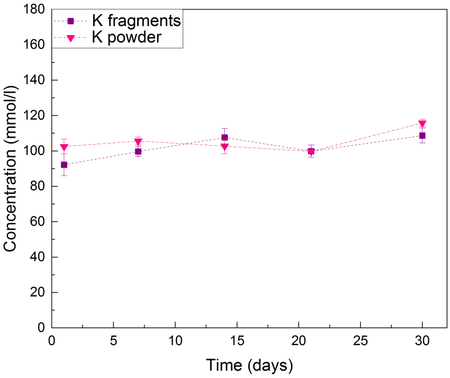

(a) K from the FLiNaK-water mixture.

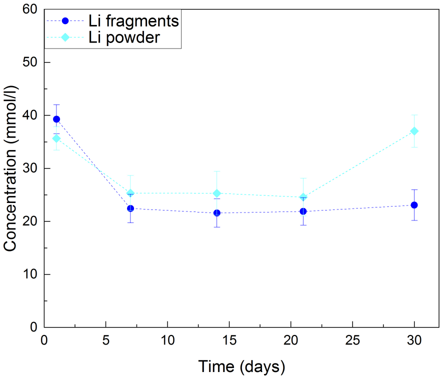

(b) Li from the FLiNaK-water mixture.

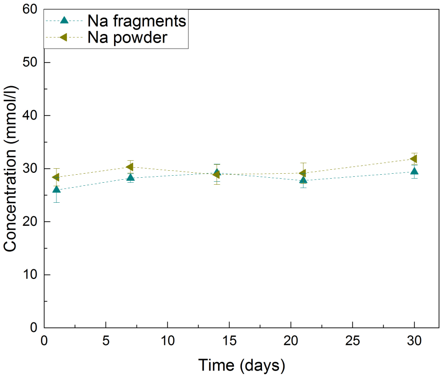

(c) Na from the FLiNaK-water mixture.

Figure 5.1: Solution concentration of K (a), Li (b), Na (c) measured after mixing FLiNaK with 99 wt% of water at 25řC.

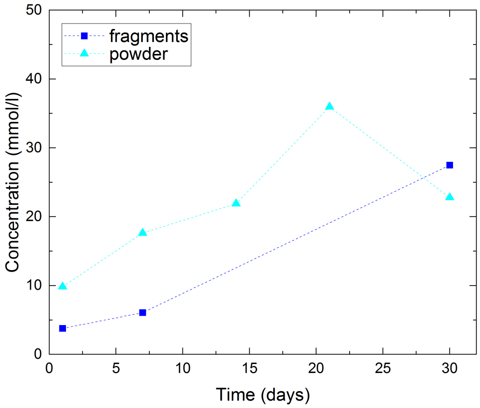

(a) Li from the LiF-ThF$_4$-water mixture.

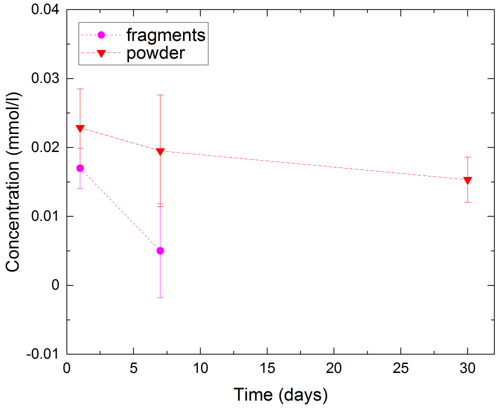

(b) Th from the LiF-ThF$_4$-water mixture.

Figure 5.2: Solution concentration of Li (a) and Th (b) found upon mixing 0.78LiF-0.22ThF$_4$ with 99 wt% of water at 25řC.

5.3.3. DISSOLUTION OF LIF-THF$_4$-UF$_4$ IN WATER

The concentration of lithium, thorium and uranium released from the salt in water were analysed and the concentration is shown separately. Five different situations were studied:

- 10 mg of the powdered salt was mixed with 1 ml of water,
- 10 mg of the salt in form of fragments was mixed with 1 ml of water,
- 10 mg of the powdered salt was mixed with 2 ml of water,
- 100 mg of the powdered salt was mixed with 10 ml of water,
- 100 mg of the salt in form of fragments was mixed with 10 ml of water.

In the latter two cases, the supernatant water was extracted and analysed after defined time intervals of 1, 7, 14, 21, 30 days. In all the other cases, several vials of mixtures were prepared and the water was filtrated and analysed. Also, two similar experiments in which 10 mg of the powdered salt was mixed with 1 ml of water were performed and analysed with the two optical emission spectrophotometers, the Perkin Elmer and the Ultima2, to check for the repeatability of the experiment.

Figure 5.3 shows the amount of lithium dissolved in water from the LiF-ThF$_4$-UF$_4$ mixture. The concentration of lithium measured from the water filtrated from 18 vials (one per each time interval and situation) containing the mixtures of salt and water is shown in Figure 5.3a. The measured concentration increased during one month. As in the case of LiF-ThF$_4$ salt, the lithium released from the fragments of the salt is less than from the powdered salt due to the smaller surface. The repeated experiment showed good agreement as shown in Figure 5.3a, where the concentration data measured with the Optima2 spectrophotometer are named as "second experiment, powder, init. eq. cont. of 10 g/l" to differentiate them from the previous ones. The concentration of lithium was also measured in the water filtrated from a mixture containing 10 mg of salt and 2 ml of water to see if doubling the amount of water had an influence on the leaching of this cation. In Figure 5.3a, it is shown that the concentration of lithium remained the same. The last two cases studied concerned the analysis of the supernatant water extracted from the solution. In Figure 5.3b, the concentration of lithium coming from this bigger vial is shown. Also in this case the lithium concentration released from the powdered salt is higher than the one left as fragments and comparable to the concentration shown in Figure 5.3a.

Figure 5.4a shows the concentration of thorium in water from the two solutions containing 1 and 2 ml of water with 10 mg of salt each. The concentration of thorium from the mixtures of water and salt in form of fragments is not reported in the Figure 5.4a because the amount of thorium released from the fragments of salt was below the limit of detection. Also for the thorium, as for the lithium, the solution that was less concentrated initially released less thorium in water. Figure 5.4b shows the concentration of thorium from the supernatant water of the solution with initial equivalent content (init. eq. cont.) of 10 g/l. The concentration in this case is higher than in the previous case. In all the situations, a drop after two weeks of dissolution is visible. The same drop in concentration was seen for the lithium released from the batch with init. eq. cont. of 10

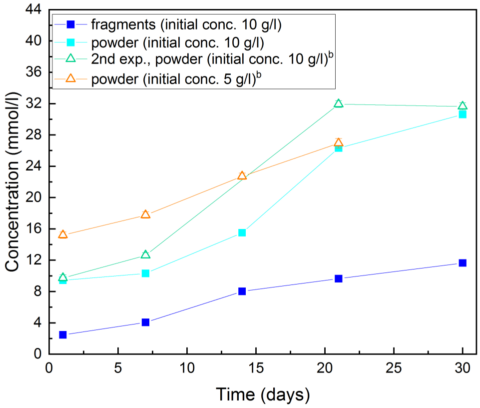

(a) Li from the LiF-ThF_4-UF_4-water mixture.

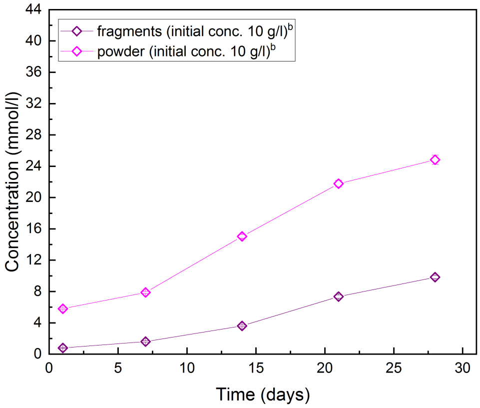

(b) Li from the supernatant water of the LiF-ThF_4-UF_4-water mixture.

Figure 5.3: Solution concentrations of lithium found upon mixing LiF-ThF_4-UF_4 with water at 25řC. (a) The concentration was measured with the Perkin Elmer Optima 4300 DV instrument from the fragmented and powdered salt mixtures with initial concentration of 10 g/l. These are confronted with the mixtures of powder and water with initial concentration of 10 and 5 g/l measured with the Ultima2 instrument[b] (open symbols). (b)The concentration found in the supernatant water of the mixtures of powder and salt with water was also measured with the Ultima2 spectrophotometer[b].

g/l measured with the Optima spectrophotometer and it was first thought that it was due to a failure of that specific batch. However, this is always visible for thorium implying it should have another origin. One explanation may be that the ThF_4 dissolution in water might be a rapid process (faster than the single day after which we analysed the concentration) while another process occurs at the same time, driven by slower kinetics: a solid crust formation on the surface of the remaining solid phase, likely hydroxide phase (confirmed by XRD in section 5.3.6) which prevents further dissolution of ThF_4 into water (or suppresses significantly). Successively, the already dissolved Th turns from fluoride phase to hydroxide or oxide phase which precipitates [26–28], leading to a concentration decrease of Th in water.

The concentration is in all the situations very small. Probably the competition between the dissolution of thorium and the formation of the solid crust and the quick precipitation of oxide-/hydroxide- phase had an influence on the low concentration of thorium in water.

Figures 5.5a and 5.5b show the concentration of uranium in the same situations described before. Also in this case the two solution with init. eq. cont. of 10 g/l are in good agreement and the one with init. eq. cont. of 5 g/l has very similar concentration. The concentration of uranium released from the supernatant water is lower than in the previous cases. In all the cases the concentration of uranium in water was increasing for the reported period of one month.

5.3.4. DISSOLUTION OF $LiF-ThF_4$ AND $LiF-ThF_4-UF_4$ (INFLUENCE OF RADIATION)

The LiF-ThF_4 and LiF-ThF_4-UF_4 salt mixtures with water were additionally analyzed after being irradiated in a Co-60 irradiation facility. In this case study, 10 mg of the two powdered salts were mixed with 1 ml of water. The three salt mixtures were dissolved in water placing the crucibles filled with the mixtures in a Co-source for 2, 6 and 12 hours.

The concentration of lithium from the LiF-ThF_4 and LiF-ThF_4-UF_4 salt mixtures with water is shown in Figure 5.6a. For the LiF-ThF_4 and water mixtures, the concentration was higher compared to the non-irradiated ones shown in Figure 5.6a. For the LiF-ThF_4-UF_4 and water mixtures, the concentration of lithium was high after 2 hours of dissolution and decreased after 6 and 12 hours. Also for the LiF-ThF_4-UF_4 mixture, we did a comparison with the concentration for non-irradiated mixtures. The comparison was done with the mixture of LiF-ThF_4-UF_4 and water with initial eq. cont. of 10 g/l analysed at TU Delft because the instrument used for the ICP-OES analysis was the same as the one for the irradiated mixtures.

The concentration of thorium, shown in Figure 5.6b, was higher or similar to the one of non irradiated mixtures. The concentration of thorium in water tends to decrease in time, which is similar to the thorium from mixtures in normal condition. Most probably this is due to the formation of precipitates of thorium oxides that prevents the further dissolution of thorium in water. In the case of the LiF-ThF_4-UF_4 mixture, the comparison with the non irradiated mixture with initial eq. cont. of 10 g/l analysed in Delft was not possible because in that case we encountered a concentration that was below the limit of detection (LOD). The comparison was therefore done with the mixture shown also in Figure 5.4a with initial eq. cont. of 10 g/l.

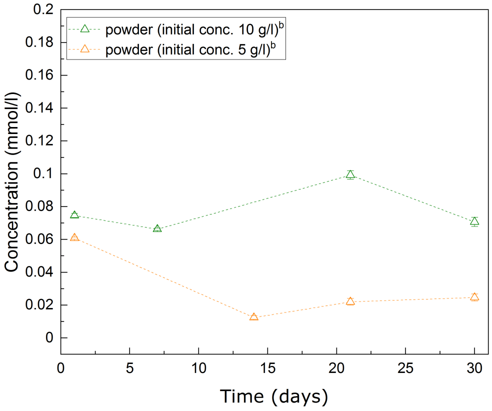

(a) Th from the LiF-ThF$_4$-UF$_4$-water mixture.

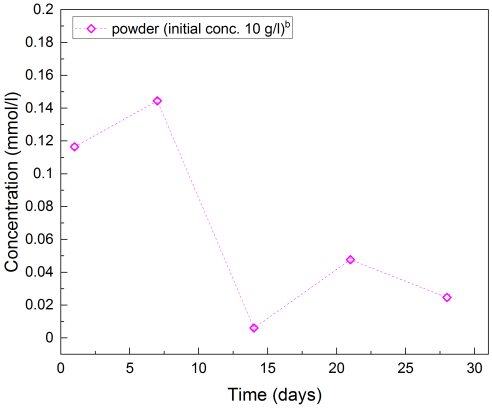

(b) Th from the supernatant water of the LiF-ThF$_4$-UF$_4$-water mixture.

Figure 5.4: Solution concentrations of thorium found upon mixing LiF-ThF$_4$-UF$_4$ with water at 25řC. (a) Mixtures of powder and water with initial concentration of 10 and 5 g/l. (b) Concentration found in the supernatant water of the mixtures of powder with water.

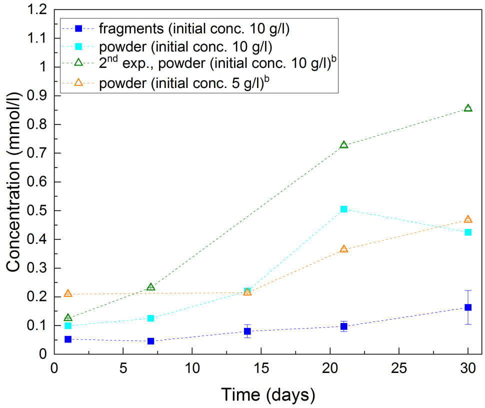

(a) U from the LiF-ThF_4-UF_4-water mixture.

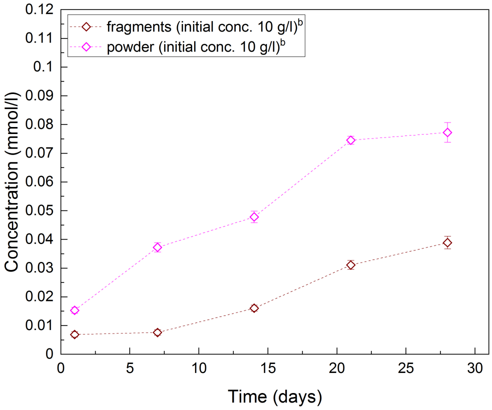

(b) U from the supernatant water of the LiF-ThF_4-UF_4-water mixture.

Figure 5.5: Solution concentrations of uranium found upon mixing LiF-ThF_4-UF_4 with water at 25řC. (a) The concentration was measured with the Perkin Elmer Optima 4300 DV instrument from the fragmented and powdered salt mixtures with init. eq. cont. of 10 g/l. These are compared with the mixtures of powder and water with initial concentration of 10 and 5 g/l measured with the Ultima2 instrument[b] (open symbols). (b) The concentration found in the supernatant water of the mixtures of powder and salt with water was also measured with the Ultima2 spectrophotometer[b].

The concentration of uranium from the irradiated mixtures shown in Figure 5.6c did not rise to higher levels comparing with dissolution under normal conditions.

The dissolution of lithium and thorium were therefore influenced by the radiation that increased the amount of these cations dissolved in water, while the concentration of uranium did not increase after irradiating the mixture.

5.3.5. DISSOLUTION OF $LiF-ThF_4$ AND $LiF-ThF_4-UF_4$ (INFLUENCE OF TEMPERATURE)

In order to study the effect of the temperature on the dissolution of lithium, thorium and uranium cations in water, the LiF-ThF_4 and LiF-ThF_4-UF_4 salt mixtures with water were additionally analyzed after being heated at 75řC. The salts were dissolved in water placing the crucibles filled with the mixtures in a furnace. The concentration of Li and Th shown respectively in Figure 5.7a and 5.7b were higher when the mixtures were heated compared to the one from the mixtures at 25 °C. The comparison is done with the same mixtures as for the previous study of the dissolution of salt under γ-irradiation. As for the previous cases, the concentration of thorium in water tends to decrease in time. The concentration of uranium from heated mixtures shown in Figure 5.7c did not rise to higher levels than those found for the uranium from dissolution under normal conditions.

5.3.6. SAMPLE CHARACTERISATION

X-RAY DIFFRACTION

After the dissolution experiments, some of the filtered and dried salt mixtures were analysed by XRD searching for the formation of oxide or hydroxide phases. The LiF-ThF_4 salt mixed with water with initial eq. cont. of 10 g/l and the LiF-ThF_4-UF_4 salt mixed with water with initial eq. cont. of 10 g/l were analysed before being mixed with water and after being mixed with water for one week and one month.

From the XRD patterns obtained from the dried powder filtrated from water after the dissolution experiment, some useful information could be collected. Figure 5.8 presents the XRD patterns of the LiF-ThF_4 salt before and after interacting with water. From the structural analysis done on the LiF-ThF_4 salt before reacting with water (the dotted diffractogram shown in Figure 5.8), the only phase Li_3ThF_7 was detected. The patterns of the salt after reaction with water show the presence of new peaks at 22ř and 45ř. These two peaks are relative to the hydrate compounds $Li_3Th_5[OH]F_{22}$ which has an intense peak at 22ř, and $ThF_4 \cdot 1.5\ H_2O$ with an intense peak at 45ř. A clearer presence of an oxide or hydroxide phase was not shown by the other X-Ray diffractograms. The diffractogram of the LiF-ThF_4-UF_4 salt mixed with water did not show the peaks attributed to oxide or hydroxide phases. The possible formation of these phases from the fluoride phase happened at room temperature, but in this condition the crystal structures visible with XRD are not formed. However, it is possible that amorphous oxide or hydroxide phase, not visible by XRD, were formed.

XAS ANALYSIS

In the current materials, uranium exists in the (IV) oxidation states. However, the interaction with the oxygen in air or the interaction with peroxide generated from water

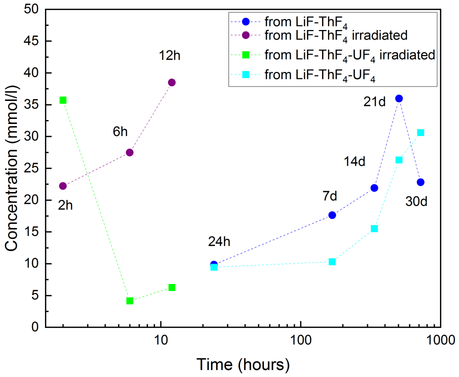

(a) Lithium dissolution in water.

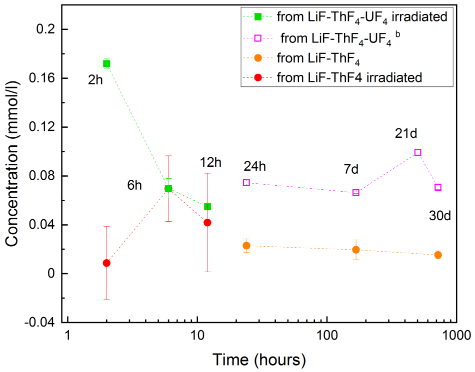

(b) Thorium dissolution in water.

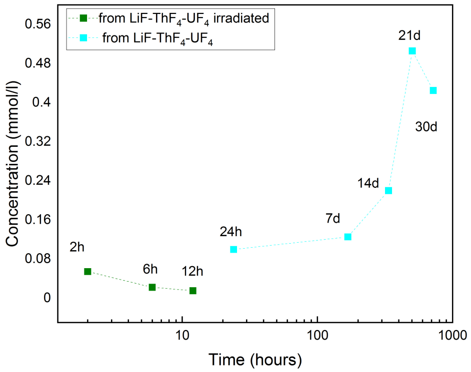

(c) Uranium dissolution in water.

Figure 5.6: Solution concentration of lithium (a), thorium (b) and uranium (c) found upon mixing LiF-ThF$_4$ and LiF-ThF$_4$-UF$_4$ with water in Co-source (1kGy/h). The init. eq. cont. of the mixtures were in all the cases, ca. 10 g/l.

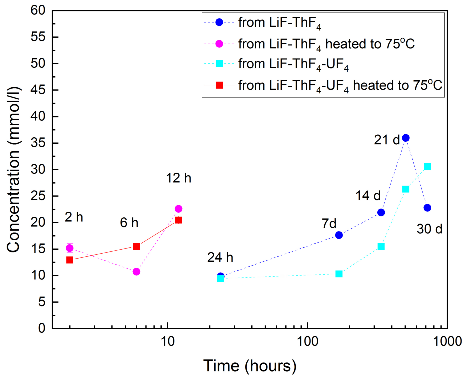

(a) Lithium dissolution in water.

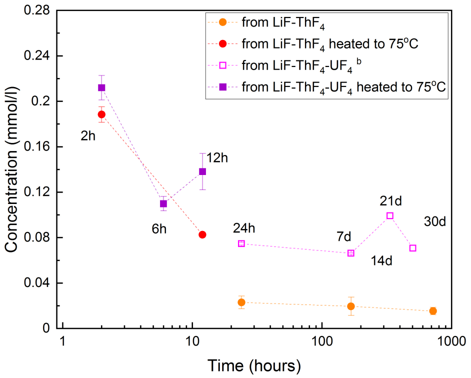

(b) Thorium dissolution in water.

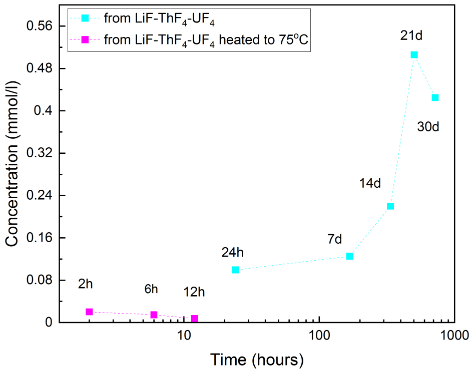

(c) Uranium dissolution in water.

Figure 5.7: Solution concentration of lithium (a), thorium (b) and uranium (c) found upon mixing LiF-ThF_4 and LiF-ThF_4-UF_4 with water at 75řC. The init. eq. cont. of the mixtures were in all the cases, ca. 10 g/l.

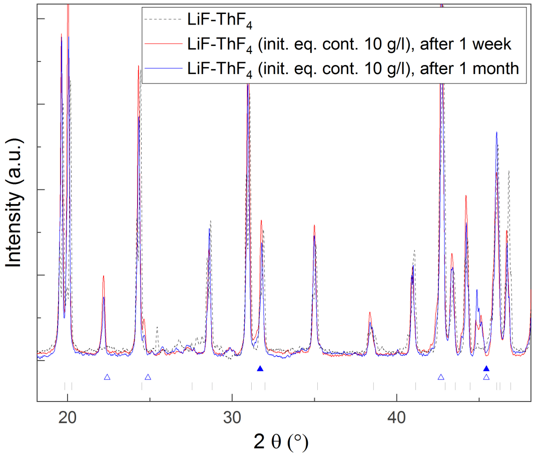

Figure 5.8: X-ray diffractograms of LiF-ThF$_4$: starting salt compared to salt mixed with water. Black, dotted diffractogram: starting salt fitted with Li_3ThF_7 (black bars). Red diffractogram: salt mixed with water (with init. eq. cont. of 10 g/l) for one week fitted with Li_3ThF_7 (black bars), $Li_3Th_5[OH]F_{22}$ (blue, empty triangles) and ThF_4 1.5 H_2O (blue, filled triangles). Blue diffractogram: salt mixed with water (with init. eq. cont. of 10 g/l) for one month fitted as the previous diffractogram.

by gamma radiation (in the case of the use of Co-source) could oxidise the uranium to the very soluble hexavalent state. A disproportion can occur by which uranium tends to be oxidised to the (V) and (VI) oxidation states [29]. Thus, an important point in the interpretation of the dissolution of fuel salt containing uranium fluoride systems is the possible change of the oxidation state of uranium under oxidising atmosphere. XANES experiments were performed at the DUBBLE line of the ESRF synchrotron in order to investigate the oxidation behaviour both in fresh and mixed with water samples. The spectra collected at the U-L_{III} edge on the investigates samples are shown in Figure 5.9 and compared to standard materials, namely $U^{+IV}O_2$, $(U^{+V}{}_{2/3},U^{+VI}{}_{1/3})_3O_8$ and $U^{+VI}O_3$ [30]. The spectra of the three U-containing fluorides are perfectly overlapping, indicating that the uranium oxidation state did not change because of interaction with water. Moreover, the white lines (maxima of the absorption spectra) of the fluorides are clearly aligned with the purely tetravalent UO_2 reference, crossed by a dashed line in Figure **??**. A shift of 1-2 eV toward higher energies is observed for U_3O_8 and UO_3, due to the higher oxidation state of uranium in these compounds. The absorption edges, defined as the first zero-crossing of the second derivative of the spectrum, and the white lines of the fluorides and the oxide references are reported in TABLE. The values of the fluorides are almost identical to those of UO_2, while a shift of 1-2 eV toward higher energies is observed for U_3O_8 and UO_3.

The present XANES results combined with the ICP-OES analysis, that reports a low concentration of uranium dissolved in water, confirm that the uranium did not change

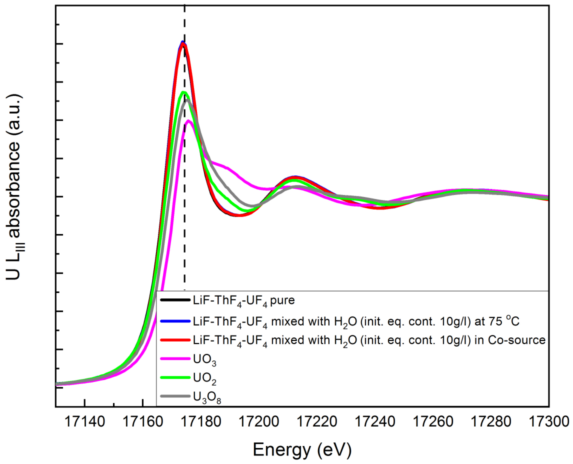

Figure 5.9: U LIII XANES spectra collected at ESRF on samples of LiF-ThF$_4$-UF$_4$ mixed with water in a irradiation facility and at high temperature and unmixed with water as reference.

its oxidation state remaining in its insoluble tetravalent state.

Table 5.3: Inflection points and white line of the XANES spectra. Values are given with 1.0 eV uncertainty.

Salt	Inflection point (eV)	White line (eV)
LiF-THF$_4$-UF$_4$ pure	17168.6	17173.8
LiF-THF$_4$-UF$_4$ with H_2O at 75 °C	17168.6	17173.9
LiF-THF$_4$-UF$_4$ ith H_2O in Co-source	17169.0	17174.0
UO_2	17168.0	17174.1
U_3O_8	17169,8	17175,2
UO_3	17171,0	17175,8

5.4. DISCUSSION

The solubility of the lithium, thorium and uranium cations in water was also studied by Briggs et al. [8] who dissolved a LiF-UF$_4$-ThF$_4$-BeF$_2$ mixture in water. Briggs reported a value of the concentration of lithium in water of $3.5 \cdot 10^{-1}$ mol/l after one day of dissolution, this value is one order of magnitude higher than the one found in this work where we measured a concentration of $3 \cdot 10^{-2}$ mol/l after one month of dissolution from all the mixtures of powdered LiF-ThF$_4$-UF$_4$ with water. When we measured the concentration of lithium from the unmolten LiF-ThF$_4$-UF$_4$ salt after one day of dissolution, shown in

Table 5.4, this resulted in higher values than the molten and ground sample at the same dissolution time showing that the solubility of the cation depends on the chemical state of the solid. However our values still did not reach the values reported by Briggs.

Regarding the solubility of ThF_4 in water, Briggs [8] reports a solubility limit of $3 \cdot 10^{-3}$ mol/l reached after one day of dissolution while we measured $5.5 \cdot 10^{-4}$ mol/l from the salt molten as Li_3ThF_7 and $1.4 \cdot 10^{-3}$ mol/l from the mixture containing only the initial end members. This last value was of the same order of magnitude as those reported by Briggs. This result confirms the hypothesis that the dissolution of thorium from the molten and re-solidified salt is lower than the dissolution of ThF_4 which is probably due to the formation of Li_3ThF_7. Briggs also measured the concentration of thorium in water up to ten days and did not find a decrease in concentration. In our case, we report a drop in the concentration of thorium in water after two weeks of dissolution assuming the precipitation of the hydroxide or oxide phase formed from thorium fluoride. The concentration of Th after irradiation or after heating (at 75řC) of the mixture slightly increased with respect to the same concentration for the reaction with water in normal conditions.

For uranium, the maximum value from the melted, re-solidified and powdered LiF-ThF_4-UF_4 sample was reached after one month with a value of $8.5 \cdot 10^{-4}$ mol/l. A similar value was presented by Briggs, but was reached after one day of interaction with water. Repeating the experiment on the un-molten salt, we reached $9.7 \cdot 10^{-4}$ mol/l after one day of dissolution. For the mixture irradiated and heated, the concentration of U was lower than for the mixtures left at 25řC. It was expected that the action of the oxygen from air or the action of peroxide generated by beta-gamma radiation in water could oxidise the uranium to the very soluble hexavalent state, but this was not noticed in the XAS spectra (in Figure 5.9) and the results on the solubility did not show a valuable increment of solubility.

The measurements, performed in the same condition as [8], are comparable to the results from the literature. In all the other cases, the formation of Li_3ThF_7 lowered the amount of cations dissolved in water.

5.5. Conclusions

Experimental data on the dissolution of molten fuel salt in water are provided. The study was executed on the simulant fuel salt FLiNaK to test the procedure and successively on the eutectic LiF-ThF_4 (78-22 mol%) mixture and on the LiF-ThF_4-UF_4 (76.2-21.3-2.5 mol%) fuel mixture. For the two compositions: the eutectic LiF-ThF_4 and the LiF-ThF_4-UF_4 fuel mixture, the concentration of Th and U in water remained low (below 1 mmol/l) in all cases studied. The data on the solubility of the single cations after irradiation are representative for an accident environment where the molten fuel at high temperature interacts with water from the storage tanks and may dissolve radioactive cations. The temperature in case of accidents may be considerably higher than 25řC for a long time. Measurements of the fuel salt in water at an elevated temperature of 75řC have been made for evaluating the probable course of events in the weeks following a postulated incident. It was found that the concentration of dissolved lithium and thorium increased with respect to the concentration from the mixtures at room temperature, increasing the temperature and placing the mixtures in a Co-source. The concentration of uranium was

Table 5.4: Concentration of MSR fuel mixtures in water

										Concentration mmol/l							
Initial concentration	FLiNaK 10 g/l			LiF-ThF$_4$ 10 g/l		LiF-ThF$_4$-UF$_4$ 10 g/l			LiF-ThF$_4$-UF$_4$[a] 10 g/l supernatant solution			LiF-ThF$_4$-UF$_4$[a] 10 g/l			LiF-ThF$_4$-UF$_4$[a] 5 g/l		
	Li	Na	K	Li	Th	Li	Th	U	Li	Th	U	Li	Th	U	Li	Th	U
Time days										fragments							
1	39.28	25.98	92.17	3.781	$16.98\cdot10^{-2}$	2.462	$\leq$ LOD[b]	$5.222\cdot10^{-2}$	$7.854\cdot10^{-1}$	$\leq$ LOD[b]	$6.907\cdot10^{-3}$						
7	22.44	28.22	99.69	6.064	$5.008\cdot10^{-3}$	4.055	$\leq$ LOD[b]	$4.575\cdot10^{-2}$	1.611	$\leq$ LOD[b]	$7.607\cdot10^{-3}$						
14	21.58	29.22	107.6			8.020	$\leq$ LOD[b]	$8.028\cdot10^{-2}$	3.614	$\leq$ LOD[b]	$1.606\cdot10^{-2}$						
21	21.89	27.76	99.87			9.636	$\leq$ LOD[b]	$9.703\cdot10^{-2}$	7.350	$\leq$ LOD[b]	$3.110\cdot10^{-2}$						
30	23.08	29.40	108.7	27.49	$9.807\cdot10^{-2}$	11.64	$\leq$ LOD[b]	$1.633\cdot10^{-1}$	9.822	$\leq$ LOD[b]	$3.884\cdot10^{-2}$						
										powder							
1	35.66	28.38	102.5	9.837	$2.288\cdot10^{-2}$	9.441	$\leq$ LOD[b]	$9.946\cdot10^{-2}$	5.803	$1.165\cdot10^{-1}$	$1.532\cdot10^{-2}$	9.714	$7.450\cdot10^{-2}$	$1.253\cdot10^{-1}$	15.20	$6.086\cdot10^{-2}$	$2.095\cdot10^{-1}$
7	25.34	30.33	105.6	17.63	$1.950\cdot10^{-2}$	10.31	$\leq$ LOD[b]	$1.254\cdot10^{-2}$	7.882	$1.445\cdot10^{-1}$	$3.724\cdot10^{-2}$	12.59	$6.612\cdot10^{-2}$	$2.319\cdot10^{-1}$			
14	25.31	28.88	102.7	21.89		15.51	$\leq$ LOD[b]	$2.199\cdot10^{-1}$	15.03	$\leq$ LOD[b]	$4.783\cdot10^{-2}$				17.75	$1.243\cdot10^{-2}$	$2.148\cdot10^{-1}$
21	24.59	29.14	99.73	35.96		26.31	$\leq$ LOD[b]	$5.058\cdot10^{-1}$	21.77	$4.770\cdot10^{-2}$	$7.456\cdot10^{-2}$	32.21	$1.000\cdot10^{-1}$	$7.337\cdot10^{-1}$	22.71	$2.199\cdot10^{-2}$	$3.645\cdot10^{-1}$
30	37.05	31.86	115.8	22.79	$1.533\cdot10^{-2}$	30.61	$\leq$ LOD[b]	$4.249\cdot10^{-1}$	24.83	$2.461\cdot10^{-2}$	$7.721\cdot10^{-2}$	31.60	$7.065\cdot10^{-2}$	$8.544\cdot10^{-1}$	26.97	$2.471\cdot10^{-2}$	$4.688\cdot10^{-1}$
Time hours						irradiated											
2				22.17	$8.776\cdot10^{-3}$	35.70	$1.7188\cdot10^{-1}$	$5.427\cdot10^{-2}$									
6				27.47	$6.958\cdot10^{-2}$	4.159	$6.982\cdot10^{-2}$	$2.205\cdot10^{-2}$									
12				38.48	$4.173\cdot10^{-2}$	6.250	$5.473\cdot10^{-2}$	$1.513\cdot10^{-2}$									
						heated at 75°C											
2				15.18	$1.883\cdot10^{-1}$	12.94	$2.119\cdot10^{-1}$	$2.022\cdot10^{-2}$									
6				10.71		15.52	$1.098\cdot10^{-1}$	$1.468\cdot10^{-2}$									
12				22.57	$8.255\cdot10^{-2}$	20.46	$1.380\cdot10^{-1}$	$7.710\cdot10^{-3}$									
Time days							un-molten salt										
1						14.74	1.425	$9.6910\cdot10^{-1}$									

[a] These solutions were analysed in JRC-Karslruhe with a Ultima2, HORIBA Jobin Yvon instrument.

[b] These results are below the detection limit (LOD). For Th, LOD in the analysed samples is 0,030 mg/kg, which (considering the dilution factor) corresponds to a limit of detection of $7.7\cdot10^{-3}$ mmol/l.

not influenced by the temperature and irradiation condition. The material characterisation performed before and after interaction of the salt with water by XRD permitted the identification of the hydrate species $Li_3Th_5[OH]F_{22}$ and $LiThF_4 \cdot 1.5\ H_2O$. The current results are important for the understanding of the nuclear fuel behaviour in case of an accident during which the molten fuel salt interacts with water from the storage tanks and may dissolve highly radioactive cations. As mention in the introduction, these type of data are of importance to evaluate the safety and the performance of the MSR as well as to evaluate the reprocessing scheme.

5.6. ACKNOWLEDGMENTS

The authors would like to express their gratitude to the support team of the BM26 beamline and in particular to Banerjee Dipanjan for the help received during the XAS experiments. S. Mastromarino acknowledges also the ENEN + project for supporting her stay at JRC-Karlsruhe, and the Horizon 2020 SAMOFAR project for funding this project.

REFERENCES

[1] *Technology Roadmap Update for Generation IV Nuclear Energy Systems*, Tech. Rep. (OECD Nuclear Energy Agency for the Generation IV Internation Forum, 2014).

[2] O. Beneš, M. Salanne, M. Levesque, and R. J. M. Konings, *DELIVERABLE D 3.2 Physico-Chemical properties of the MSFR fuel salt Evaluation and Viability of Liquid Fuel Fast Reactor System EVOL Contract (grant agreement) number: 249696*, Tech. Rep. (2013).

[3] L. Luzzi, V. Di Marcello, and A. Cammi, *Multi-Physics Approach to the Modelling & Analysis of Molten Salt Reactors*, edited by L. Luzzi, V. Di Marcello, and A. Cammi (Nova Science Publishers Inc, New York, United States, 2012) pp. 1–140.

[4] D. LeBlanc, *Molten salt reactors: A new beginning for an old idea,* Nuclear Engineering and Design **240**, 1644 (2010).

[5] M. Allibert, D. Gérardin, D. Heuer, E. Huffer, A. Laureau, E. Merle, S. Beils, A. Cammi, B. Carluec, S. Delpech, A. Gerber, E. Girardi, J. Krepel, D. Lathouwers, D. Lecarpentier, S. Lorenzi, L. Luzzi, S. Poumerouly, M. Ricotti, and V. Tiberi, *A Paradigm Shift in Nuclear Reactor Safety with the Molten Salt Fast Reactor Grant Agreement number: 661891 SAMOFAR D1.1 Description of initial reference design and identification of safety aspects*, Tech. Rep. (2016).

[6] R. Yoshioka, K. Mitachi, Y. Shimazu, and M. Kinoshita, *Safety criteria and guidelines for MSR accident analysis*, Tech. Rep. (Japan, 2015).

[7] R. J. Belles, G. F. Flanagan, and M. Voth, *ORNL/TM-2018/834, Proposed guidance for preparing and reviewing molten salt nonpower reactor license application (NUREG-1537),* Tech. Rep. (Oak Ridge National Laboratory, 2018).

[8] R. B. Briggs, *ORNL-3282 Molten salt reactor program semiannual progress report*, Tech. Rep. (Oak Ridge National Laboratory, 1962).

[9] J. W. Koger, *ORNL-TM-3866 Corrosion and mass transfer characteristics of NaBF*$_4$*-NaF*$_4$ *(92-8 mole %) in hastelloy-N*, Tech. Rep. (Oak Ridge National Laboratory, 1972).

[10] P. Souček, O. Beneš, B. Claux, E. Capelli, M. Ougier, V. Tyrpekl, J. F. Vigier, and R. J. M. Konings, *Synthesis of UF*$_4$ *and ThF*$_4$ *by HF gas fluorination and re-determination of the UF*$_4$ *melting point,* Journal of Fluorine Chemistry **200**, 33 (2017).

[11] E. Capelli, O. Beneš, and R. J. M. Konings, *Thermodynamic assessment of the LiFNaFBeF*$_2$*ThF*$_4$*UF*$_4$ *system,* Journal of Nuclear Materials **449**, 111 (2014).

[12] E. Merle-Lucotte, D. Heuer, M. Allibert, X. Doligez, and V. Ghetta, *Minimizing the fissile inventory of the molten salt fast reactor,* Advances in Nuclear Fuel Management IV (ANFM IV) (Apr 2009).

[13] A. E. of Canada, *Instruction manual, gammacell 220 Cobalt 60 Irradiation Unit*, Atomic Energy of Canada, Commercial products, P.O. BOX 93, Ottawa, Canada (July, 1968).

[14] T. R. Dulski, *Trace elemental analysis of metals* (1999).

[15] E. Prichard, G. M. MacKay, and J. Points, *Trace analysis: A structured approach to obtaining reliable results* (1996).

[16] A. Montaser and D. W. Golightly, *Inductively Coupled Plasmas in Analytical Atomic Spectrometry*, Vol. 2 (1991).

[17] J. Rodríguez-Carvajal, *Recent advances in magnetic structure determination by neutron powder diffraction,* Physica B: Physics of Condensed Matter **192**, 55 (1993).

[18] A. Le Bail, *Whole powder pattern decomposition methods and applications: A retrospection,* Powder Diffraction **20**, 316326 (2005).

[19] M. Borsboom, W. Bras, I. Cerjak, D. Detollenaere, D. G. van Loon, P. Goedtkindt, M. Konijnenburg, P. Lassing, Y. K. Levine, B. Munneke, M. Oversluizen, R. van Tol, and E. Vlieg, *The Dutch-Belgian beamline at the ESRF,* Journal of Synchrotron Radiation **5**, 518 (1998).

[20] B. Ravel and M. Newville, *ATHENA, ARTEMIS, HEPHAESTUS: data analysis for X-ray absorption spectroscopy using IFEFFIT,* Journal of Synchrotron Radiation **12**, 537541 (2005).

[21] X. H. An, J. H. Cheng, T. Su, and P. Zhang, *Determination of thermal physical properties of alkali fluoride/carbonate eutectic molten salt,* AIP Conference Proceedings **1850**, 1 (2017).

[22] J. Faridi and M. E. Guendouzi, *Solubility of potassium fluoride in aqueous solution at different temperatures* $298.15K353.15K$, MATEC Web of Conferences **5**, 4 (2013).

[23] C. B. Stubblefield and R. O. Bach, *Solubility of Lithium Fluoride in Water,* Journal of Chemical and Engineering Data **17**, 491 (1972).

[24] J. G. Reynolds and J. D. Belsher, *A Review of Sodium Fluoride Solubility in Water,* Journal of Chemical and Engineering Data **62**, 1743 (2017).

[25] N. S. Nikolaev and Y. A. Luk'yanychev, *The determination of the solubility product of thorium tetrafluoride,* Atomnaya Energiya **12**, 334 (1962).

[26] A. Abrao, A. Alves de Freitas, and F. M. Sequeira de Carvalho, *Preparation of highly pure thorium nitrate via thorium sulfate and thorium peroxide,* Journal of Alloys and Compounds **323/324**, 53 (2001).

[27] R. Prasad and A. K. Dey, *Studies on the Precipitation of Thorium Hydroxide,* Kolloid-Zeitschrift **175**, 136 (1960).

[28] M. Rand, J. Fuger, I. Grenthe, V. Neck, and R. Dhanpat, *Chemical thermodynamics of thorium*, Vol. 11 (2007).

[29] M. J. Welland, W. T. Thompson, B. J. Lewis, and D. Manara, *Computer simulations of non-congruent melting of hyperstoichiometric uranium dioxide,* Journal of Nuclear Materials **385**, 358 (2009).

[30] K. O. Kvashnina, S. M. Butorin, P. Martin, and P. Glatzel, *Chemical state of complex uranium oxides,* Phys. Rev. Lett. **111**, 253002 (2013).

6

CONCLUSION

The research described in this thesis focuses on understanding the chemico-physical properties of the fuel salt and coolant salt for Molten Salt Fast Reactors (MSFRs). The main goal was to provide more reliable data than is currently available for the properties of the salts. The properties of a range of salts were measured for the first time. For example, the melting point of LiF-ThF_4-UF_4-PuF_3 (77.5-6.6-12.3-3.6 mol%) and the thermal diffusivity of ThF_4, UF_4, PuF_3) and their mixtures were never measured before. Alkali fluorides (LiF, KF, NaF) and their mixture (FLiNaK) were measured as well as ThF_4, UF_4, PuF_3 and their mixtures. Effort was put into understanding how the properties of the salts change depending on their oxidation, chemical state, composition and temperature. For example, the oxidation of alkali and actinide fluorides causes differences in their melting point. Also, the alkali fluorides show different values of thermal conductivity compared to the actinide fluorides. Moreover, the alkali fluorides have a higher solubility in water with respect to the actinide fluorides.

The measurement of the chemico-physical properties of the salts was achieved by using established techniques and by developing new crucibles and methods. The melting point of some salts was evaluated by using the established differential scanning calorimetry (DSC) by using new crucibles for higher temperatures. The established laser flash method was used for the measurement of the thermal diffusivity and the known inductively coupled plasma - optical emission spectrometry (ICP-OES) was used for studying the dissolution of fuel and coolant salt. For the study of the thermal diffusivity of the salts a new method for the pellet preparation was developed. Also, an innovative technique was successfully used for measuring the viscosity of low viscous fluids.

This work has been conducted within the Euratom Horizon 2020 SAMOFAR project. This conclusive chapter reports also the main results of this research and provides recommendations for future studies.

6.1. DISCUSSION AND CONCLUSION

6.1.1. MELTING POINT OF PuF_3 AND MSFR FUEL MIXTURE

Knowing the melting point of the fuel salt is important for determining the operating temperature of the reactor. The melting point of the MSFR fuel mixture LiF-ThF_4-UF_4-PuF_3 (77.5-6.6-12.3-3.6 mol%) has never been reported in literature. Among the single components of the salt, the melting point of LiF, ThF_4 and UF_4 is known [1], while few literature data have been collected on the melting point of PuF_3 [2–4]. The latter ones are scattered between 1442 and 1909 K. The optimization of the phase diagrams of the salts containing PuF_3 requires the correct value of its melting point, therefore we addressed the questions:

Why is the melting point of PuF_3 scattered by 500 K? Can we measure the melting point of PuF_3 more accurately?

Aiming to lower the uncertainty in the melting point measurement of PuF_3, we measured the salt via DSC. The usual stainless steel crucible with nickel liner could not be used for these DSC measurements because these materials would melt at the range of temperature where the melting point of PuF_3 was expected. New materials were tested and a considerable effort was made to choose and manufacture a crucible out of materials that could also be used with the corrosive molten salts. BN without and with liners of Pt or W, graphite and glassy carbon were used as materials for the crucibles. During the measurements we observed that the melting point of PuF_3 was influenced by the material of the crucibles in which it was molten. A difference of approximately 40 K between all the measurements was found. The measured melting point of PuF_3 was between 1647 and 1687 K. We noticed that it is important to check the purity of the sample before and after DSC measurement by XRD. PuOF was formed when PuF_3 was melted in BN and graphite crucibles. The formation of the oxide phase was visible from both the DSC curves (where two peaks were present) and the XRD patterns. The formation of oxide phases could have, caused the uncertainty of 500 K in the melting point of PuF_3. Robinson [4] and Westrum and Wallmann [3] have also found that PuOF was formed after melting of PuF_3. Using crucible materials that do not contain oxygen, the formation of oxide phases can be avoided. We have seen that PuOF was formed when using graphite and BN crucibles. Both these materials are porous and the cause of the formation of PuOF might be due to the oxygen present in the crucible. Using a crucible of BN with a liner of Pt or W might solve this issue. Controlling that the atmosphere is free of oxygen during the measurement of the melting point is also crucial to avoid the formation of oxide phases. In this work, the melting point of PuF_3 was measured with higher accuracy with respect to the literature results. The DSC curves of the Pu_3 measured in a BN crucible with liners in Pt and W were repeatable, the standard deviation was 2 K, while in the measurements performed with graphite and BN crucibles the standard deviation was 14 K. However, the XRD has not been performed yet on the samples measured in BN + liners and we can not demonstrate the non formation of oxide phases.

A correct measurement of the melting point was also aimed for the MSFR fuel salt mixture. The phase diagram of the pseudo binary phase diagram of LiF-UF_4 with fixed amount of ThF_4 (6.6 mol%) and PuF_3 (3.6 mol%) has been optimized in [5] and we questioned:

Do the solidus and liquidus temperature of LiF-ThF_4-UF_4-PuF_3 (77.5-6.6-12.3-3.6 mol%) agree with the modeled phase diagram?

The purification of the single components was an essential first step for the study of the melting point. PuF_3, ThF_4 and UF_4 were synthetized by hydrofluorination of respectively PuO_2, ThO_2 and UO_2 using HF [1]. The characterization of the single fluorides by XRD analysis confirmed the purity of the samples, important for a reliable determination of its basic thermodynamic properties. ThF_4, UF_4, LiF were also singularly analyzed via DSC to confirm their purity. The presence of one single peak on the DSC curve demonstrated the purity of the compounds. The same procedure was tried for PuF_3, but in many cases the oxide was formed while melting the sample due to its high melting point. The MSFR mixture was measured using the standard crucibles for the DSC. The results, liquidus and solidus point, were compared and plotted on the phase diagram modeled using the thermodynamic database assessed by Capelli et al. [6]. The measurement of the solidus temperature (776 ± 2 K) agreed with the modeled phase diagram, while a difference of 40 K was found for the liquidus temperature (893 ± 10 K). The difference between the liquidus temperature from the experiments and from the modeled phase diagram was explained by a error either in the optimization of the phase diagram or in the preparation of the sample. Considering that a difference of 1.5 % towards the LiF component corresponds to a liquidus temperature shift of 40 K, an error in the preparation of the sample can be the reason for the disagreement of the liquidus value.

The melting point of PuF_3 and of the fuel mixture are reported in Table 6.1.

Table 6.1: Melting temperatures of PuF_3 and of MSFR fuel mixture LiF-ThF_4-UF_4-PuF_3 (77.5-6.6-12.3-3.6 mol%) measured by DSC in this work and obtained by the phase diagram in [5].

Composition	Solidus temperature	Liquidus Temperature
PuF_3		1681 ± 2 K
LiF-ThF_4-UF_4-PuF_3 (77.5-6.6-12.3-3.6 mol%)	776 ± 2 K (776 K)	893 ± 10 K (852 K)

In parentheses, the values from the modeled phase diagram.

The melting point reported for PuF_3 is the average of the melting points measured using the crucibles in BN with liners in Pt and W.

6.1.2. THERMAL CONDUCTIVITY OF ALKALI FLUORIDES (LIF, KF, NAF) AND ACTINIDE FLUORIDES (THF_4, UF_4, PUF_3) AND THEIR MIXTURES

The second section of this thesis presents new data on the thermal diffusivity of alkali and actinide fluorides. These data were measured with an established method, the laser flash method, but in an innovative manner. The thermal diffusivity of LiF has been measured in literature [7, 8], but no data have been found for the other solid alkali fluorides and for any of the actinide fluorides. We inquired:

What is the thermal conductivity of alkali and actinide fluorides below their melting point?

In this work we measured the thermal diffusivity of a series of solid alkali fluorides (LiF, NaF, and KF), including the ternary mixture FLiNaK, of PuF_3 and of solid MSFR fuel mixtures (LiF-ThF_4, LiF-ThF_4-UF_4, LiF-ThF_4-UF_4-PuF_3). The thermal diffusivity was measured in the temperature range from 500 K to 100 K below the melting point of each sample. Measuring the thermal diffusivity below the melting point of the salts is needed to know the heat transferred through the solidified salt in case of the formation of a solid crust at the walls of the piping and at the freeze plug of the MSR.

The method for the preparation of the salts for the laser flash analysis had to be designed before starting the experiments. The laser flash method has been used for pellets of oxides but never for fluorides. Along the progress of the PhD research, some tests were performed: the salt was first pressed into pellets, then pressed and sintered, and finally molten and re-solidified into solid pieces analyzable by the laser flash facility. The results are shown in Table 6.2 for the salts that were pressed and molten and re-solidified. The method that was selected as the most reliable was the pre-melting and resolidifying of the salts. Some of the pressed and sintered pellets presented cracks on their surface or broke during the laser flash measurements, the pre-molten disks of all the salts did not broke during any measurement. The method of melting and producing solid-crystalline salt is also the most representative for the purpose of studying a salt crust formed after the salt is molten and re-solidified.

The thermal diffusivity was then translated into thermal conductivity using the experimentally measured density and heat capacity. The thermal conductivity at 650 and 800 K is shown in Table 6.2. Since the experimental data were taken at a temperature ranging from room temperature to 100 K below the melting point of the salts in intervals of approximately 50 K, the thermal conductivity was extrapolated at 650 and 800 K by linear fitting the experimental data.

We conclude that alkali fluorides have larger thermal conductivity than the molten salt mixtures. Also, the thermal conductivity is smaller for salts having more constituents. The only results present in literature for solid fluoride salts (between the ones considered in this work) were for LiF. The thermal diffusivity measured in this work for LiF showed good agreement with the literature values.

6.1.3. VISCOSITY MEASUREMENT OF LOW-VISCOUS LIQUIDS USING AN ULTRASONIC WAVEGUIDE

The interest in the viscosity of molten fluoride salts brought us to investigate innovative methods for measuring the viscosity. The characteristics of the molten salts being low-viscous, hygroscopic, radioactive and liquid at a temperature above 454°C, made us question:

Table 6.2: Thermal conductivity (W/m K) of the studied fuel and coolant compositions at 650 and 800 K.

Composition	Thermal conductivity			
	pressed pellets		pre-molten salts	
	650 K	800 K	650 K	800 K
LiF	4.88 ± 0.45	4.63 ± 0.43	6.75 ± 0.59	5.52 ± 0.49
NaF	2.40 ± 0.29	2.12 ± 0.26	6.63 ± 0.47	5.21 ± 0.37
KF	1.66 ± 0.20	1.43 ± 0.17	2.67 ± 0.60	2.40 ± 0.54
LiF-KF-NaF (46.5-11.5-42 mol %)	2.94 ± 0.10	2.05 ± 0.07	4.48 ± 0.53	1.78 ± 0.21
PuF_3	0.75 ± 0.42	0.79 ± 0.43	2.00 ± 0.12	1.87 ± 0.12
LiF-THF_4 (75-25 mol %)			2.07 ± 0.30	2.23 ± 0.33
LiF-ThF_4 -UF_4 (77.5-20.0-2.5 mol %)			1.70 ± 0.42	1.59 ± 0.39
LiF-ThF_4-UF_4-PuF_3 (77.5-6.6-12.3-3.6 mol%)			0.43 ± 0.31	0.45 ± 0.32

What method can be used for measuring low viscous, harsh liquids?

The method presented in chapter 4 has been developed by [9] and is based on the measurements of shear waves in waveguide immersed in a liquid. The shear waves are attenuated when the waveguide is immersed in a liquid and their attenuation depends on the immersion depth of the waveguide. We used this method improving its accuracy: we averaged 128 signals, we fitted the intensity of the signal as a function of the immersion depth with an exponential curve and we obtained the attenuation from the coefficient determined optimizing the exponential fitting. We measured liquids in the temperature range 20 to 75 °C; the measurement at a temperature higher than room temperature was not studied before for low viscous liquids. Also, the measurement of low viscous liquids has not been tackled in literature. The results presented in this thesis are preliminary, but show that it is possible to measure low viscous liquids using the ultrasonic viscometer. The use of a waveguide for measuring the viscosity of molten salts is beneficial because the method allows to use a small amount of liquid, has a small and compact set-up, has electronics distant from the radioactive salt and can measure with accuracy for low viscous salts. Figure 6.1 shows the viscosity measured in this work for a range of liquids with viscosity between 0.8 and 50 mPa·s at room temperature. The experimental results are compared to the reference values from the literature and show a relative error of 3 % except for ethanol that showed results off by 11.7%. The results by the ultrasonic viscometer are also compared to the results by a commercial falling ball viscometer. In this last case the relative error was slightly more significant, but still less than 5 % for all the liquids except for water, which showed a relative error of 11.9 %.

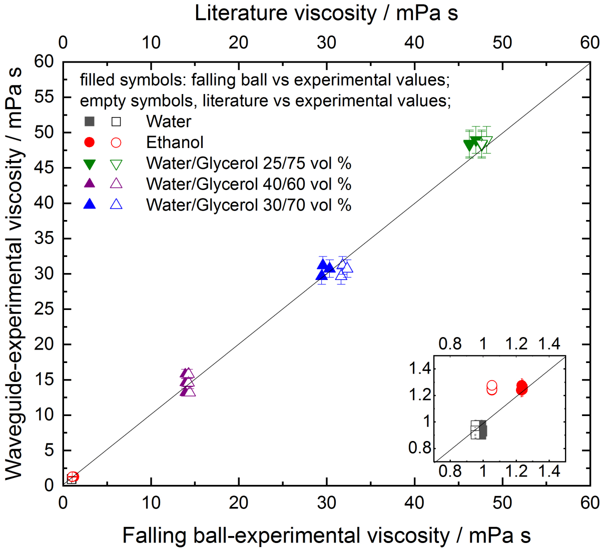

Figure 6.1: The viscosity from the shear guided waves attenuation for all the liquids measured is compared to the theoretical viscosity (a) and to the results from the falling ball viscometer (b) for the liquids at the same temperature. The error bars indicate the uncertainty of the method.

We conclude that it is possible to measure differences in viscosity as small as 0.3 mPa s: we measured the viscosity of ethanol and water that differ of 0.3 mPa s between each other. We measured the viscosity of a 25/75 volume % water/glycerol mixture varying the temperature of 1 °C. The viscosity was changing up to 4 mPa s each 1 °C. A first measurement at 70 °C was performed. The viscosity of pure glycerol was obtained within 8 % of literature data from 25 to 70 °C. Figure 6.2 shows the results for the viscosity of glycerol measured between 25 and 70 °C compared to the viscosity from the literature and measured with the established method of the rolling ball viscometer.

Since this technique was not used in literature for low viscous liquids, some tests were performed to identify possible modifications of the method that can optimize it. Among the tests, the viscosity of the water/glycerol mixtures was measured at different frequencies ranging between 2.6 and 3.6 MHz, showing that the viscosity of the mixtures is independent of the wave frequency.

Considering the final goal for this ultrasonic viscometer to study molten fuel salts, it is desired to minimize the liquid volume needed for the measurement of the viscosity. Few modifications of the initial set up were done in order to lower the amount of liquid measured. The sensitivity of the ultrasonic method with respect to the dimension of the plate and the container was investigated. The viscosity was not influenced by the width of the plate. The results of the plates with width 40, 60 and 80 mm, were all in good agreement with the literature. The waves only travel through the middle of the plate, so making the plate wider than practically necessary (wider than the transducer) does not contribute to the accuracy of viscosity measurements. Varying the thickness,

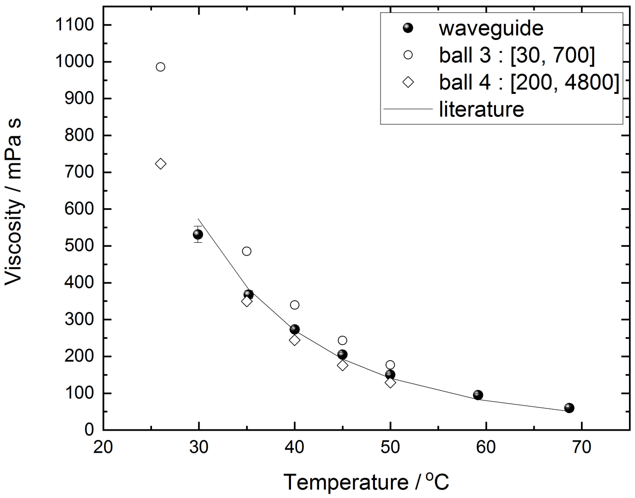

Figure 6.2: Viscosity of pure glycerol measured with the waveguide and with the falling ball viscometer using two different balls (3 and 4) with a different viscosity range of operation compared to literature data [10].

0.1 mm instead of 0.2 mm, and the material of the plate, tungsten instead of stainless steel, gave results not in agreement with the literature. A plate too thin causes more fluctuations in the signal. The use of tungsten instead of stainless steel was driven by the fact that molten fuel salts can corrode stainless steel in the presence of oxygen or moisture. Tungsten instead, does not react with the molten salts. The smallest volume of liquid measured in this work is 44 ml, which gave viscosity results corresponding to literature data.

This work shows that this type of viscosity measurement is suitable for liquids with low viscosity in a harsh environment, where the electronic parts should be kept apart from the liquid. This method has many advantages for high temperatures, high corrosion and high radioactivity liquids.

6.1.4. DISSOLUTION OF MOLTEN FUEL SALT IN WATER

In case of an accident in the MSFR, the fuel salt can be drained via freeze plugs into storage tanks under the reactor core. In a preliminary design of the MSFR, there are cooling rods in the draining tanks consisting of a thick layer of inert salt surrounded by a central channel where cooling water can circulate [11].

Following a hypothetical situation in which the molten fuel salt and water come into contact, the fuel salt can dissolve in water. Therefore, the following question was formulated:

Do alkali and actinide fluoride dissolve in water in conditions such as high tempera-

ture and irradiation?

Experimental data on the dissolution of molten fuel salt in water are provided in this work. The study was executed on the simulant salt fuel FLiNaK to test the procedure and successively on the eutectic LiF-ThF_4 (78-22 mol %) mixture and on the LiF-ThF_4-UF_4 (76.2-21.3-2.5 mol %) fuel mixture.

For the two compositions: the eutectic LiF-ThF_4 and the LiF-ThF_4-UF_4 fuel mixture, the concentration of Th and U in water remained low (below 1 mmol/l) in all the cases studied. The data on the solubility of the single cations after irradiation were useful in simulating an accident environment, where the molten fuel at high temperature interacts with water from the storage tanks and may dissolve high radioactive cations. The temperature, in case of an accident, may be much higher than 25°C for a long time. Measurements of the fuel salt in water at an elevated temperature of 75°C have been made for evaluating the probable course of events in the weeks following a postulated incident. It was found that the concentration of dissolved lithium and thorium increased, with respect to the concentration from the mixtures at room temperature, increasing the temperature and placing the mixtures in a Co-source radiation field, while the concentration of uranium was not influenced by the temperature and irradiation condition. The material characterisation performed before and after interaction of the salt with water by XRD permitted the identification of the hydrate species $Li_3Th_5[OH]F_{22}$ and $LiThF_4 \cdot 1.5\ H_2O$.

6.1.5. MAIN CONCLUSIONS

The main conclusions of this study can be summarized as follows:

- The melting point of the salt mixture, LiF-ThF_4-UF_4-PuF_3 (77.5-6.6-12.3-3.6 mol%), was measured for the first time. The solidus temperature was found to be in agreement with the modeled data from the phase diagram.
- The melting point of PuF_3 was measured in several crucibles aiming to identify the best material, in terms of chemical compatibility with the salt. A crucible in BN and a liner in W or Pt is the most suitable for this experiment.
- The thermal diffusivity of solid salts, alkali and actinide fluorides, has been studied. Eight salts have been measured, five of which were pressed pellets and pre molten salts. We found that: the thermal conductivity of alkali fluorides is higher than the thermal conductivity of actinide fluorides. The thermal conductivity is smaller for salt having more constituents.
- The ultrasonic guided wave technique for measuring the viscosity was applied to low viscous fluids. The relative error to the literature for the studied fluids was lower than 12% while the uncertainty in the measurements was lower than 5 %. The same technique was applied for fluids up to 70°C.
- The dissolution of molten fluoride salts in water was investigated. ICP-OES was used to perform elemental analysis on the liquid where the salts were dissolved. The alkali fluorides (KF, LiF, NaF) showed a higher concentration in water (up to 100 mmol/l), while the concentration of Th and U remained low (below 1 mmol/l).

6.1.6. OUTLOOK

The results presented in this thesis address gaps in the data on MSR fuel salts. Despite this, future research has to be conducted to validate the properties measured in this work (melting point, thermal diffusivity, dissolution and concentration in water). One of the aspects that needs improvement is that some of the measurements were not confirmed by multiple measurements. The melting point of plutonium fluoride measured in crucibles of different materials had a standard deviation of 14 K. The measurements performed in the BN crucible with W and Pt liners showed results in agreement with the literature [5] and a standard deviation among three runs of 2 K. However, these measurement were not repeated on another sample of plutonium fluoride. Also, the measurements of the thermal diffusivity of the alkali and actinide fluorides were not repeated. We suggest to perform new DSC measurements of PuF_3 in a BN crucible with a Pt or W liner to optimize the melting point measurement. We also suggest to measure the thermal diffusivity again via laser flash analysis (LAF) on each salt composition already measured in this research. Both measurements (DSC and LAF) should be preceded and followed by an XRD measurement. We stressed the importance of the XRD analysis to determine the purity of the sample. The XRD measurements were important in understanding when oxide was formed after the melting point measurement.

The results presented show that, in order to properly characterize molten salts, the oxidation of the salt has to be taken into consideration. For example, the melting point of the plutonium fluoride was influenced by its oxidation. The PuF_3 samples melted in Pt and W liners were not analyzed by XRD after the melting point measurement. In order to confirm that the melting point measured in these last crucible is reliable and no oxide is formed, the XRD pattern of these samples have to be analyzed.

The main factor influencing the properties of the salt is its composition. We have shown the differences in thermal diffusivity and dissolution of the salt in water, when the composition was changed by adding more components. For example, the thermal diffusivity of actinide fluorides with three components was lower than the thermal diffusivity of a two component system. More knowledge on the behaviour of molten salts is needed to understand the mechanisms behind these properties. We suggest the investigation of the lower thermal diffusivity of actinide fluorides with respect to the alkali fluoride. Moreover, we suggest to investigate why multi component salts have a lower thermal diffusivity than single component salts. Furthermore when dissolving the salt in water, the concentration of the same single fluoride was different if the last one was part of one multi component system or another. For example, the concentration in water of LiF part of LiF-ThF_4 and LiF-ThF_4-UF_4 was different. Another measurement should show if the concentration of the same single fluoride is different if PuF_3 is added to the system. The influence of PuF_3 in the dissolution of the salt might be a topic for a future study.

The research described in chapter 4 is a preliminary work on the use of an ultrasonic viscometer for low viscous fluids at high temperature. The aim of the project was to develop a viscometer for measuring molten salts. Future applications of this ultrasonic viscometer should address the possibility of performing measurements at higher temperatures. The viscometer has to be adapted for temperatures between 400 and 800 °C, temperatures in which the molten salts will have to be studied.

Measurements have been performed changing the material of the waveguide. This study was done because the material of the waveguide should be chemically compatible with the molten salts. The uncertainty on the viscosity, by using a thin tungsten plate, was higher than for the measurements performed using the stainless steel plate. In this case, two parameters were changed with respect to the measurements performed with the stainless steel plate: the thickness of the plate and its material. More measurements have to be performed with a thicker plate of tungsten, not available when this research was performed, or a thinner plate of stainless steel to understand the origin of the error. Also, an analysis using other materials for the waveguide, such as molybdenum, should be performed to see if the measurements can be carried out using more metallic waveguides.

Since the molten fuel salts are radioactive, we want to be able to measure the salt properties with the smallest amount possible. Using the ultrasonic viscometer a small volume of liquid can be measured. Smaller containers than the ones used for this reseach, could be used in the setup, and by adjusting the setup, using less wide plates, the volume could be decreased from 40 ml (the volume of the smallest container used in the research) to 10 ml.

The possibility to measure non-Newtonian fluids will also be considered for a further development of the ultrasonic viscometer.

Finally, other physico-chemical properties should be measured for characterizing the fuel salt. Among the most relevant physico-chemical properties not tackled in this work, the density, heat capacity, heat transport properties should be measured to characterize the fuel salt. The effect of the composition change of the salt after or during an experiment should be measured with the elemental analysis in order to quantify the uncertainty on each measurement.

REFERENCES

[1] P. Souek, O. Bene, B. Claux, E. Capelli, M. Ougier, V. Tyrpekl, J.-F. Vigier, and R. J. Konings, *Synthesis of UF_4 and ThF_4 by HF gas fluorination and re-determination of the UF_4 melting point,* Journal of Fluorine Chemistry **200**, 33 (2017).

[2] T. E. Phipps, R. L. Seifert, and O. C. Simpson, *The transuranium elements: research papers,* National Nuclear Energy Series Div IV **14 B** (1949).

[3] E. F. Westrum and J. C. Wallmann, *The melting point and heat of sublimation of PuF_3 1,* Journal of the American Chemical Society **73**, 3530 (1951).

[4] H. P. Robinson, *Manhattan Project Metallurgical Laboratory Report CN-2159,* Tech. Rep. (1944).

[5] A. Tosolin, J.-Y. Colle, S. Mastromarino, P. Souek, L. Luzzi, R. J. M. Konings, and O. Bene, *Vaporization behaviour of a PuF_3 -containing fuel mixture for the Molten Salt Fast Reactor,* Journal of Nuclear Materials **527**, 151780 (2019).

[6] E. Capelli, O. Bene, and R. Konings, *Thermodynamic assessment of the LiFThF_4PuF3UF_4 system,* Journal of Nuclear Materials **462**, 43 (2015).

[7] H. Chang, M. Altman, and R. Sharma, *The Determination of Thermal Diffusivities of Thermal Energy Storage Materials,* Transaction of ASME, Journal of Engineering for Power , 407 (1967).

[8] X. Yu and A. M. Hofmeister, *Thermal diffusivity of alkali and silver halide crystals as a function of temperature,* Journal of Applied Physics **109**, 033516 (2011).

[9] T. K. Vogt, M. J. S. Lowe, and P. Cawley, *Measurement of the Material Properties of Viscous Liquids Using Ultrasonic Guided Waves,* IEEE Transactions on Ultrasonics, Ferroelectrics, and Frequency Control **51**, 737 (2004).

[10] N.-S. Cheng, *Formula for the Viscosity of a GlycerolWater Mixture,* Industrial & Engineering Chemistry Research **47**, 3285 (2008).

[11] M. Allibert, D. Gérardin, D. Heuer, E. Huffer, A. Laureau, E. Merle, S. Beils, A. Cammi, B. Carluec, S. Delpech, A. Gerber, E. Girardi, J. Krepel, D. Lathouwers, D. Lecarpentier, S. Lorenzi, L. Luzzi, S. Poumerouly, M. Ricotti, and V. Tiberi, *A Paradigm Shift in Nuclear Reactor Safety with the Molten Salt Fast Reactor Grant Agreement number: 661891 SAMOFAR D1.1 Description of initial reference design and identification of safety aspects*, Tech. Rep. (2016).

CURRICULUM VITÆ

01-10-1991	Born in Aprilia, Italy.

EDUCATION

2016–2021	Ph. D. student in nuclear engineering Delft University of Technology Delft, The Netherlands

Thesis:	New measurement methods and physico-chemical properties of the MSFR salt
Promotor:	Prof. dr. ir. J. L. Kloosterman
Promotor:	Prof. dr. ir. M. Rohde

2013–2015	M.S. Physical Chemistry, Cum Laude Università La Sapienza di Roma Roma, Italy
2010–2013	B.S. Chemistry Università La Sapienza di Roma Roma, Italy

PROFESSIONAL EXPERIENCE

2020–2021	R & D Engineer University of California - Berkeley Berkeley, California, United States
2019–2020	Grantholder European Commission, Joint Research Centre Karlsruhe, Germany
2015	Trainee European Commission, Joint Research Centre Institute for Transuranium Elements Karlsruhe, Germany

AWARDS GRANTS

2018	ENEN + project
2018	Young Nuclear Generation Award
2017	Grant AS Science Day
2015	Gentle project

List of Publications

12. S. Mastromarino, R. Vidrio, E. Still, L. Chapdelaine, R. O. Scarlat, Measurements and Uncertainty Quantification for the Density and Coefficient of Thermal Expansion of Molten 2LiF-BeF2 (FLiBe), in preparation.

11. W. Derdeyn, S. Mastromarino, R. Gakhar, M. Anderson, M. Kats,R. O. Scarlat, High Temperature Liquid Fluoride Salts Optical Spectroscopic Methods and Data with Focus on Structural Interpretation and Relevance to Radiative Heat Transfer, submitted to Journal of Molecular Liquids.

10. S. R. Scott, S. Mastromarino, F. Carotti, A. Kruizenga, R. O. Scarlat, M. M. Shafer, Simultaneous measurement of lithium isotope and lithium/beryllium ratios in FLiBe salts using MC-ICP-MS, in preparation.

9. J. Qiu. D. D Macdonald, J. Han, J. R. Scully, R. Schoell; S. Mastromarino; D. Kaoumi, Electrochemical study of the dissolution of oxide films grown on Type 316L stainless steel in molten fluoride salt, Corrosion Science 181 (2021) 109457.

8. S. Mastromarino, R. Rook, D. De Haas, E. D. J. Verschuur, M. Rohde, and J. L. Kloosterman; An Ultrasonic Shear Wave Viscometer for Low Viscosity Newtonian Liquids, Measurement Science and Technology 32 (2021) 125305.

7. S. Mastromarino, E.Capelli, E. Epifano, O.Benes, J.L.Kloosterman, Physicochemical effect of mixing molten fuel salt and water, to be submitted to Journal of Fluorine Chemistry.

6. A. Tosolin, S. Mastromarino, J-Y Colle, P Souek , L. Luzzi, R.J.M. Konings, O. Bene, Vaporization behaviour of a PuF3 containing fuel mixture for the Molten Salt Fast Reactor, Journal of Nuclear Materials 527 (2019) 151780.

5. E. Hashem, A. Seibert, J .F. Vigier, M. Naji, S. Mastromarino, A. Ciccioli, D. Manara, Solid-liquid equilibria in the ThO2 ZrO2 system: an experimental study, Journal of Nuclear Materials 521 (2019) 99-108.

4. D.Manara, M. Naji, S. Mastromarino, J.M. Elorrieta, N. Magnani, L. Martel, J-Y Colle, The Raman fingerprint of plutonium dioxide: Some example applications for the detection of PuO 2 in host matrices, Journal of Nuclear Materials 499 (2018) 268-271.

3. S. Mastromarino, A.Seibert, E.Hashem, A.Ciccioli, D.Prieur, A.Scheinost, S.Stohr, P.Lajarge, J.Boshoven, D.Robba, M.Ernstberger, D.Bottomley, D.Manara, Assessment of solid/liquid equilibria in the (U, Zr)O2+y system, Journal of Nuclear Materials 494 (2017) 368-379.

2. D.Manara, L. Soldi, S. Mastromarino, K. Boboridis, D. Robba, L. Vlahovic, R. Konings, Laser-heating and Radiance Spectrometry for the Study of Nuclear Materials in Conditions Simulating a Nuclear Power Plant Accident, Journal of Visualised Experiments 130 (2017).

1. M. Naji, N. Magnani, L. J. Bonales, S. Mastromarino, J.-Y. Colle, J. Cobos, D. Manara, Raman spectrum of plutonium dioxide: Vibrational and crystal field modes, Phys. Rev. B 95, 104307 Published 29 March 2017.

Conferences

10. NUMAT Fall 2020 Virtual Meeting, October 26-29, 2020, Measurements and Uncertainty Quantification for the Density and Coefficient of Thermal Expansion of Molten 2LiF-BeF2 (FLiBe), Presenter
9. ACS Fall 2020 Virtual Meeting-Symposium on Molten Salt Chemistry, August 16-20, 2020, Digestion methods: Sample preparation for the elemental analysis of molten fluoride salts, Speaker
8. International Youth Nuclear Congress 2020 - Australia, March 8-13 2020; Generation iv an opportunity for nuclear energy, Workshop manager
7. NuFuel-MMSNF 2019 Workshop, November 4-7 2019, Physicochemical properties of MSFR fuel, Speaker
6. SAMOFAR Final Meeting, July 4-5 2020, Thermodynamic properties of MSFR fuel and coolant, Speaker
5. SAMOFAR Final Meeting, July 4-5 2020, Physicochemical effect of mixing molten fuel salt and water, Poster presentation
4. NUMAT 2018, Seattle October14-18 2018, Development of a ultrasonic viscometer for molten salt, Speaker
3. NUMAT 2018, Seattle October14-18 2018, Molten fuel salt interaction with water, Poster presentation
2. NuFuel 2017, Lecco, September 4-6 2017, Development of a high temperature ultrasonic viscometer, Speaker
1. NuFuel 2015, November 16-18 2015, Characterisation of Essential Corium Subsystems Up To Melting, Poster presentation